

CERN-PH-EP-2013-192

Submitted to: JHEP

Measurement of dijet cross-sections in pp collisions at 7 TeV centre-of-mass energy using the ATLAS detector

The ATLAS Collaboration

Abstract

Double-differential dijet cross-sections measured in pp collisions at the LHC with a 7 TeV centre-of-mass energy are presented as functions of dijet mass and half the rapidity separation of the two highest- p_T jets. These measurements are obtained using data corresponding to an integrated luminosity of 4.5 fb^{-1} , recorded by the ATLAS detector in 2011. The data are corrected for detector effects so that cross-sections are presented at the particle level. Cross-sections are measured up to 5 TeV dijet mass using jets reconstructed with the anti- k_t algorithm for values of the jet radius parameter of 0.4 and 0.6. The cross-sections are compared with next-to-leading-order perturbative QCD calculations by NLOJet++ corrected to account for non-perturbative effects. Comparisons with POWHEG predictions, using a next-to-leading-order matrix element calculation interfaced to a parton-shower Monte Carlo simulation, are also shown. Electroweak effects are accounted for in both cases. The quantitative comparison of data and theoretical predictions obtained using various parameterizations of the parton distribution functions is performed using a frequentist method. In general, good agreement with data is observed for the NLOJet++ theoretical predictions when using the CT10, NNPDF2.1 and MSTW 2008 PDF sets. Disagreement is observed when using the ABM11 and HERAPDF1.5 PDF sets for some ranges of dijet mass and half the rapidity separation. An example setting a lower limit on the compositeness scale for a model of contact interactions is presented, showing that the unfolded results can be used to constrain contributions to dijet production beyond that predicted by the Standard Model.

© 2014 CERN for the benefit of the ATLAS Collaboration.

Reproduction of this article or parts of it is allowed as specified in the CC-BY-3.0 license.

Measurement of dijet cross-sections in pp collisions at 7 TeV centre-of-mass energy using the ATLAS detector

The ATLAS Collaboration

E-mail: atlas.publications@cern.ch

ABSTRACT: Double-differential dijet cross-sections measured in pp collisions at the LHC with a 7 TeV centre-of-mass energy are presented as functions of dijet mass and half the rapidity separation of the two highest- p_T jets. These measurements are obtained using data corresponding to an integrated luminosity of 4.5 fb^{-1} , recorded by the ATLAS detector in 2011. The data are corrected for detector effects so that cross-sections are presented at the particle level. Cross-sections are measured up to 5 TeV dijet mass using jets reconstructed with the anti- k_t algorithm for values of the jet radius parameter of 0.4 and 0.6. The cross-sections are compared with next-to-leading-order perturbative QCD calculations by NLOJet++ corrected to account for non-perturbative effects. Comparisons with POWHEG predictions, using a next-to-leading-order matrix element calculation interfaced to a parton-shower Monte Carlo simulation, are also shown. Electroweak effects are accounted for in both cases. The quantitative comparison of data and theoretical predictions obtained using various parameterizations of the parton distribution functions is performed using a frequentist method. In general, good agreement with data is observed for the NLO-Jet++ theoretical predictions when using the CT10, NNPDF2.1 and MSTW 2008 PDF sets. Disagreement is observed when using the ABM11 and HERAPDF1.5 PDF sets for some ranges of dijet mass and half the rapidity separation. An example setting a lower limit on the compositeness scale for a model of contact interactions is presented, showing that the unfolded results can be used to constrain contributions to dijet production beyond that predicted by the Standard Model.

Contents

1	Introduction	2
2	The ATLAS experiment	3
3	Data-taking conditions	3
4	Cross-section definition	4
5	Monte Carlo samples	5
6	Theoretical predictions and uncertainties	5
6.1	Theoretical predictions	5
6.2	Theoretical uncertainties	6
7	Trigger, jet reconstruction and data selection	9
8	Stability of the results under pileup conditions	11
9	Data unfolding	13
10	Experimental uncertainties	14
11	Frequentist method for a quantitative comparison of data and theory spectra	16
11.1	Test statistic	16
11.2	Frequentist method	17
12	Cross-section results	20
12.1	Quantitative comparison with NLOJet++ predictions	20
12.2	Comparison with POWHEG predictions	29
13	Exploration and exclusion of contact interactions	32
14	Summary and conclusions	35
A	Tables of results	37

1 Introduction

Measurements of jet production in pp collisions at the LHC [1] test the predictions of Quantum Chromodynamics (QCD) at the largest centre-of-mass energies explored thus far in colliders. They are useful for understanding the strong interaction and its coupling strength α_S , one of the fundamental parameters of the Standard Model. The measurement of cross-sections as a function of dijet mass is also sensitive to resonances and new interactions, and can be employed in searches for physics beyond the Standard Model. Where no new contribution is found, the cross-section results can be exploited to study the partonic structure of the proton. In particular, the high dijet-mass region can be used to constrain the parton distribution function (PDF) of gluons in the proton at high momentum fraction.

Previous measurements at the Tevatron in $p\bar{p}$ collisions have shown good agreement between predictions from QCD calculations and data for lower dijet mass [2, 3]. Recent results from the LHC using pp collisions have extended the measurement of dijet production cross-sections to higher dijet-mass values [4–6]. While good agreement between data and several theoretical predictions has been observed in general, the predicted cross-section values using the CT10 PDF set [7] at high dijet mass tend to be larger than those measured in data.

In this paper, measurements of the double-differential dijet cross-sections are presented as functions of the dijet mass and half the rapidity separation of the two highest- p_T jets. The measurements are made at the particle level (see section 4 for a definition), using the iterative, dynamically stabilized (IDS) unfolding method [8] to correct for detector effects. The use of an integrated luminosity more than a factor of 100 larger than in the previous ATLAS publication [5] improves the statistical power in the high dijet-mass region. In spite of the increased number of simultaneous proton–proton interactions in the same beam bunch crossing during 2011 data taking, improvements in the jet energy calibration result in an overall systematic uncertainty smaller than previously achieved [9]. The measurements are compared to next-to-leading-order (NLO) QCD calculations [10], as well as to a NLO matrix element calculation by POWHEG [11], which is interfaced to the parton-shower Monte Carlo generator PYTHIA. Furthermore, a quantitative comparison of data and theory predictions is made using a frequentist method.

New particles, predicted by theories beyond the Standard Model (SM), may decay into dijets that can be observed as narrow resonances in dijet mass spectra [12]. New interactions at higher energy scales, parameterized using an effective theory of contact interactions [13], may lead to modifications of dijet cross-sections at high dijet mass. Searches for these deviations have been performed by ATLAS [14] and CMS [15]. The approach followed here is to constrain physics beyond the SM using unfolded cross-sections and the full information on their uncertainties and correlations. This information is also provided in HepData [16]. This has the advantage of allowing new models to be confronted with data without the need for additional detector simulations. This paper considers only one theory of contact interactions, rather than presenting a comprehensive list of exclusion ranges for various models. The results are an illustration of what can be achieved using unfolded data, and do not seek to improve the current exclusion range.

The content of the paper is as follows. The ATLAS detector and data-taking conditions are briefly described in sections 2 and 3, followed by the cross-section definition in section 4. Sections 5 and 6 describe the Monte Carlo samples and theoretical predictions, respectively. The trigger, jet reconstruction, and data selection are presented in section 7, followed by studies of the stability of the results under different luminosity conditions (pileup) in section 8. Sections 9 and 10 discuss the data unfolding and systematic uncertainties on the measurement, respectively. These are followed by the introduction of a frequentist method for the quantitative comparison of data and theory predictions in section 11. The cross-section results are presented in section 12, along with quantitative statements of the ability of the theory prediction to describe the data. An application of the frequentist method for setting a lower limit on the compositeness scale of a model of contact interactions is shown in section 13. Finally, the conclusions are given in section 14.

2 The ATLAS experiment

The ATLAS detector is described in detail elsewhere [17]. The main system used for this analysis is the calorimeter, divided into electromagnetic and hadronic parts. The lead/liquid-argon (LAr) electromagnetic calorimeter is split into three regions:¹ the barrel ($|\eta| < 1.475$), the end-cap ($1.375 < |\eta| < 3.2$), and the forward ($3.1 < |\eta| < 4.9$) regions. The hadronic calorimeter is divided into four regions: the barrel ($|\eta| < 0.8$) and the extended barrel ($0.8 < |\eta| < 1.7$) made of scintillator/steel, the end-cap ($1.5 < |\eta| < 3.2$) with LAr/copper modules, and the forward calorimeter covering ($3.1 < |\eta| < 4.9$) composed of LAr/copper and LAr/tungsten modules. The tracking detectors, consisting of silicon pixels, silicon microstrips, and transition radiation tracking detectors immersed in a 2 T axial magnetic field provided by a solenoid, are used to reconstruct charged-particle tracks in the pseudorapidity region $|\eta| < 2.5$. Outside the calorimeter, a large muon spectrometer measures the momenta and trajectories of muons deflected by a large air-core toroidal magnetic system.

3 Data-taking conditions

Data-taking periods in ATLAS are divided into intervals of approximately uniform running conditions called luminosity blocks, with a typical duration of one minute. For a given pair of colliding beam bunches, the expected number of pp collisions per bunch crossing averaged over a luminosity block is referred to as μ . The average of μ over all bunches in the collider for a given luminosity block is denoted by $\langle\mu\rangle$. In 2011 the peak luminosity delivered by

¹ATLAS uses a right-handed coordinate system with its origin at the nominal interaction point (IP) in the centre of the detector and the z -axis pointing along the beam axis. The x -axis points from the IP to the centre of the LHC ring, and the y -axis points upward. Cylindrical coordinates (r, ϕ) are used in the transverse plane, ϕ being the azimuthal angle around the beam axis, referred to the x -axis. The pseudorapidity is defined in terms of the polar angle θ with respect to the beamline as $\eta = -\ln \tan(\theta/2)$. When dealing with massive jets and particles, the rapidity $y = 1/2 \ln(E + p_z)/(E - p_z)$ is used, where E is the jet energy and p_z is the z -component of the jet momentum. The transverse momentum p_T is defined as the component of the momentum transverse to the beam axis.

the accelerator at the start of an LHC fill increased, causing $\langle\mu\rangle$ to change from 5 at the beginning of the data-taking period to more than 18 by the end. A *bunch train* in the accelerator is generally composed of 36 proton bunches with 50 ns *bunch spacing*, followed by a larger 250 ns window before the next bunch train.

The overlay of multiple collisions, either from the same bunch crossing or due to electronic signals present from adjacent bunch crossings, is termed *pileup*. There are two separate, although related, contributions to consider. In-time pileup refers to additional energy deposited in the detector due to simultaneous collisions in the same bunch crossing. Out-of-time pileup is a result of the 500 ns pulse length of the LAr calorimeter readout, compared to the 50 ns spacing between bunch crossings, leaving residual electronic signals in the detector, predominantly from previous interactions. The shape of the LAr calorimeter pulse is roughly a 100 ns peak of positive amplitude, followed by a shallower 400 ns trough of negative amplitude. Due to this trough, out-of-time pileup results by design in a subtraction of measured energy in the LAr calorimeter, providing some compensation for in-time pileup.

4 Cross-section definition

Jet cross-sections are defined using jets reconstructed by the anti- k_t algorithm [18] implemented in the FastJet [19] package. In this analysis, jets are clustered using two different values of the radius parameter, $R = 0.4$ and $R = 0.6$.

Non-perturbative (hadronization and underlying event) and perturbative (higher-order corrections and parton showers) effects are different, depending on the choice of the jet radius parameter. By performing the measurement for two values of the jet radius parameter, different contributions from perturbative and non-perturbative effects are probed. The fragmentation process leads to a dispersion of the jet constituents, more of which are collected for jets with a larger radius parameter. Particles from the underlying event make additional contributions to the jet, and have less of an effect on jets with a smaller radius parameter. Additionally, hard emissions lead to higher jet multiplicity when using a smaller jet radius parameter.

Measured cross-sections are corrected for all experimental effects, and thus are defined at the *particle-level* final state. Here particle level refers to stable particles, defined as those with a proper lifetime longer than 10 ps, including muons and neutrinos from decaying hadrons [20].

Events containing two or more jets are considered, with the leading (subleading) jet defined as the one within the range $|y| < 3.0$ with the highest (second highest) p_T . Dijet double-differential cross-sections are measured as functions of the dijet mass m_{12} and half the rapidity separation $y^* = |y_1 - y_2|/2$ of the two leading jets. This rapidity separation is invariant under a Lorentz boost along the z -direction, so that in the dijet rest frame $y'_1 = -y'_2 = y^*$. The leading (subleading) jet is required to have $p_T > 100$ GeV ($p_T > 50$ GeV). The requirements on p_T for the two jets are asymmetric to improve the stability of the NLO calculation [21]. The measurement is made in six ranges of $y^* < 3.0$, in equal steps of 0.5.

In each range of y^* , a lower limit on the dijet mass is chosen in order to avoid the region of phase space affected by the requirements on the p_T of the two leading jets.

5 Monte Carlo samples

The default Monte Carlo (MC) generator used to simulate jet events is PYTHIA 6.425 [22] with the ATLAS Underlying Event Tune AUET2B [23]. It is a leading-order (LO) generator with $2 \rightarrow 2$ matrix element calculations, supplemented by leading-logarithmic parton showers ordered in p_T . A simulation of the underlying event is also provided, including multiple parton interactions. The Lund string model [24] is used to simulate the hadronization process. To simulate pileup, minimum bias events² are generated using PYTHIA 8 [25] with the 4C tune [26] and MRST LO** proton PDF set [27]. The number of minimum bias events overlaid on each signal event is chosen to model the distribution of $\langle\mu\rangle$ throughout the data-taking period.

To estimate the uncertainties on the hadronization and parton-shower modelling, events are also generated by HERWIG++ 2.5.2 [28–30] using the UE-EE-3 tune [31]. In this LO generator, the parton shower follows an angular ordering, and a clustering model [32] is used for the hadronization. The effect of the underlying event is included using the eikonal multiple-scattering model [33].

Two PDF sets are considered for both MC generators. For the nominal detector simulation, the MRST LO** proton PDF set is used. Additionally, versions of the same tunes based on the CTEQ6L1 [34] proton PDF set are used to assess uncertainties on the non-perturbative corrections (see section 6.2).

The output four-vectors from these event generators are passed to a detector simulation [35] based on GEANT4 [36]. Simulated events are digitized to model the detector responses, and then reconstructed using the software used to process data.

6 Theoretical predictions and uncertainties

The measured dijet cross-sections are compared to fixed-order NLO QCD predictions by NLOJet++ [10], corrected for non-perturbative effects in the fragmentation process and in the underlying event using calculations by PYTHIA 6.425. A NLO matrix element calculation by POWHEG, which is interfaced to the PYTHIA parton-shower MC generator, is also considered. Both the NLOJet++ and POWHEG predictions are corrected to account for NLO electroweak effects. When used in this paper, the term *Standard Model predictions* refers to NLO QCD calculations corrected for non-perturbative and electroweak effects.

6.1 Theoretical predictions

The fixed-order $O(\alpha_S^3)$ QCD calculations are performed with the NLOJet++ program interfaced to APPLGRID [37] for fast convolution with various PDF sets. The following proton PDF sets are considered for the theoretical predictions: CT10 [7], HERAPDF1.5

²Events passing a trigger with minimum requirements, and which correspond mostly to inelastic pp collisions, are called minimum-bias events.

[38], epATLJet13 [39], MSTW 2008 [40], NNPDF2.1 [41, 42] and NNPDF2.3 [43], and ABM11 [44]. The epATLJet13 PDF set is the result of simultaneously using in the fit ATLAS jet data, collected at centre-of-mass energies of 2.76 TeV and 7 TeV, and HERA-I ep data. In the previous ATLAS measurement [5], a scale choice was introduced to ensure that the cross-sections remained positive for large values of y^* . Although values of y^* greater than 3.0 are not considered here, the same choice is used for consistency. The renormalization (μ_R) and factorization (μ_F) scales are set to

$$\mu = \mu_R = \mu_F = p_T^{\max} e^{0.3y^*}, \quad (6.1)$$

where p_T^{\max} is the p_T of the leading jet. Further details can be found in ref. [45].

Non-perturbative corrections are evaluated using leading-logarithmic parton-shower generators, separately for each value of the jet radius parameter. The corrections are calculated as bin-by-bin ratios of the dijet differential cross-section at the particle level, including hadronization and underlying event effects, over that at the parton level. The nominal corrections are calculated using PYTHIA 6.425 with the AUET2B tune derived for the MRST LO** PDF set. The non-perturbative corrections as a function of dijet mass are shown in figure 1(a) for the range $1.0 \leq y^* < 1.5$.

Comparisons are also made to the POWHEG [11, 46, 47] NLO matrix element calculation³ interfaced to a parton-shower MC generator, using the CT10 PDF set. For these calculations the factorization and renormalization scales are set to the default value of p_T^{Born} , the transverse momentum in the $2 \rightarrow 2$ process before the hardest emission. The parton-level configurations are passed to the PYTHIA generator for fragmentation and underlying event simulation. Both the AUET2B and Perugia 2011 [49] tunes are considered. The version of the program used includes an explicit calculation of all hard emission diagrams [39, 50]. This provides improved suppression of rare events, removing fluctuations that arise from the migration of jets with low values of parton-level p_T to larger values of particle-level p_T .

Corrections for electroweak tree-level effects of $O(\alpha\alpha_S, \alpha^2)$ as well as weak loop effects of $O(\alpha\alpha_S^2)$ [51] are applied to both the NLOJet++ and POWHEG predictions. The calculations are derived for NLO electroweak processes on a LO QCD prediction of the observable in the phase space considered here. In general, electroweak effects on the cross-sections are $< 1\%$ for values of $y^* \geq 0.5$, but reach up to 9% for $m_{12} > 3$ TeV in the range $y^* < 0.5$. The magnitude of the corrections on the theoretical predictions as a function of dijet mass in several ranges of y^* is shown in figure 1(b). The electroweak corrections show almost no dependence on the jet radius parameter.

6.2 Theoretical uncertainties

To estimate the uncertainty due to missing higher-order terms in the fixed-order calculations, the renormalization scale is varied up and down by a factor of two. The uncertainty due to the choice of factorization scale, specifying the separation between the short-scale

³The folding values of `foldcsi=5`, `foldy=10`, `foldphi=2` associated with the spacing of the integration grid as described in ref. [48], are used.

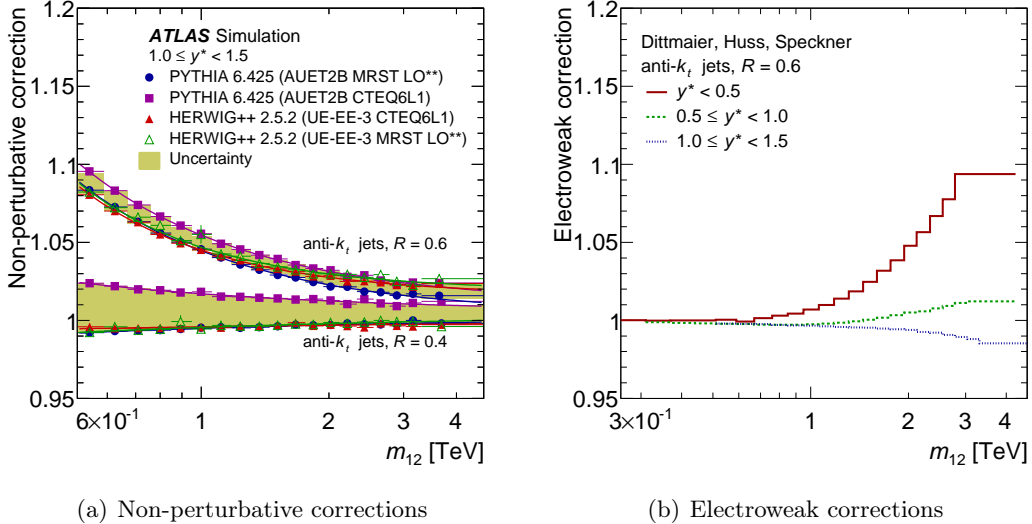


Figure 1. Non-perturbative corrections (ratio of particle-level cross-sections to parton-level cross-sections) obtained using various MC generators and tunes are shown in (a), for the differential dijet cross-sections as a function of dijet mass in the range $1.0 \leq y^* < 1.5$ with values of jet radius parameter $R = 0.4$ and $R = 0.6$. Uncertainties are taken as the envelope of the various curves. Electroweak corrections are shown in (b) as a function of dijet mass in multiple ranges of y^* [51], for jet radius parameter $R = 0.6$.

hard scatter and long-scale hadronization, is also varied by a factor of two. All permutations of these two scale choices are considered, except for cases where the renormalization and factorization scales are varied in opposite directions. In these extreme cases, logarithmic factors in the theoretical calculations may become large, resulting in instabilities in the prediction. The maximal deviations from the nominal prediction are taken as the uncertainty due to the scale choice. The scale uncertainty is generally within $^{+5\%}_{-15\%}$ for the $R = 0.4$ calculation, and $\pm 10\%$ for the $R = 0.6$ calculation.

The uncertainties on the cross-sections due to that on α_S are estimated using two additional proton PDF sets, for which different values of α_S are assumed in the fits. This follows the recommended prescription in ref. [52], such that the effect on the PDF set as well as on the matrix elements is included. The resulting uncertainties are approximately $\pm 4\%$ across all dijet-mass and y^* ranges considered in this analysis.

The multiple uncorrelated uncertainty components of each PDF set, as provided by the various PDF analyses, are also propagated through the theoretical calculations. The PDF analyses generally derive these from the experimental uncertainties on the data used in the fits. For the results shown in section 12 the standard Hessian sum in quadrature [53] of the various independent components is taken. The NNPDF2.1 and NNPDF2.3 PDF sets are exceptions, where uncertainties are expressed in terms of *replicas* instead of by independent components. These replicas represent a collection of equally likely PDF sets, where the data entering the PDF fit were varied within their experimental uncertainties. For the plots shown in section 12, the uncertainties on the NNPDF PDF sets are propagated

using the RMS of the replicas, producing equivalent PDF uncertainties on the theoretical predictions. For the frequentist method described in section 11, these replicas are used to derive a covariance matrix for the theoretical predictions. The eigenvector decomposition of this matrix provides a set of independent uncertainty components, which can be treated in the same way as those in the other PDF sets.

In cases where variations of the theoretical parameters are also available, these are treated as additional uncertainty components assuming a Gaussian distribution. For the HERAPDF1.5, NNPDF2.1, and MSTW 2008 PDF sets, the results of varying the heavy-quark masses within their uncertainties are taken as additional uncertainty components. The nominal value of the charm quark mass is taken as $m_c = 1.40$ GeV, and the bottom quark mass as $m_b = 4.75$ GeV. For NNPDF2.1 the mass of the charm quark is provided with a symmetric uncertainty, while that of the bottom quark is provided with an asymmetric uncertainty. NNPDF2.3 does not currently provide an estimate of the uncertainties due to heavy-quark masses. For HERAPDF1.5 and MSTW 2008, asymmetric uncertainties for both the charm and bottom quark masses are available. When considering the HERAPDF1.5 PDF set, the uncertainty components corresponding to the strange quark fraction and the Q^2 requirement are also included as asymmetric uncertainties.

In addition, the HERAPDF1.5 analysis provides four additional PDF sets arising from the choice of the theoretical parameters and fit functions, which are treated here as separate predictions. These are referred to as *variations* in the following, and include:

1. Varying the starting scale Q_0^2 from 1.9 GeV² to 1.5 GeV², while adding two additional parameters to the gluon fit function.
2. Varying the starting scale Q_0^2 from 1.9 GeV² to 2.5 GeV².
3. Including an extra parameter in the valence u -quark fit function.
4. Including an extra parameter in the \bar{u} -quark fit function.

Including the maximal deviations due to these four variations with respect to the original doubles the magnitude of the theoretical uncertainties at high dijet mass, as seen in section 12. When performing the quantitative comparison described in section 11, the four variations are treated as distinct PDF sets, since they are obtained using different parameterizations and their statistical interpretation in terms of uncertainties is not well defined.

The uncertainties on the theoretical predictions due to those on the PDFs range from 2% at low dijet mass up to 20% at high dijet mass for the range of smallest y^* values. For the largest values of y^* , the uncertainties reach 100–200% at high dijet mass, depending on the PDF set.

The uncertainties on the non-perturbative corrections, arising from the modelling of the fragmentation process and the underlying event, are estimated as the maximal deviations of the corrections from the nominal (see section 6.1) using the following three configurations: PYTHIA with the AUET2B tune and CTEQ6L1 PDF set, and HERWIG++ 2.5.2 with the UE-EE-3 tune using the MRST LO** or CTEQ6L1 PDF sets. In addition, the statistical uncertainty due to the limited size of the sample generated using the nominal tune is

included. The uncertainty increases from 1% for the range $y^* < 0.5$, up to 5% for larger values of y^* . The statistical uncertainty significantly contributes to the total uncertainty only for the range $2.5 \leq y^* < 3.0$.

There are several cases where the PDF sets provide uncertainties at the 90% confidence level (CL); in particular, the PDF uncertainty components for the CT10 PDF set, as well as α_s uncertainties for the CT10, HERAPDF1.5, and NNPDF2.1/2.3 PDF sets. In these cases, the magnitudes of the uncertainties are scaled to the 68% CL to match the other uncertainties. In general, the scale uncertainties are dominant at low dijet mass, and the PDF uncertainties are dominant at high dijet mass.

7 Trigger, jet reconstruction and data selection

This measurement uses the full data set of pp collisions collected with the ATLAS detector at 7 TeV centre-of-mass energy in 2011, corresponding to an integrated luminosity of 4.5 fb^{-1} [54]. Only events collected during stable beam conditions and passing all data-quality requirements are considered in this analysis. At least one primary vertex, reconstructed using two or more tracks, each with $p_T > 400 \text{ MeV}$, must be present to reject cosmic ray events and beam background. The primary vertex with the highest $\sum p_T^2$ of associated tracks is selected as the hard-scatter vertex.

Due to the high luminosity, a suite of single-jet triggers was used to collect data, where only the trigger with the highest p_T threshold remained unrescaled. An event must satisfy all three levels of the jet trigger system based on the transverse energy (E_T) of jet-like objects. Level-1 provides a fast, hardware decision using the combined E_T of low-granularity calorimeter towers. Level-2 performs a simple jet reconstruction in a window around the geometric region passed at Level-1, with a threshold generally 20 GeV higher than at Level-1. Finally, a jet reconstruction using the anti- k_t algorithm with $R = 0.4$ is performed over the entire detector solid angle by the Event Filter (EF). The EF requires transverse energy thresholds typically 5 GeV higher than those used at Level-2.

The efficiencies of the central jet triggers ($|\eta| < 3.2$) relevant to this analysis are shown in figure 2. They are determined using an unbiased sample known to be fully efficient in the jet- p_T range of interest. The unbiased sample can be either a random trigger, or a single-jet trigger that has already been shown to be fully efficient in the relevant jet- p_T range. The efficiency is presented in a representative rapidity interval ($1.2 \leq |y| < 2.1$), as a function of calibrated jet p_T , for jets with radius parameter $R = 0.6$. Triggers are used only where the probability that a jet fires the trigger is $> 99\%$. Because events are triggered using $R = 0.4$ jets, the p_T at which calibrated $R = 0.6$ jets become fully efficient is significantly higher than that for calibrated $R = 0.4$ jets. To take advantage of the lower p_T at which $R = 0.4$ jets are fully efficient, distinct p_T ranges are used to collect jets for each value of the radius parameter.

A dijet event is considered in this analysis if either the leading jet, the subleading jet, or both are found to satisfy one of the jet trigger requirements. Because of the random nature of the prescale decision, some events are taken not because of the leading jet, but instead because of the subleading jet. This two-jet trigger strategy results in an increase

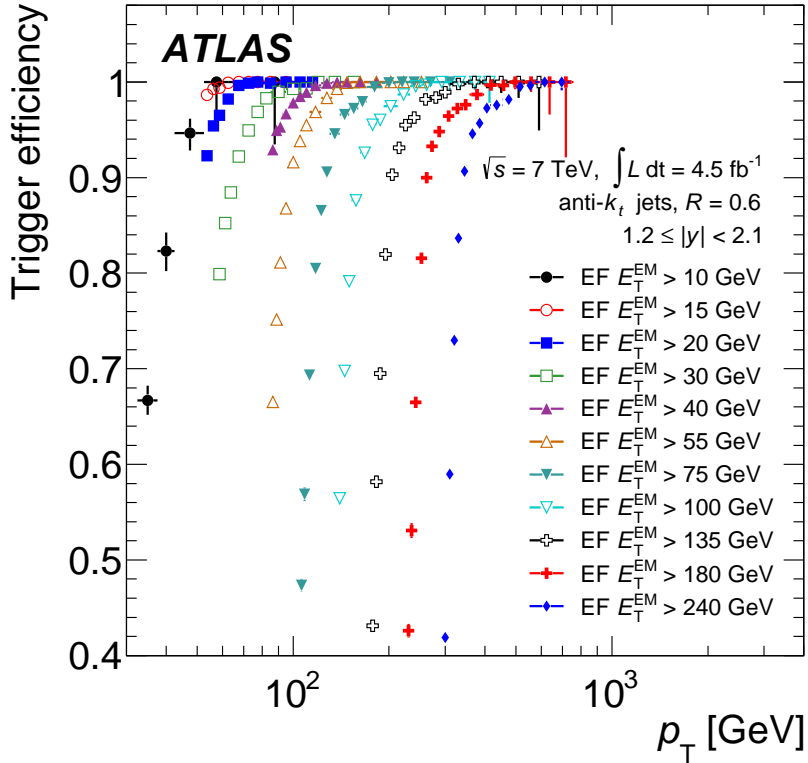


Figure 2. Jet trigger efficiency as a function of calibrated jet p_T for jets in the interval $1.2 \leq |y| < 2.1$ with radius parameter $R = 0.6$, shown for various trigger thresholds. The energy of jets in the trigger system is measured at the electromagnetic energy scale (EM scale), which correctly measures the energy deposited by electromagnetic showers.

in the sample size of about 10%. To properly account for the combined prescale of two overlapping triggers the “inclusion method for fully efficient combinations” described in ref. [55] is used.

After events are selected by the trigger system, they are fully reconstructed offline. The input objects to the jet algorithm are three-dimensional “topological” clusters [56] corrected to the electromagnetic energy scale.

Each cluster is constructed from a seed calorimeter cell with $|E_{\text{cell}}| > 4\sigma$, where σ is the RMS of the total noise of the cell from both electronic and pileup sources. Neighbouring cells are iteratively added to the cluster if they have $|E_{\text{cell}}| > 2\sigma$. Finally, an outer layer of all surrounding cells is added. A calibration that accounts for dead material, out-of-cluster losses for pions, and calorimeter response, is applied to clusters identified as hadronic by their topology and energy density [57]. This additional calibration serves to improve the energy resolution from the jet-constituent level through the clustering and calibration steps. Taken as input to the anti- k_t jet reconstruction algorithm, each cluster is considered as a massless particle with an energy $E = \sum E_{\text{cell}}$, and a direction given by the energy-weighted

barycentre of the cells in the cluster with respect to the geometrical centre of the ATLAS detector.

The four-momentum of an uncalibrated jet is defined as the sum of four-momenta of the clusters making up the jet. The jet is then calibrated in four steps:

1. Additional energy due to pileup is subtracted using a correction derived from MC simulation and validated in situ as a function of $\langle\mu\rangle$, the number of primary vertices (N_{PV}) in the bunch crossing, and jet η [58].
2. The direction of the jet is corrected such that the jet originates from the selected hard-scatter vertex of the event instead of the geometrical centre of ATLAS.
3. Using MC simulation, the energy and the position of the jet are corrected for instrumental effects (calorimeter non-compensation, additional dead material, and effects due to the magnetic field) and the jet energy scale is restored on average to that of the particle-level jet. For the calibration, the particle-level jet does not include muons and non-interacting particles.
4. An additional in situ calibration is applied to correct for residual differences between MC simulation and data, derived by combining the results of γ -jet, Z -jet, and multijet momentum balance techniques.

The full calibration procedure is described in detail in ref. [9].

The jet acceptance is restricted to $|y| < 3.0$ so that the trigger efficiency remains $> 99\%$. Furthermore, the leading jet is required to have $p_{\text{T}} > 100$ GeV and the subleading jet is required to have $p_{\text{T}} > 50$ GeV to be consistent with the asymmetric cuts imposed on the theoretical predictions.

Part of the data-taking period was affected by a read-out problem in a region of the LAr calorimeter, causing jets in this region to be poorly reconstructed. Since the same unfolding procedure is used for the entire data sample, events are rejected if either the leading or the subleading jet falls in the region $-0.88 < \phi < -0.5$, for all $|\eta|$, in order to avoid a bias in the spectra. This requirement results in a loss in acceptance of approximately 10%. The inefficiency is accounted for and corrected in the data unfolding procedure.

The leading and subleading jets must also fulfil the “medium” quality criteria as described in ref. [59], designed to reject cosmic rays, beam halo, and detector noise. If either jet fails these criteria, the event is not considered. More than four (two) million dijet events are selected with these criteria using jets with radius parameter $R = 0.4$ ($R = 0.6$), with the difference in sample size resulting mostly from the trigger requirements.

8 Stability of the results under pileup conditions

The dijet mass is sensitive to the effects of pileup through the energies, and to a lesser extent the directions, of the leading and subleading jets. As such, it is important to check the stability of the measurement with respect to various pileup conditions. The effects of pileup are removed at the per-jet level during the jet energy calibration (see section 7). To

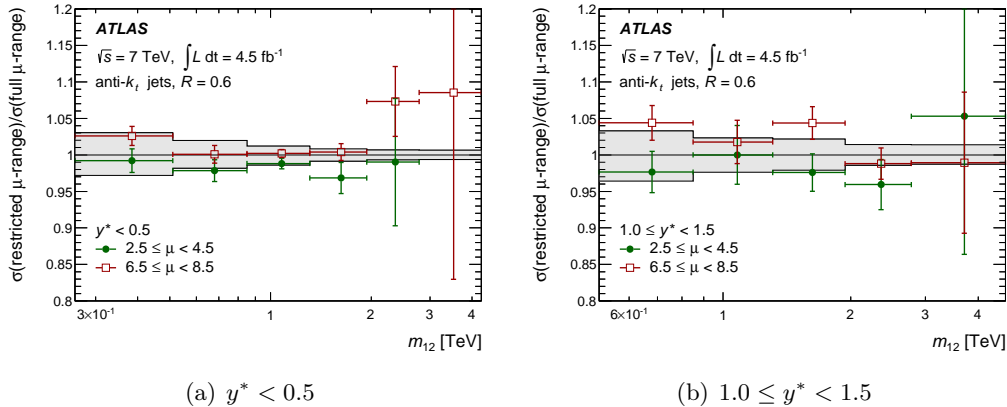


Figure 3. Luminosity-normalized dijet yields as a function of dijet mass for two ranges of μ , in the range (a) $y^* < 0.5$ and (b) $1.0 \leq y^* < 1.5$. The measurements are shown as ratios with respect to the full luminosity-normalized dijet yields. The gray bands represent the uncertainty on the jet energy calibration that accounts for the $\langle\mu\rangle$ and N_{PV} dependence, propagated to the luminosity-normalized dijet yields. The statistical uncertainty shown by the error bars is propagated assuming no correlations between the samples. This approximation has a small impact, and does not reduce the agreement observed within the pileup uncertainties.

check for any remaining effects, the integrated luminosity delivered for several ranges of μ is determined separately for each trigger used in this analysis. This information is then used to compute the luminosity-normalized dijet yields in different ranges of μ . A comparison of the yields for two ranges of μ is shown in figure 3. While statistical fluctuations are present, the residual bias is covered by the uncertainties on the jet energy calibration due to $\langle\mu\rangle$ and N_{PV} , derived through the in situ validation studies (see section 10) [9, 58].

The dependence of the luminosity-normalized dijet yields on the position in the accelerator bunch train is also studied. Because the first bunches in a train do not fully benefit from the compensation of previous bunches due to the long LAr calorimeter pulses, a bias is observed in the jet energy calibration. This bias can be studied by defining a control region using only events collected from the middle of the bunch train, where full closure in the jet energy calibration is obtained. By comparing the luminosity-normalized dijet yields using the full sample to that from the subsample of events collected from the middle of the bunch train, any remaining effects on the measurement due to pileup are estimated. An increase in the luminosity-normalized dijet yields using the full sample compared to the subsample from the middle of the bunch train is observed, up to 5% at low dijet mass. This increase is well described in the MC simulation, so that the effect is corrected for during the unfolding step. All remaining differences are covered by the jet energy calibration uncertainty components arising from pileup.

The stability of the luminosity-normalized dijet yields in the lowest dijet-mass bins is studied as a function of the date on which the data were collected. Since portions of

the hadronic calorimeter became non-functional during the course of running⁴ and pileup increased throughout the year, this provides an important check of the stability of the result. The observed variations are consistent with those due to μ , which on average increased until the end of data taking. Pileup is found to be the dominant source of variations, whereas detector effects are small in comparison.

9 Data unfolding

The cross-sections as a function of dijet mass are obtained by unfolding the data distributions, correcting for detector resolutions and inefficiencies, as well as for the presence of muons and neutrinos in the particle-level jets (see section 4). The same procedure as in ref. [5] is followed, using the iterative, dynamically stabilized (IDS) unfolding method [8], a modified Bayesian technique. To account for bin-to-bin migrations, a transfer matrix is built from MC simulations, relating the particle-level and reconstruction-level dijet mass, and reflecting all the effects mentioned above. The matching is done in the m_{12} - y^* plane, such that only a requirement on the presence of a dijet system is made. Since migrations between neighbouring bins predominantly occur due to jet energy resolution smearing the dijet mass, and less frequently due to jet angular resolution, the unfolding is performed separately for each range of y^* .

Data are unfolded to the particle level using a three-step procedure, consisting of correcting for matching inefficiency at the reconstruction level, unfolding for detector effects, and correcting for matching inefficiency at the particle level. The final result is given by the equation:

$$N_i^{\text{part}} = \sum_j N_j^{\text{reco}} \cdot \epsilon_j^{\text{reco}} A_{ij} / \epsilon_i^{\text{part}} \quad (9.1)$$

where i (j) is the particle-level (reconstruction-level) bin index, and N_k^{part} (N_k^{reco}) is the number of particle-level (reconstruction-level) events in bin k . The quantities ϵ_k^{reco} (ϵ_k^{part}) represent the fraction of reconstruction-level (particle-level) events matched to particle-level (reconstruction-level) events for each bin k . The element of the unfolding matrix, A_{ij} , provides the probability for a reconstruction-level event in bin j to be associated with a particle-level event in bin i . The transfer matrix is improved through a series of iterations, where the particle-level MC distribution is reweighted to the shape of the unfolded data spectrum. The number of iterations is chosen such that the bias in the closure test (see below) is at the sub-percent level. This is achieved after one iteration for this measurement.

The statistical uncertainties following the unfolding procedure are estimated using pseudo-experiments. Each event in the data is fluctuated using a Poisson distribution with a mean of one before applying any additional event weights. For the combination of this measurement with future results, the pseudo-random Poisson distribution is seeded uniquely for each event, so that the pseudo-experiments are fully reproducible. Each resulting pseudo-experiment of the data spectrum is then unfolded using a transfer matrix and efficiency corrections obtained by fluctuating each event in the MC simulation according to

⁴Up to 5% of the modules in the barrel and extended barrels of the hadronic calorimeter were turned off by the end of data taking.

a Poisson distribution. Finally, the unfolded pseudo-experiments are used to calculate the covariance matrix. In this way, the statistical uncertainty and bin-to-bin correlations for both the data and the MC simulation are encoded in the covariance matrix. For neighbour and next-to-neighbour bins the statistical correlations are generally 1–15%, although the systematic uncertainties are dominant. The level of statistical correlation decreases quickly for bins with larger dijet-mass separations.

A data-driven closure test is used to derive the bias of the spectrum shape due to mis-modelling by the MC simulation. The particle-level MC simulation is reweighted directly in the transfer matrix by multiplying each column of the matrix by a given weight. These weights are chosen to improve the agreement between data and reconstruction-level MC simulation. The modified reconstruction-level MC simulation is unfolded using the original transfer matrix, and the result is compared with the modified particle-level spectrum. The resulting bias is considered as a systematic uncertainty.⁵

10 Experimental uncertainties

The uncertainty on the jet energy calibration is the dominant uncertainty for this measurement. Complete details of its derivation can be found in ref. [9]. Uncertainties in the central region are determined from in situ calibration techniques, such as the transverse momentum balance in Z/γ -jet and multijet events, for which a comparison between data and MC simulation is performed. The uncertainty in the central region is propagated to the forward region using transverse momentum balance between a central and a forward jet in dijet events. The difference in the balance observed between MC simulation samples generated with PYTHIA and HERWIG results in an additional large uncertainty in the forward region. The uncertainty due to jet energy calibration on each individual jet is 1–4% in the central region, and up to 5% in the forward region. The improvement of the in situ jet calibration techniques over the single-particle response used for data taken in 2010 [62] leads to a reduction in the magnitude of the uncertainty compared to that achieved in the 2010 measurement, despite the increased level of pileup. As a result of the different techniques employed in the 2010 and current analyses, the correlations between the two measurements are non-trivial.

The uncertainty due to the jet energy calibration is propagated to the measured cross-sections using MC simulation. Each jet in the sample is scaled up or down by one standard deviation of a given uncertainty component, after which the luminosity-normalized dijet yield is measured from the resulting sample. The yields from the original sample and the samples where all jets were scaled are unfolded, and the difference is taken as the uncertainty due to that component. Since the sources of jet energy calibration uncertainty are taken as uncorrelated with each other, the corresponding uncertainty components on the cross-section are also taken as uncorrelated. Because the correlations between the various experimental uncertainty components are not perfectly known, two additional jet energy

⁵For this measurement the IDS method results in the smallest bias when compared with the bin-by-bin technique used in ref. [60] or the SVD method [61].

calibration uncertainty configurations are considered. They have *stronger* and *weaker* correlations with respect to the nominal configuration, depending on the number of uncertainty sources considered as fully correlated or independent of one another [9].

Jet energy and angular resolutions are estimated using MC simulation, after using an angular matching of particle-level and reconstruction-level jets. The resolution is obtained from a Gaussian fit to the distribution of the ratio (difference) of reconstruction-level and particle-level jet energy (angle). Jet energy resolutions are cross-checked in data using in situ techniques such as the bisector method in dijet events [63], where good agreement is observed with MC simulation. The uncertainty on the jet energy resolution comes from varying the selection parameters for jets, such as the amount of nearby jet activity, and depends on both jet p_T and jet η . The jet angular bias is found to be negligible, while the resolution varies between 0.005 radians and 0.07 radians. An uncertainty of 10% on the jet angular resolution is shown to cover the observed differences in a comparison between data and MC simulation.

The resolution uncertainties are propagated to the measured cross-sections through the transfer matrix. All jets in the MC sample are smeared according to the uncertainty on the resolution, either the jet energy or jet angular variable. To reduce the dependence on the MC sample size, this process is repeated for each event 1000 times. The transfer matrix resulting from this smeared sample is used to unfold the luminosity-normalized dijet yields, and the deviation from the measured cross-sections unfolded using the original transfer matrix is taken as a systematic uncertainty.

The uncertainty due to the jet reconstruction inefficiency as a function of jet p_T is estimated by comparing the efficiency for reconstructing a calorimeter jet, given the presence of an independently measured track-jet of the same radius, in data and in MC simulation. Here, a track-jet refers to a jet reconstructed using the anti- k_t algorithm, considering as input all tracks in the event with $p_T > 500$ MeV and $|\eta| < 2.5$, and which are assumed to have the mass of a pion. Since this method relies on tracking, its application is restricted to the acceptance of the tracker for jets of $|\eta| < 1.9$. For jets with $p_T > 50$ GeV, relevant for this analysis, the reconstruction efficiency in both the data and the MC simulation is found to be 100% for this rapidity region, leading to no additional uncertainty. The same efficiency is assumed for the forward region, where jets have more energy for a given value of p_T ; therefore, their reconstruction efficiency is likely to be as good as or better than that of jets in the central region.

Comparing the jet quality selection efficiency for jets passing the “medium” quality criteria in data and MC simulation, an agreement of the efficiency within 0.25% is found [59]. Because two jets are considered for each dijet system, a 0.5% systematic uncertainty on the cross-sections is assigned.

The impact of a possible mis-modelling of the spectrum shape in MC simulation, introduced through the unfolding as described in section 9, is also included. The luminosity uncertainty is 1.8% [54] and is fully correlated between all data points.

The bootstrap method [64] has been used to evaluate the statistical significance of all systematic uncertainties described above. The individual uncertainties are treated as fully correlated in dijet mass and y^* , but uncorrelated with each other, for the quantitative

comparison described in section 11. The total uncertainty ranges from 10% at low dijet mass up to 25% at high dijet mass for the range $y^* < 0.5$, and increases for larger y^* .

11 Frequentist method for a quantitative comparison of data and theory spectra

The comparison of data and theoretical predictions at the particle level rather than at the reconstruction level has the advantage that data can be used to test any theoretical model without the need for further detector simulation. Because the additional uncertainties introduced by the unfolding procedure are at the sub-percent level, they do not have a significant effect on the power of the comparison. The frequentist method described here provides quantitative statements about the ability of SM predictions to describe the measured cross-sections. An extension, based on the *CLs* technique [65], is used to explore potential deviations in dijet production due to contributions beyond the SM (see section 13).

11.1 Test statistic

The test statistic, which contains information about the degree of deviation of one spectrum from another, is the key input for any quantitative comparison. The use of a simple χ^2 test statistic such as

$$\chi^2(\mathbf{d}; \mathbf{t}) = \sum_i \left(\frac{d_i - t_i}{\sigma_i(t_i)} \right)^2, \quad (11.1)$$

comparing data (\mathbf{d}) and theoretical predictions (\mathbf{t}), accounts only for the uncertainties on individual bins (σ_i). This ignores the statistical and, even stronger, systematic correlations between bins. Therefore, it has a reduced sensitivity to the differences between theoretical predictions and the measurements compared to other more robust test statistics.

The use of a covariance matrix (C) in the χ^2 definition,

$$\chi^2(\mathbf{d}; \mathbf{t}) = \sum_{i,j} (d_i - t_i) \cdot [C^{-1}(\mathbf{t})]_{ij} \cdot (d_j - t_j), \quad (11.2)$$

is a better approximation. However, the covariance matrix is built from symmetrized uncertainties and thus cannot account for the asymmetries between positive and negative uncertainty components.

An alternative χ^2 definition, based on fits of the uncertainty components, was proposed in refs. [66] and [67]. For symmetric uncertainties it is equivalent to the definition in eq. (11.2) [68]. However, it allows a straightforward generalization of the χ^2 statistic, accounting for asymmetric uncertainties by separating them from the symmetric ones in the test statistic, which is now:

$$\chi^2(\mathbf{d}; \mathbf{t}) = \min_{\beta_a} \left\{ \sum_{i,j} \left[d_i - \left(1 + \sum_a \beta_a \cdot (\epsilon_a^\pm(\beta_a))_i \right) t_i \right] \cdot [C_{\text{su}}^{-1}(\mathbf{t})]_{ij} \cdot \left[d_j - \left(1 + \sum_a \beta_a \cdot (\epsilon_a^\pm(\beta_a))_j \right) t_j \right] + \sum_a \beta_a^2 \right\}, \quad (11.3)$$

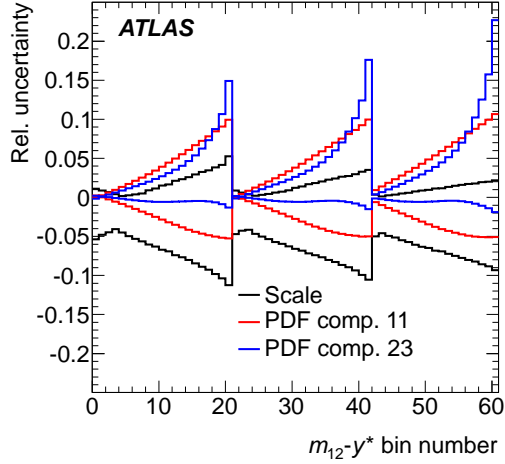
where C_{su} is the covariance matrix built using only the *symmetric* uncertainties, and β_a are the profiled coefficients of the *asymmetric* uncertainties which are varied in a fit that minimizes the χ^2 . Here ϵ_a^\pm is the positive component of the a^{th} asymmetric relative uncertainty if the fitted value of β_a is positive, or the negative component otherwise. The magnitude of each ϵ_a^\pm corresponds to the relative effect on the theory prediction of a one standard deviation shift of parameter a . For this analysis, an uncertainty component is considered asymmetric when the absolute difference between the magnitudes of the positive and negative portions is larger than 1% of the cross-section in at least one bin. Due to the large asymmetric uncertainties on the theoretical predictions, this χ^2 definition is not only a better motivated choice, but provides stronger statistical power than the two approaches mentioned above.

The theoretical and experimental uncertainties, including both statistical and systematic components, are included in the χ^2 fit. This relies on a detailed knowledge of the individual uncertainty components and their correlations with each other. Sample inputs to the χ^2 function using the SM predictions based on the CT10 PDF set are shown in figure 4. To illustrate the asymmetries, examples of the most asymmetric uncertainty components are shown, namely the theoretical uncertainties due to the scale choice and two uncertainty components of the CT10 PDF set. The positive and negative relative uncertainties are shown in figure 4(a) as functions of the bin number, corresponding to those in the cross-section tables in Appendix A. The signed difference between the magnitudes of the positive and negative relative uncertainties ($up - (-down)$) are shown in figure 4(b) as functions of the bin number. The importance of the asymmetric uncertainties is highlighted in figure 4(c) through the comparison of the relative total symmetric uncertainty with the relative total uncertainty. Uncertainty components exhibiting asymmetries of up to 22% are present, and are an important fraction of the total uncertainty, in particular at high dijet mass. The largest asymmetric uncertainties are individually comparable to the size of the total symmetric ones. The correlation matrix computed for the symmetric uncertainties is shown in figure 4(d). Strong correlations of 90% or more are observed among neighbouring bins of dijet mass, mostly due to the jet energy scale and resolution, while correlations are smaller between different ranges of y^* . The total symmetric uncertainty and its correlation matrix define the symmetric covariance matrix in eq. (11.3).

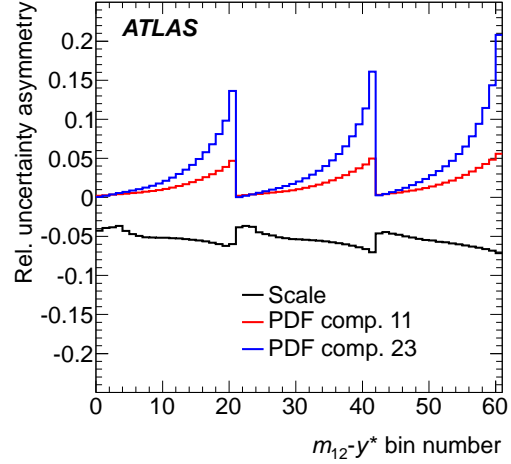
11.2 Frequentist method

The χ^2 distribution expected for experiments drawn from the parent distribution of a given theory hypothesis is required in order to calculate the probability of measuring a specific χ^2 value under that theory hypothesis. This is obtained by generating a large set of pseudo-experiments that represent fluctuations of the theory hypothesis due to the full set of experimental and theoretical uncertainties. The theory hypothesis can be the SM, or the SM with any of its extensions, depending on the study being carried out. In the generation of pseudo-experiments, the following sources of uncertainty are considered:

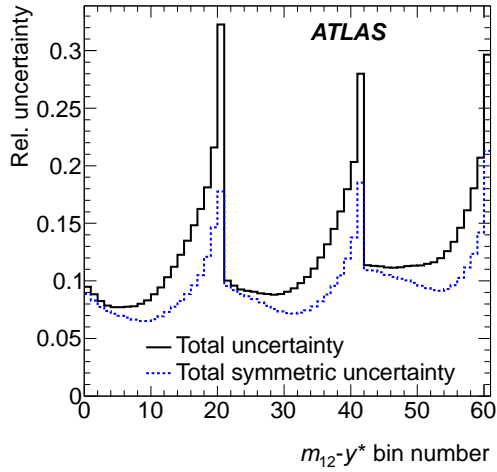
- **Statistical uncertainties:** an eigenvector decomposition of the statistical covariance matrix resulting from the unfolding procedure is performed. The resulting eigenvec-



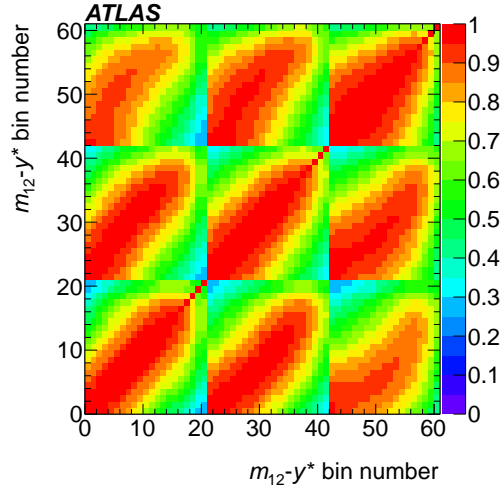
(a) Asymmetric uncertainties.



(b) Asymmetry of the uncertainties.



(c) Relative total uncertainty (black) and relative total symmetric uncertainty (blue).



(d) Correlation matrix for the symmetric uncertainties (statistical and systematic).

Figure 4. Sample inputs to the asymmetric generalization of the χ^2 function. The uncertainty components with the largest asymmetries are shown in (a), which includes the renormalization and factorization scale, and two uncertainty components (PDF comp.) of the CT10 PDF set. The asymmetries of the same uncertainty components are shown in (b), defined as the signed difference between the magnitudes of the positive and negative portions ($up - (-down)$). The relative total symmetric uncertainty (blue dashed line) and relative total uncertainty (black line) are shown in (c), along with the correlation matrix computed from the symmetric uncertainties in (d). These plots correspond to the theoretical prediction using the CT10 PDF set, and radius parameter $R = 0.6$. For each plot, the horizontal axis covers all dijet-mass bins (ordered according to increasing dijet mass) for three ranges in y^* : starting from the left end the range $y^* < 0.5$, then $0.5 \leq y^* < 1.0$ and finally $1.0 \leq y^* < 1.5$. The $m_{12}-y^*$ bin numbers correspond to those in the cross-section tables in Appendix A.

tors are taken as Gaussian-distributed uncertainty components.

- Systematic experimental and theoretical uncertainties: the symmetric components are taken as Gaussian distributed, while a two-sided Gaussian distribution is used for the asymmetric ones.

For each pseudo-experiment, the χ^2 value is computed between the pseudo-data and the theory hypothesis. In this way, the χ^2 distribution that would be expected for experiments drawn from the theory hypothesis is obtained without making assumptions about its shape.

The *observed* χ^2 (χ_{obs}^2) value is computed using the data and the theory hypothesis. To quantify the compatibility of the data with the theory, the ratio of the area of the χ^2 distribution with $\chi^2 > \chi_{\text{obs}}^2$ to the total area is used. This fractional area, called a p-value, is the observed probability, under the assumption of the theory hypothesis, to find a value of χ^2 with equal or lesser compatibility with the hypothesis relative to what is found with χ_{obs}^2 . If the observed p-value (P_{obs}) is smaller than 5%, the theoretical prediction is considered to poorly describe the data at the 95% CL.

The comparison of a theory hypothesis that contains an extension of the SM to the data is quantified using the *CLs* technique [65], which accounts for cases where the signal is small compared to the background. This technique relies on the computation of two χ^2 distributions: one corresponding to the *background* model (the SM) and another to the *signal+background* model (the SM plus any extension), each with respect to the assumption of the signal+background model. These distributions are calculated using the same technique described earlier, namely through the generation of large sets of pseudo-experiments:

- In the case of the background-only distribution, the χ^2 values are calculated between each background pseudo-experiment and the signal+background prediction. The *expected* χ^2 (χ_{exp}^2) is defined as the median of this χ^2 distribution.
- In the case of the signal+background distribution, the χ^2 values are calculated between each signal+background pseudo-experiment and the signal+background prediction.

These two χ^2 distributions are subsequently used to calculate two p-values: (1) the observed signal+background p-value (p_{s+b}), which is defined in the same way as the one described above, i.e. the fractional area of the signal+background χ^2 distribution above χ_{obs}^2 ; and (2) the observed background p-value (p_b), which is defined as the fractional area of the background-only χ^2 distribution below χ_{obs}^2 and measures the compatibility of the background model with the data. In the *CLs* technique, these two p-values are used to construct the quantity $CLs = p_{s+b}/(1 - p_b)$, from which the decision to exclude a given signal+background prediction is made. The theory hypothesis is excluded at 95% CL if the quantity CLs is less than 0.05. This technique has the advantage, compared to the use of p_{s+b} alone, that theoretical hypotheses to which the data have little or no sensitivity are not excluded. For comparison, the expected exclusion is calculated using the same procedure, except using the expected χ^2 value instead of the observed χ^2 value.

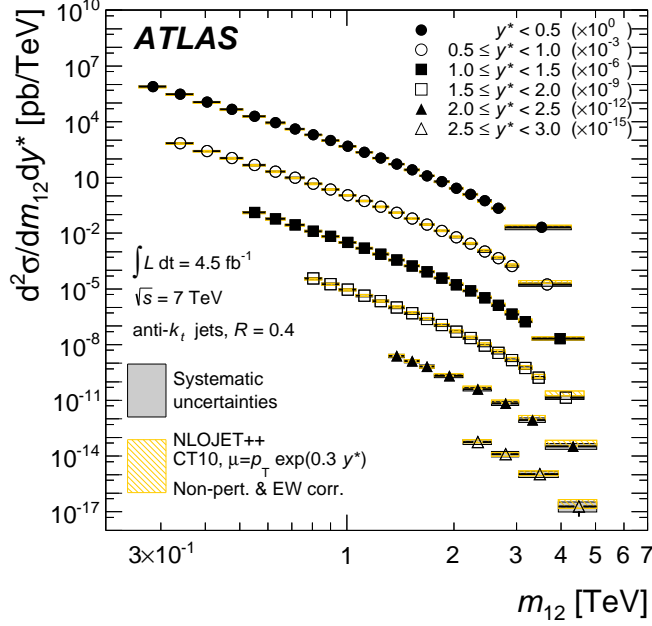
12 Cross-section results

Measurements of the dijet double-differential cross-sections as a function of dijet mass in various ranges of y^* are shown in figure 5 for anti- k_t jets with values of the radius parameter $R = 0.4$ and $R = 0.6$. The cross-sections are measured up to a dijet mass of 5 TeV and y^* of 3.0, and are seen to decrease quickly with increasing dijet mass. The NLO QCD calculations by NLOJet++ using the CT10 PDF set, which are corrected for non-perturbative and electroweak effects, are compared to the measured cross-sections. No major deviation of the data from the theoretical predictions is observed over the full kinematic range, covering almost eight orders of magnitude in measured cross-section values. More detailed quantitative comparisons are made between data and theoretical predictions in the following subsection. At a given dijet mass, the absolute cross-sections using jets with radius parameter $R = 0.4$ are smaller than those using $R = 0.6$. This is due to the smaller value of the jet radius parameter, resulting in a smaller contribution to the jet energy from the parton shower and the underlying event. Tables summarising the measured cross-sections are provided in Appendix A. The quadrature sum of the uncertainties listed in the tables is the total uncertainty on the measurement, although the in situ, pileup, and flavour columns are each composed of two or more components. The full set of cross-section values and uncertainty components, each of which is fully correlated in dijet mass and y^* but uncorrelated with the other components, can be found in HepData [16].

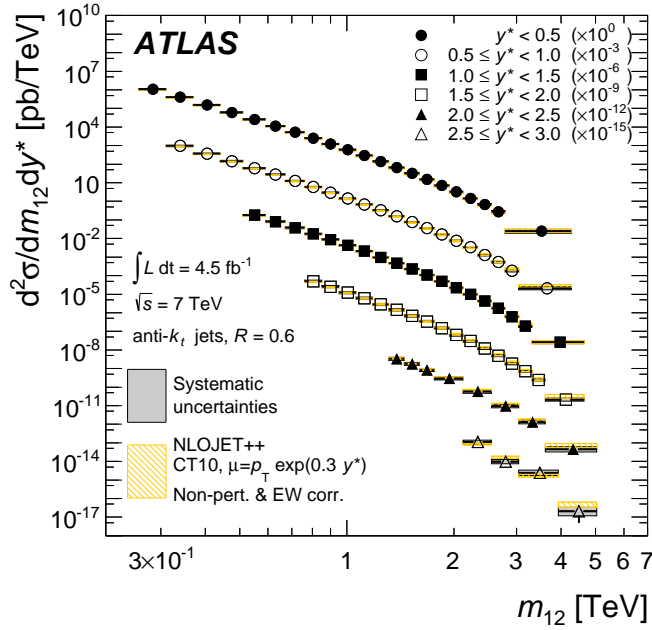
12.1 Quantitative comparison with NLOJet++ predictions

The ratio of the NLO QCD predictions from NLOJet++, corrected for non-perturbative and electroweak effects, to the data is shown in figures 6–9 for various PDF sets. The CT10, HERAPDF1.5, epATLJet13, MSTW 2008, NNPDF2.3, and ABM11 PDF sets are used. As discussed in section 10, the individual experimental and theoretical uncertainty components are fully correlated between m_{12} and y^* bins. As such, the frequentist method described in section 11 is necessary to make quantitative statements about the agreement of theoretical predictions with data. For this measurement, the NLOJet++ predictions using the MSTW 2008, NNPDF2.3 and ABM11 PDF sets have smaller theoretical uncertainties than those using the CT10 and HERAPDF1.5 PDF sets. Due to the use of ATLAS jet data in the PDF fit, the predictions using the epATLJet13 PDF set have smaller uncertainties at high dijet mass compared to those using the HERAPDF1.5 PDF set, when only considering the uncertainties due to the experimental inputs for both.

The frequentist method is employed using the hypothesis that the SM is the underlying theory. Here, the NNPDF2.1 PDF set is considered instead of NNPDF2.3 due to the larger number of replicas available, which allows a better determination of the uncertainty components. The epATLJet13 PDF set is not considered since the full set of uncertainties is not available. The resulting observed p-values are also shown in figures 6–9, where all m_{12} bins are considered in each range of y^* separately. The agreement between the data and the various theories is good (observed p-value greater than 5%) in all cases, except the following. For the predictions using HERAPDF1.5, the smallest observed p-values are seen in the range $1.0 \leq y^* < 1.5$ for jets with radius parameter $R = 0.4$, and in the range



(a) $R = 0.4$



(b) $R = 0.6$

Figure 5. Dijet double-differential cross-sections for anti- k_t jets with radius parameter $R = 0.4$ and $R = 0.6$, shown as a function of dijet mass in different ranges of y^* . To aid visibility, the cross-sections are multiplied by the factors indicated in the legend. The error bars indicate the statistical uncertainty on the measurement, and the dark shaded band indicates the sum in quadrature of the experimental systematic uncertainties. For comparison, the NLO QCD predictions of NLOJet++ using the CT10 PDF set, corrected for non-perturbative and electroweak effects, are included. The renormalization and factorization scale choice μ is as described in section 6. The hatched band shows the uncertainty associated with the theory predictions. Because of the logarithmic scale on the vertical axis, the experimental and theoretical uncertainties are only visible at high dijet mass, where they are largest.

$0.5 \leq y^* < 1.0$ for jets with radius parameter $R = 0.6$, both of which are $< 5\%$. For the predictions using ABM11, the observed p-value is $< 0.1\%$ for each of the first three ranges of $y^* < 1.5$, for both values of jet radius parameter. The results using the ABM11 PDF set also show observed p-values of less than 5%, for the range $2.0 \leq y^* < 2.5$ for jets with radius parameter $R = 0.4$, and $1.5 \leq y^* < 2.0$ for $R = 0.6$ jets.

Figure 10 shows the χ^2 distribution from pseudo-experiments for the SM hypothesis using the CT10 PDF set, as well as the observed χ^2 value. The full range of dijet mass in the first three ranges of $y^* < 1.5$, for jets with radius parameter $R = 0.6$, is considered. The mean, median, $\pm 1\sigma$ and $\pm 2\sigma$ regions of the χ^2 distribution from pseudo-experiments around the median, and number of degrees of freedom are also indicated. Figure 10(b) shows that a broadening of the χ^2 distribution from pseudo-experiments is observed when additional degrees of freedom are included by combining multiple ranges of y^* . For both χ^2 distributions, the mean and median are close to the number of degrees of freedom. This shows that the choice of generalized χ^2 as the test statistic in the frequentist method behaves as expected.

Because the data at larger values of y^* are increasingly dominated by experimental uncertainties, the sensitivity to the proton PDFs is reduced. For this reason, when considering a combination only the first three ranges of $y^* < 1.5$ are used. While the low dijet-mass region provides constraints on the global normalization, due to the increased number of degrees of freedom it also introduces a broadening of the χ^2 distribution from the pseudo-experiments that reduces sensitivity to the high dijet-mass region. To focus on the regions where the PDF uncertainties are large while the data still provide a good constraint, the comparison between data and SM predictions is also performed using a high dijet-mass subsample. The high dijet-mass subsample is restricted to $m_{12} > 1.31$ TeV for $y^* < 0.5$, $m_{12} > 1.45$ TeV for $0.5 \leq y^* < 1.0$, and $m_{12} > 1.60$ TeV for $1.0 \leq y^* < 1.5$.

Table 1 presents a reduced summary of the observed p-values for the comparison of measured cross-sections and SM predictions in both the full and high dijet-mass regions using various PDF sets, for both values of the jet radius parameter. For the first three ranges of $y^* < 1.5$, as well as their combination, theoretical predictions using the CT10 PDF set have an observed p-value $> 6.6\%$ for all ranges of dijet mass, and are typically much larger than this. For the HERAPDF1.5 PDF set, good agreement is found at high dijet mass in the ranges $y^* < 0.5$ and $1.0 \leq y^* < 1.5$ (not shown), both with observed p-values $> 15\%$. Disagreement is observed for jets with distance parameter $R = 0.6$ when considering the full dijet-mass region for the first three ranges of $y^* < 1.5$ combined, where the observed p-value is 2.5%. This is due to the differences already noted for the range $0.5 \leq y^* < 1.0$, where the observed p-value is 0.9% (see figure 8). Disagreement is also seen when limiting to the high dijet-mass region and combining the first three ranges of $y^* < 1.5$, resulting in an observed p-value of 0.7%. The observed p-values for the MSTW 2008 and NNPDF2.1 PDF sets are always $> 12.5\%$ in the ranges shown in table 1. This is particularly relevant considering these two PDF sets provide small theoretical uncertainties at high dijet mass. A strong disagreement, where the observed p-value is generally $< 0.1\%$, is observed for the ABM11 PDF set for the first three ranges of $y^* < 1.5$ and both values of the jet radius parameter.

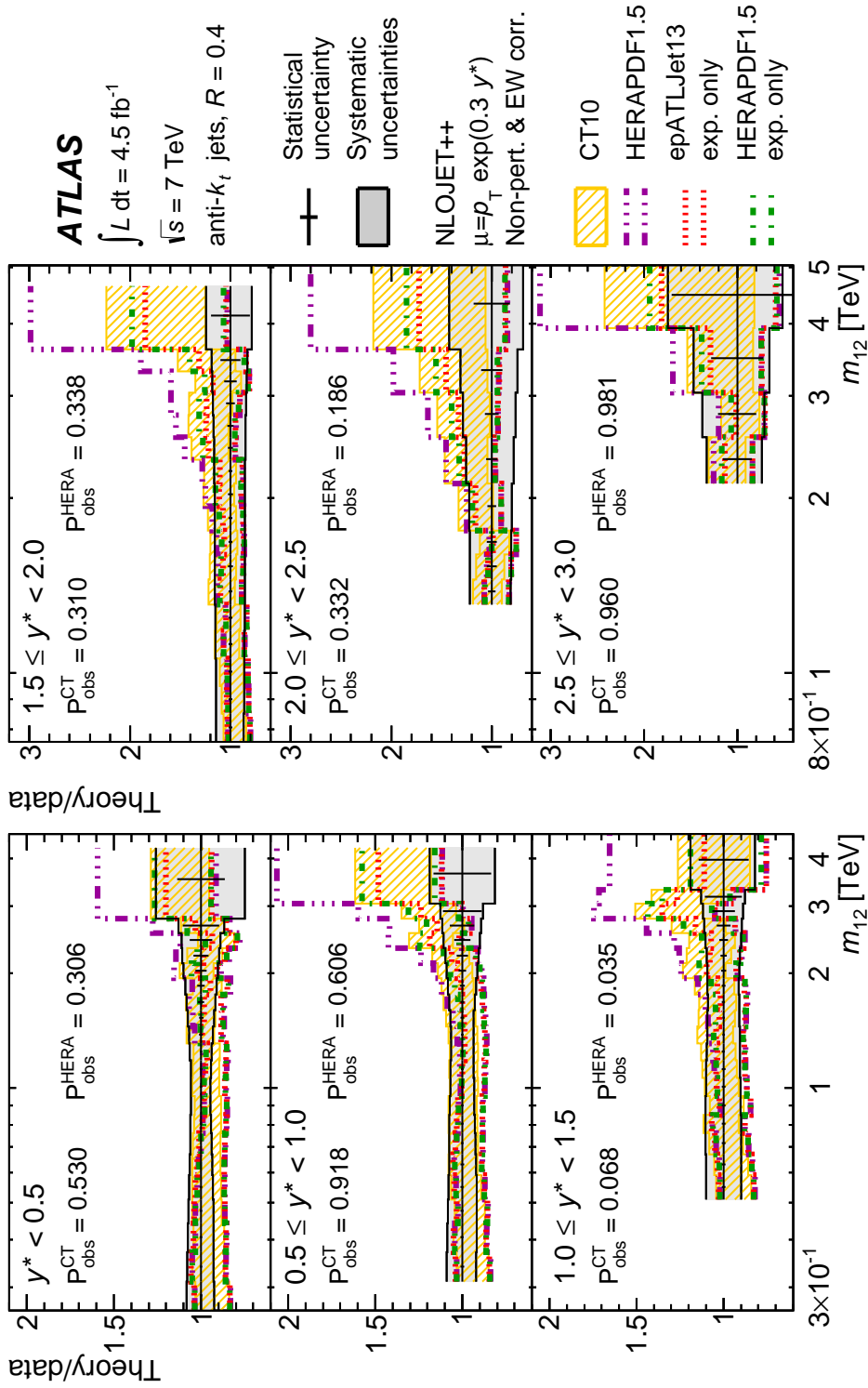


Figure 6. Ratio of the NLO QCD predictions of NLOJet++ to the measurements of the dijet double-differential cross-section as a function of dijet mass in different ranges of y^* . The results are shown for jets identified using the anti- k_t algorithm with radius parameter $R = 0.4$. The predictions of NLOJet++ using different PDF sets (CT10, HERAPDF1.5, and epATLJet13) are shown. The renormalization and factorization scale choice μ is as described in section 6. Observed p-values resulting from the comparison of theory with data are shown considering all m_{12} bins in each range of y^* separately. The HERAPDF1.5 analysis accounts for model and parameterization uncertainties as well as experimental uncertainties. The theoretical predictions are labelled with *exp. only* when the model and parameterization uncertainties are not included.

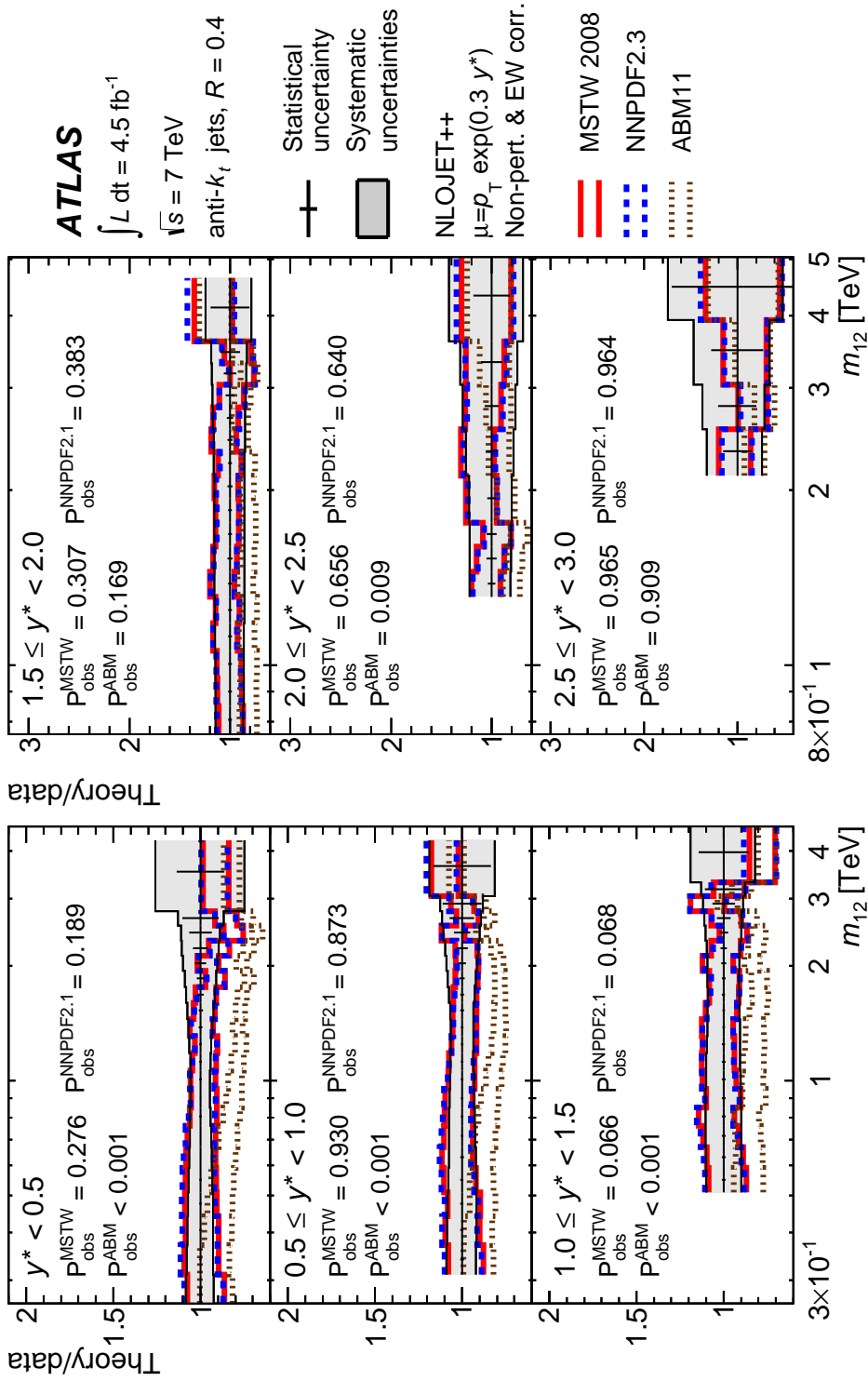


Figure 7. Ratio of the NLO QCD predictions of NLOJet++ to the measurements of the dijet double-differential cross-section as a function of dijet mass in different ranges of y^* . The results are shown for jets identified using the anti- k_t algorithm with radius parameter $R = 0.4$. The predictions of NLOJet++ using different PDF sets (MSTW 2008, NNPDF2.3 and ABM11) are shown. The renormalization and factorization scale choice μ is as described in section 6. Observed p-values resulting from the comparison of theory with data are shown considering all m_{12} bins in each range of y^* separately. Here, the observed p-value is shown for the NNPDF2.1 PDF set, while the lines are for the NNPDF2.3 PDF set (see text).

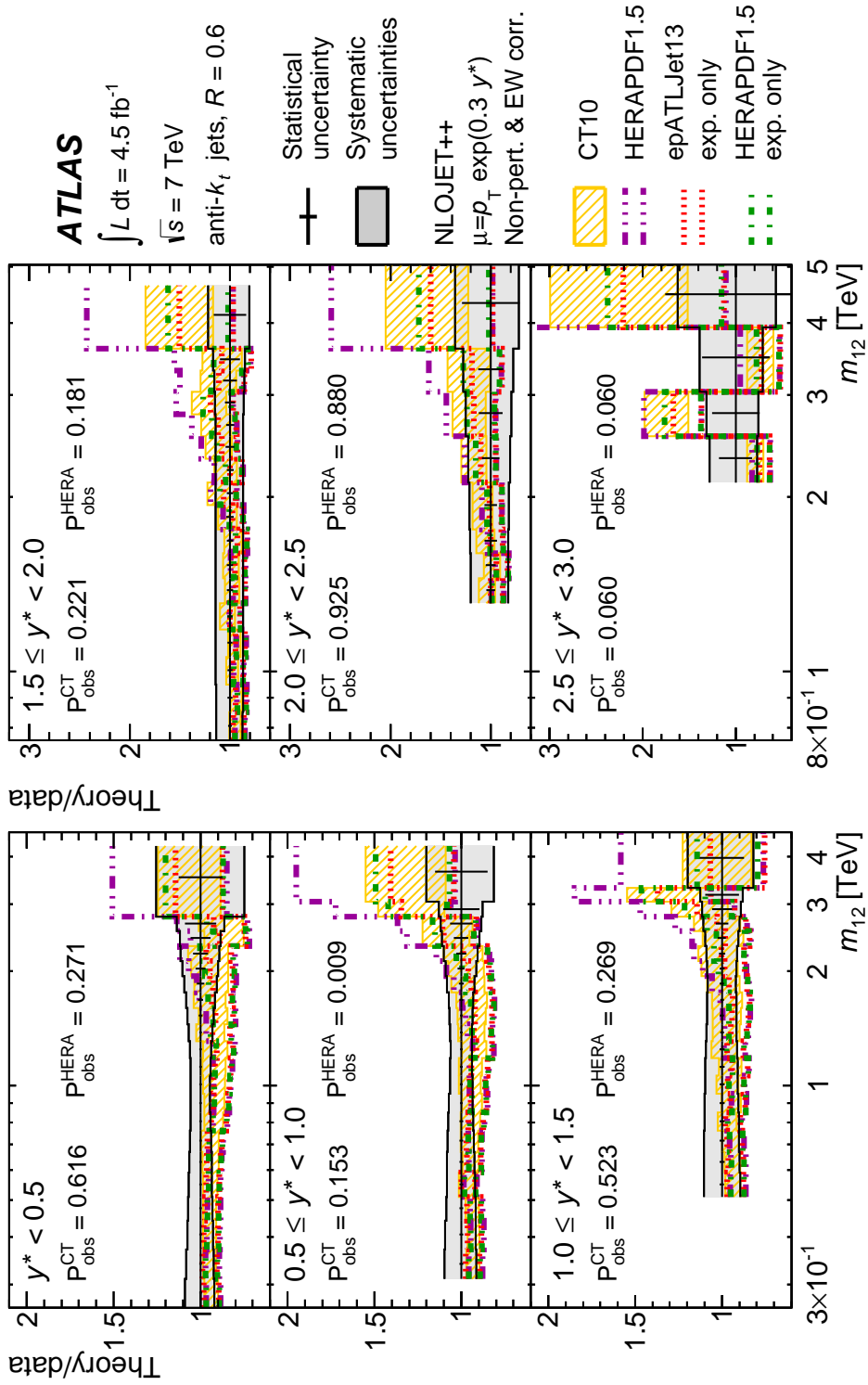


Figure 8. Ratio of the NLO QCD predictions of NLOJet++ to the measurements of the dijet double-differential cross-section as a function of dijet mass in different ranges of y^* . The results are shown for jets identified using the anti- k_t algorithm with radius parameter $R = 0.6$. The predictions of NLOJet++ using different PDF sets (CT10, HERAPDF1.5, and epATLJet13) are shown. The renormalization and factorization scale choice μ is as described in section 6. Observed p-values resulting from the comparison of theory with data are shown considering all m_{12} bins in each range of y^* separately. The HERAPDF1.5 analysis accounts for model and parameterization uncertainties as well as experimental uncertainties. The theoretical predictions are labelled with *exp. only* when the model and parameterization uncertainties are not included.

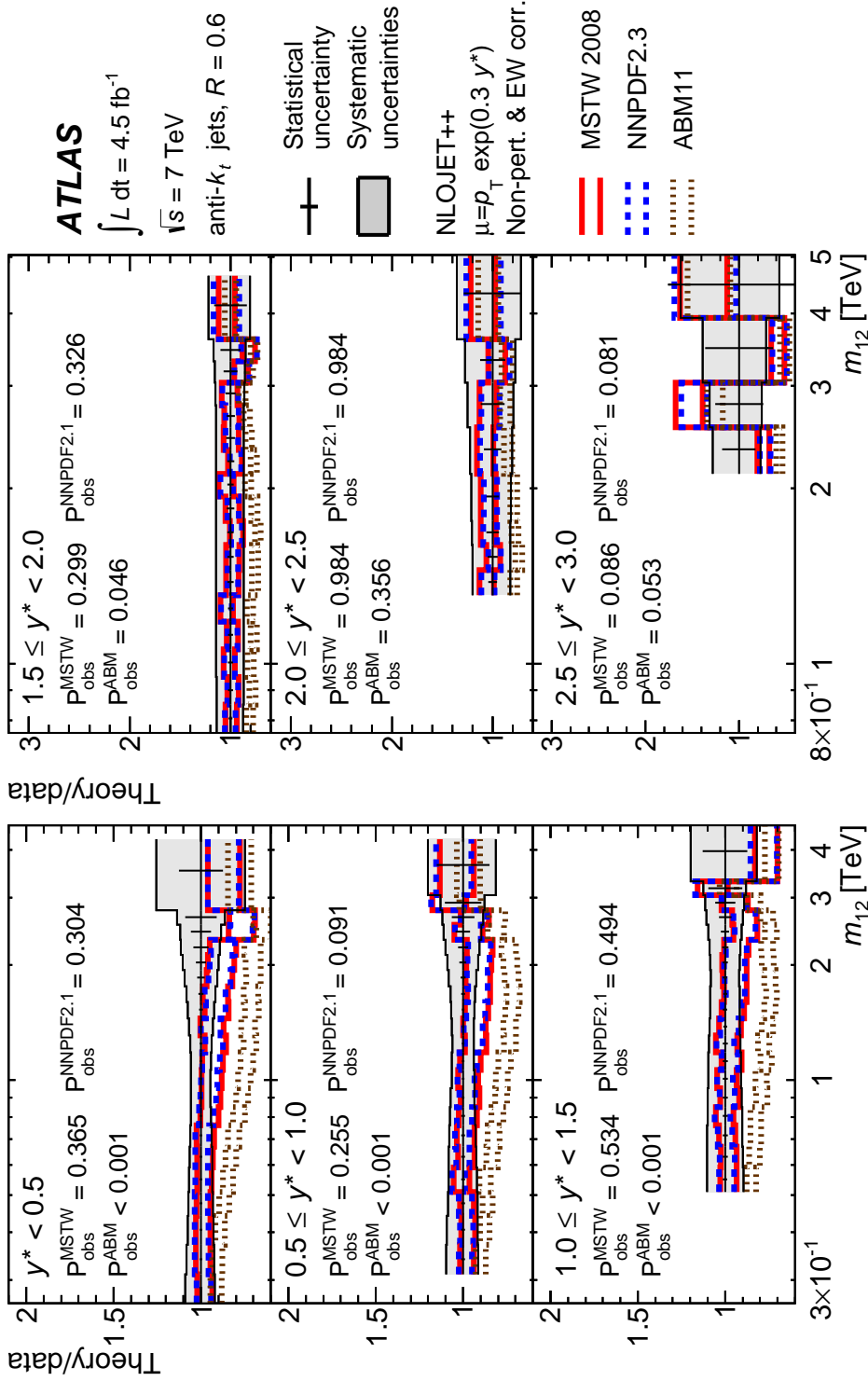
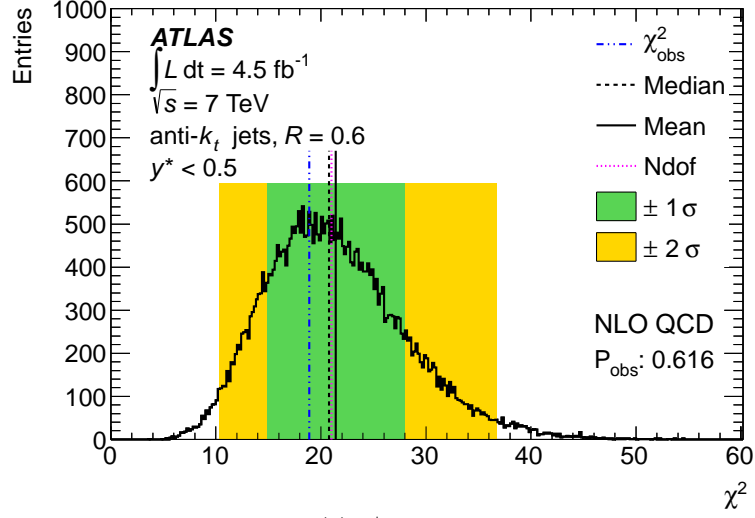
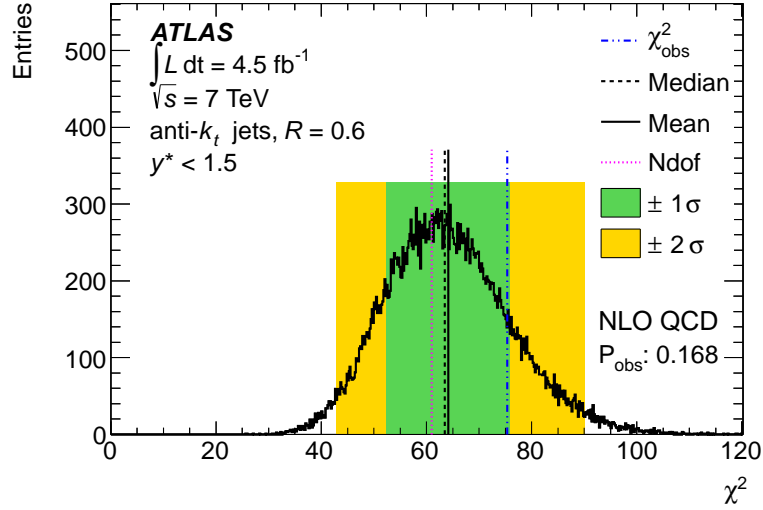


Figure 9. Ratio of the NLO QCD predictions of NLOJet++ to the measurements of the dijet double-differential cross-section as a function of dijet mass in different ranges of y^* . The results are shown for jets identified using the anti- k_t algorithm with radius parameter $R = 0.6$. The predictions of NLOJet++ using different PDF sets (MSTW 2008, NNPDF2.3 and ABM11) are shown. The renormalization and factorization scale choice μ is as described in section 6. Observed p-values resulting from the comparison of theory with data are shown considering all m_{12} bins in each range of y^* separately. Here, the observed p-value is shown for the NNPDF2.1 PDF set, while the lines are for the NNPDF2.3 PDF set (see text).



(a) $y^* < 0.5$



(b) $y^* < 1.5$

Figure 10. The χ^2 distribution of pseudo-experiments (black histogram) for NLO QCD using the CT10 PDF set. The renormalization and factorization scale choice μ is as described in section 6. The full information on the uncertainties, including their asymmetries and correlations, is used for both the pseudo-experiments and the χ^2 calculation. The black vertical dashed (solid) line indicates the median (mean) of the distribution, while the green (yellow) band indicates the $\pm 1\sigma$ ($\pm 2\sigma$) region. The blue dot-dashed vertical lines indicate the observed χ^2 , with the corresponding observed p-value given in the legend (see text). The pink dotted lines show the number of degrees of freedom, 21 for (a) and 61 for (b). The plots correspond to (a) the range $y^* < 0.5$, and (b) the first three ranges of $y^* < 1.5$ combined, for jets reconstructed with radius parameter $R = 0.6$.

PDF set	y^* ranges	mass range (full/high)	P_{obs}	
			$R = 0.4$	$R = 0.6$
CT10	$y^* < 0.5$	high	0.742	0.785
	$y^* < 1.5$	high	0.080	0.066
	$y^* < 1.5$	full	0.324	0.168
HERAPDF1.5	$y^* < 0.5$	high	0.688	0.504
	$y^* < 1.5$	high	0.025	0.007
	$y^* < 1.5$	full	0.137	0.025
MSTW 2008	$y^* < 0.5$	high	0.328	0.533
	$y^* < 1.5$	high	0.167	0.183
	$y^* < 1.5$	full	0.470	0.352
NNPDF2.1	$y^* < 0.5$	high	0.405	0.568
	$y^* < 1.5$	high	0.151	0.125
	$y^* < 1.5$	full	0.431	0.242
ABM11	$y^* < 0.5$	high	0.024	$< 10^{-3}$
	$y^* < 1.5$	high	$< 10^{-3}$	$< 10^{-3}$
	$y^* < 1.5$	full	$< 10^{-3}$	$< 10^{-3}$

Table 1. Sample of observed p-values obtained in the comparison between data and the NLO QCD predictions using the CT10, HERAPDF1.5, MSTW 2008, NNPDF2.1 and ABM11 PDF sets, with values of the jet radius parameter $R = 0.4$ and $R = 0.6$. Results are presented for the range $y^* < 0.5$, as well as the combination of the first three ranges of $y^* < 1.5$, performing the test in the full dijet-mass range or restricting it to the high dijet-mass subsample. The full information on uncertainties, including their asymmetries and correlations, is used for both the pseudo-experiments and the χ^2 calculation.

It is possible to further study the poor agreement observed at high dijet mass for the combination of the first three ranges of $y^* < 1.5$ when using the HERAPDF1.5 PDF set by exploring the four variations described in section 6.2. The observed p-values using variations 1, 2, and 4 in the NLOJet++ predictions, shown in table 2, are generally similar to those using the default HERAPDF1.5 PDF set. However, much smaller p-values are observed for variation 3, which has a more flexible parameterization for the valence u -quark contribution. Including the present dijet measurement in the PDF analysis should provide a better constraint on the choice of parameterization.

The studies described above, as well as most of the previously published analyses, use test statistics that exploit the information on the sizes and bin-to-bin correlations of the uncertainties. As such, the results are sensitive to the assumptions used to derive the uncorrelated uncertainty components, in particular those of the jet energy calibration. To improve upon previous studies, the analysis is repeated using the two different correlation assumptions described in section 10. Theoretical predictions using the CT10 PDF set in the range $y^* < 0.5$ for the high dijet-mass subsample, with jet radius parameter $R = 0.6$, are considered. For both the stronger and weaker correlation assumptions the observed p-values differ by $< 0.1\%$ from the value of 78.5% found using the default jet energy

PDF set	y^* ranges	mass range (full/high)	P_{obs}	
			$R = 0.4$	$R = 0.6$
HERAPDF1.5 variation 1	$y^* < 0.5$	high	0.692	0.493
	$y^* < 1.5$	high	0.018	0.005
	$y^* < 1.5$	full	0.113	0.018
variation 2	$y^* < 0.5$	high	0.667	0.453
	$y^* < 1.5$	high	0.025	0.008
	$y^* < 1.5$	full	0.124	0.024
variation 3	$y^* < 0.5$	high	0.424	0.209
	$y^* < 1.5$	high	$< 10^{-3}$	$< 10^{-3}$
	$y^* < 1.5$	full	0.001	$< 10^{-3}$
variation 4	$y^* < 0.5$	high	0.677	0.525
	$y^* < 1.5$	high	0.031	0.010
	$y^* < 1.5$	full	0.160	0.031

Table 2. Sample of observed p-values obtained in the comparison between data and the NLO QCD predictions based on the variations (described in section 6.2) of the HERAPDF1.5 PDF analysis, with values of the jet radius parameter $R = 0.4$ and $R = 0.6$. Results are presented for the range $y^* < 0.5$, as well as the combination of the first three ranges of $y^* < 1.5$, performing the test in the full dijet-mass range or restricting it to the high dijet-mass subsample. The full information on uncertainties, including their asymmetries and correlations, is used for both the pseudo-experiments and the χ^2 calculation.

calibration uncertainty components. This is because the impact on the total uncertainty and its correlations is only at the few-percent level for most bins, even though these assumptions lead to a relative change of up to 8% in the experimental uncertainty, and up to 12% in its correlations. Quantitative comparisons of theoretical predictions with data would benefit from alternative assumptions for the correlations of the theoretical uncertainties, in particular the large PDF uncertainty components.

12.2 Comparison with POWHEG predictions

The ratios of the theoretical predictions from POWHEG to data are shown in figures 11 and 12 for values of the jet radius parameter $R = 0.4$ and $R = 0.6$. Because of the difficulty in propagating multiple PDF sets through the POWHEG generation, direct calculations of the theoretical uncertainties are not made and only qualitative comparisons are provided. However, the theoretical uncertainties are expected to be similar to those shown for the NLOJet++ calculations using the CT10 PDF set.

The POWHEG predictions show no major deviations from data, with the Perugia 2011 tune resulting in slightly larger cross-sections (10–20%) than the AUET2B tune. At high dijet mass, the difference in the theory calculations is less pronounced, decreasing to a few percent at low values of y^* . For the range $y^* < 0.5$, theoretical predictions underestimate the measured cross-sections by up to 25% at larger values of dijet mass. In the range $0.5 \leq y^* < 1.0$, this difference at high dijet mass is less, at around 15%. At larger values of

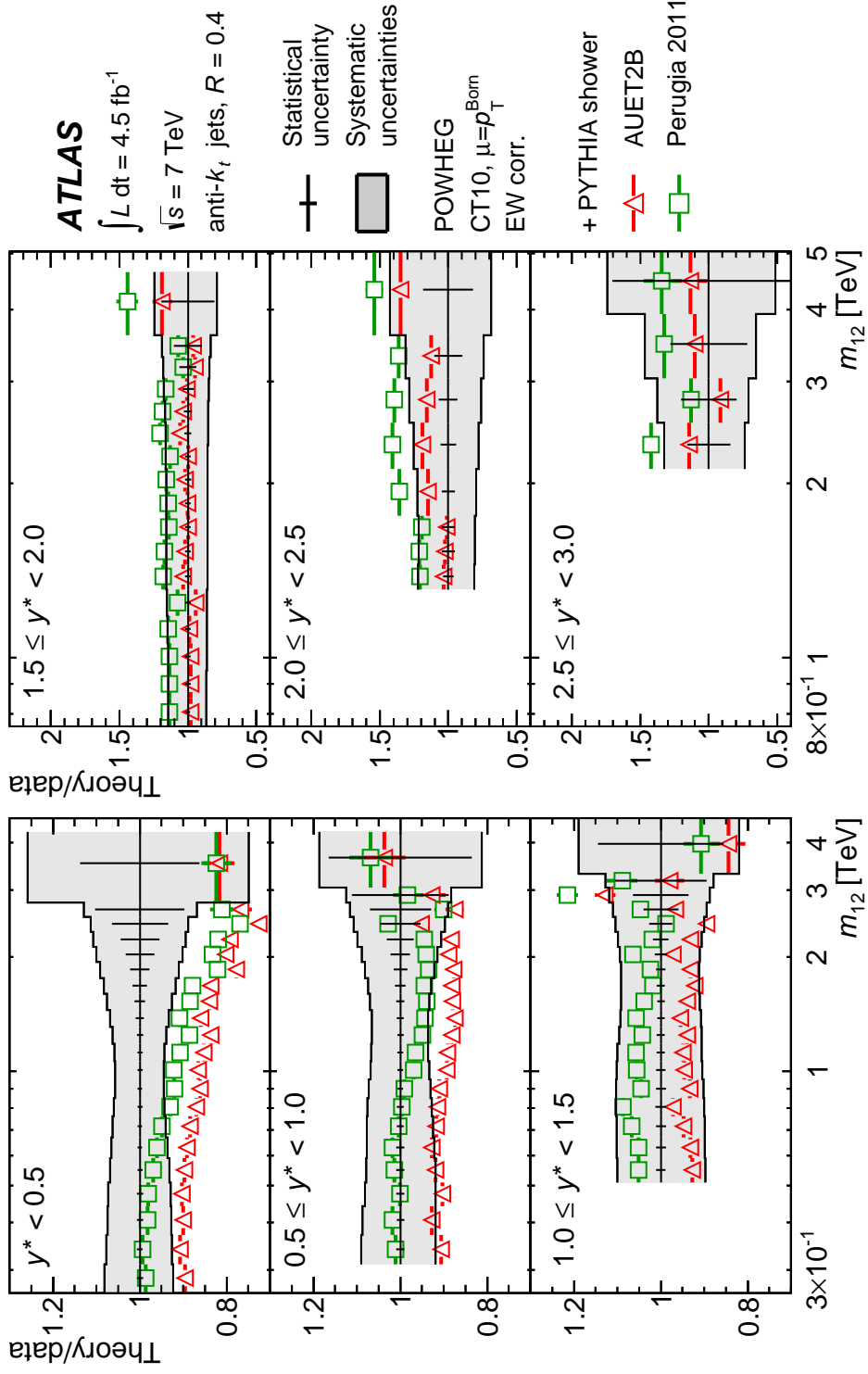


Figure 11. Ratio of the POWHEG predictions to the measurements of the dijet double-differential cross-sections as a function of dijet mass in different ranges of y^* . The results are shown for jets identified using the anti- k_t algorithm with jet radius parameter $R = 0.4$. The predictions of POWHEG with parton-shower MC simulation by PYTHIA are shown for the AUET2B and Perugia 2011 tunes. The statistical (total systematic) uncertainties of the measurements are indicated as error bars (shaded bands).

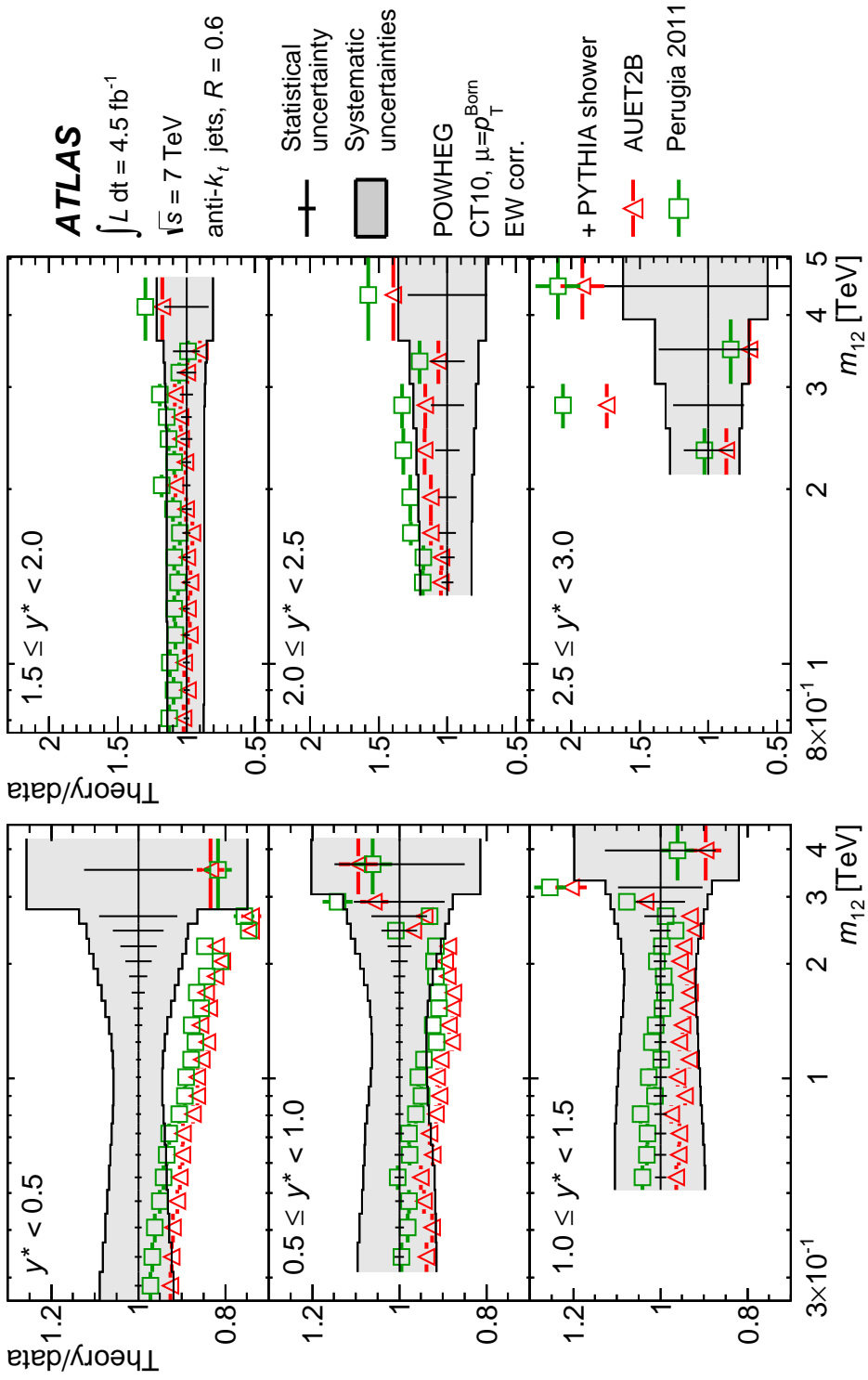


Figure 12. Ratio of the POWHEG predictions to the measurements of the dijet double-differential cross-sections as a function of dijet mass in different ranges of y^* . The results are shown for jets identified using the anti- k_t algorithm with jet radius parameter $R = 0.6$. The predictions of POWHEG with parton-shower MC simulation by PYTHIA are shown for the AUET2B and Perugia 2011 tunes. The statistical (total systematic) uncertainties of the measurements are indicated as error bars (shaded bands).

y^* , the experimental sensitivity decreases so that no strong statements can be made. The ratios of the theoretical predictions to the cross-section measurements using jets with radius parameter $R = 0.4$ are observed to be larger than those for $R = 0.6$. This is similar to the trend observed previously for inclusive jet cross-sections from ATLAS [5]. While this trend is particularly apparent for the Perugia 2011 tune, it is almost negligible for the AUET2B tune at high dijet mass.

13 Exploration and exclusion of contact interactions

To illustrate the sensitivity of the measurements to physics beyond the SM, the model of QCD plus contact interactions (CIs) [69] with left–left coupling and destructive interference between CIs and QCD as implemented by the CIJET program [70] is considered. The use of NLO QCD calculations for the CI portion unifies the treatment of the two predictions. For this study, the measurement is restricted to the high dijet-mass subsample $m_{12} > 1.31$ TeV in the range $y^* < 0.5$, where theory predicts the largest effect. Because QCD predicts a more uniform y^* distribution compared to CIs, where events are preferentially produced at smaller values of y^* , this region provides the highest sensitivity to the CI contribution. Furthermore, the additional QCD plus CIs matrix elements are sensitive to different quark–gluon compositions. Given that the positive electroweak corrections and the CIs produce similar contributions, the electroweak corrections are not applied to the CI portion. This results in a conservative approach when setting limits for the kinematic region considered here. Non-perturbative corrections are also not applied to the CI portion, but have a negligible size of less than 1% at high dijet mass where CI contributions are most significant. The PDF sets for which the SM predictions in this region provide a good description of the data are considered: CT10, HERAPDF1.5, MSTW 2008, and NNPDF2.1. Even when considering the ABM11 PDF set in only the low dijet-mass region $m_{12} < 1.31$ TeV, where CIs were previously excluded [71, 72], the observed p-value is $< 0.1\%$ in the range $y^* < 0.5$. For this reason, the ABM11 PDF set is not considered in this example.

Figure 13 shows the χ^2 distributions from pseudo-experiments for both the SM (background) and QCD plus CIs (signal+background), as well as the observed and expected χ^2 values. Here, the hypothesis for the χ^2 calculation is the prediction of QCD plus CIs using the CT10 PDF set with compositeness scale $\Lambda = 6.5$ TeV. For this example, jets with radius parameter $R = 0.6$ are considered. The observed p-value for the signal+background model, i.e. the integral of the distribution above the observed χ^2 , is significantly smaller than that obtained for the SM pseudo-data, resulting in an exclusion of the compositeness scale $\Lambda = 6.5$ TeV with a CLs value < 0.001 . Similar results are obtained for jets reconstructed with radius parameter $R = 0.4$, as well as for the MSTW 2008, NNPDF2.1 and HERAPDF1.5 PDF sets.

In order to exclude a range for the compositeness scale, a scan of the observed CLs value as a function of Λ is performed. This is shown in figure 14(a), whereas figure 14(b) shows the scan over Λ of the observed and expected χ^2 values from which the CLs values are derived. The observed and expected χ^2 values follow each other closely for small values of Λ , converging towards a constant difference in the limit $\Lambda \rightarrow \infty$. The scans are for the

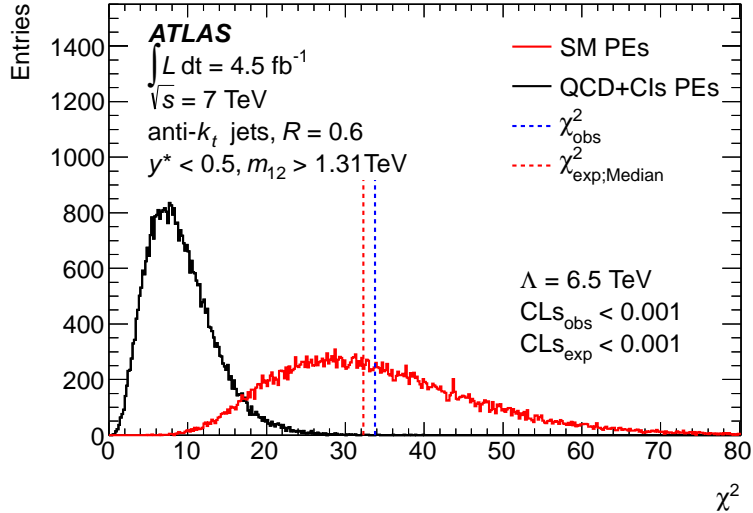
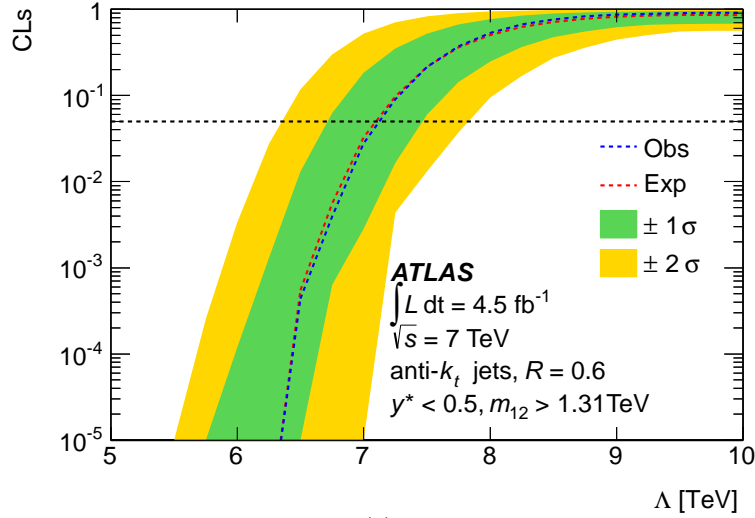


Figure 13. The χ^2 distribution from pseudo-experiments of QCD plus CIs (black histogram) and of the SM background (red histogram) using the full information on the uncertainties, including their asymmetries and correlations, for both the pseudo-experiments (PEs) and the χ^2 calculation. The theoretical hypothesis is the NLO QCD plus CIs prediction based on the CT10 PDF set and a compositeness scale $\Lambda = 6.5$ TeV. The blue (red) dashed vertical line indicates the observed (expected) χ^2 , with the corresponding observed (expected) CLs value given in the legend (see text). The plot corresponds to the measurement in the high dijet-mass subsample for the range $y^* < 0.5$ and jet radius parameter $R = 0.6$.

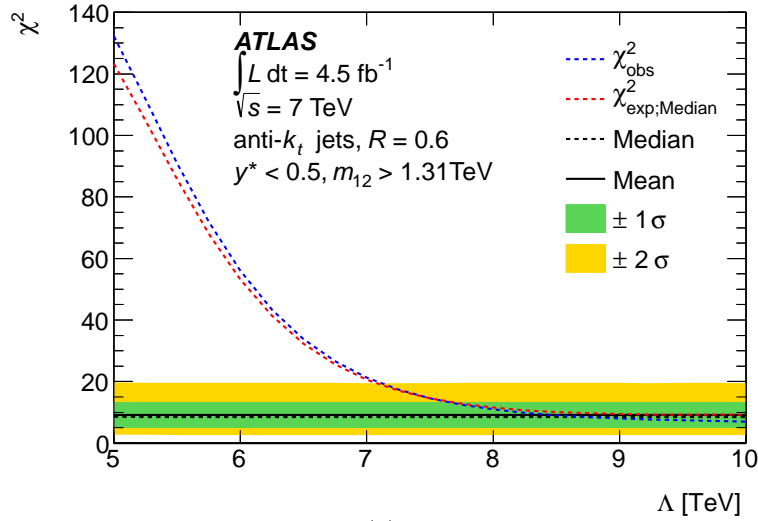
PDF set	Λ [TeV]			
	$R = 0.4$		$R = 0.6$	
	Exp	Obs	Exp	Obs
CT10	7.3	7.2	7.1	7.1
HERAPDF1.5	7.5	7.7	7.3	7.7
MSTW 2008	7.3	7.0	7.1	6.9
NNPDF2.1	7.3	7.2	7.2	7.0

Table 3. Expected and observed lower limits at the 95% CL on the compositeness scale Λ of the NLO QCD plus CIs model using the CT10, HERAPDF1.5, MSTW 2008, and NNPDF2.1 PDF sets, for values of the jet radius parameter $R = 0.4$ and $R = 0.6$, using the measurements in the range $y^* < 0.5$ for the high dijet-mass subsample.

theoretical predictions with jet radius parameter $R = 0.6$, using the CT10 PDF set, and exclude the range $\Lambda < 7.1$ TeV at the 95% CL. The granularity of the scan is 0.25 TeV, and the final value is obtained using a linear interpolation between points. A summary of the lower limits on Λ obtained using the different PDF sets is shown in table 3 for both values of the jet radius parameter. While the expected limits are in the range 7.1–7.5 TeV, the observed ones span the range 6.9–7.7 TeV, the larger values being obtained for the



(a)



(b)

Figure 14. Scan of (a) CL_s value and (b) χ^2 for NLO QCD plus CIs as a function of Λ , using the CT10 PDF set. The green (yellow) bands indicate the $\pm 1\sigma$ ($\pm 2\sigma$) regions, from pseudo-experiments of (a) the SM background and (b) the QCD plus CIs. The full information on uncertainties, including their asymmetries and correlations, is used for both the pseudo-experiments and the χ^2 calculation. The dashed horizontal line in (a) indicates the 95% CL exclusion, computed using the observed (expected) p-value shown by the blue (red) dashed line. In (b) the black dashed (solid) line indicates the median (mean) of the χ^2 distribution of pseudo-experiments. The blue (red) dashed lines indicate the observed (expected) χ^2 . The plots correspond to the measurement with jet radius parameter $R = 0.6$ in the range $y^* < 0.5$, restricted to the high dijet-mass subsample.

HERAPDF1.5 PDF set. When considering the variations of the HERAPDF1.5 PDF's, values of $\Lambda < 7.6\text{--}7.8$ TeV are excluded.

The sensitivity to the assumptions about the correlations between the jet energy cal-

ibration uncertainty components is also tested. An effect at the level of 0.01 TeV on the lower limit for Λ is observed, consistent with the small changes seen for the comparisons with the SM predictions in section 12.

To compare these results with those obtained by previous studies [14] using an approximate (rather than exact) NLO QCD plus CIs calculation, the cross-sections presented here are also used to test the approximate NLO QCD plus CIs prediction. A scaling factor computed from the ratio of the NLO to LO QCD calculations is applied to the sum of the LO QCD plus CIs predictions, together with their interference. This factor ranges between 0.85 and 1.20, depending on the dijet mass and y^* region. Here, for the sake of consistency with previous studies, no electroweak corrections are applied to the QCD or CI contributions. While the cross-sections used here include dijet-mass values $m_{12} > 1.31$ TeV in the range $y^* < 0.5$, the previous results include dijet-mass values $m_{12} > 2.6$ TeV in the range $y^* < 1.7$. Values of $\Lambda < 6.6$ – 7.3 TeV are excluded at the 95% CL using the predictions based on the different PDF sets, with expected lower limits in the range $\Lambda < 6.6$ – 6.9 TeV. This result is comparable to the observed (expected) lower limit of 7.6 TeV (7.7 TeV) obtained by the reconstruction-level analysis using a normalized dijet angular distribution [14], and does not improve the previous result.

14 Summary and conclusions

Cross-section measurements are presented for dijet production in pp collisions at 7 TeV centre-of-mass energy as a function of dijet mass up to 5 TeV, and for half the rapidity separation of $y^* < 3.0$. These measurements are based on the full data sample collected with the ATLAS detector during 2011 at the LHC, corresponding to an integrated luminosity of 4.5 fb^{-1} .

Jets are reconstructed with the anti- k_t algorithm using two values of the radius parameter, $R = 0.4$ and $R = 0.6$, in order to compare data and theory for two different regimes of hadronization, parton shower, underlying event, and higher-order QCD corrections. The measurements are corrected for detector effects to the particle level and compared to theoretical predictions. Fixed-order NLO QCD calculations by NLOJet++, corrected for non-perturbative effects, and POWHEG NLO matrix element calculations interfaced to a parton-shower MC generator are considered. In both cases, corrections to account for electroweak effects are applied.

The statistical uncertainties are smaller than in the previous ATLAS measurement of dijet production using data collected during 2010. In particular, the improved measurement in the high dijet-mass region can be used to constrain the PDF's at high momentum fraction. The correlations between the two measurements, which should be accounted for in a common fit of the PDFs, are non-trivial due to the different treatments of the jet energy calibration uncertainty.

Detailed quantitative comparisons between the measured cross-sections and theoretical predictions are presented, using a frequentist method employing a χ^2 definition generalized for asymmetric uncertainties and their correlations. Good agreement is observed when using the CT10, NNPDF2.1 and MSTW 2008 PDF sets for the theoretical predictions with

values of the jet radius parameter $R = 0.4$ and $R = 0.6$. Disagreement is observed in some ranges of dijet mass and y^* when using the HERAPDF1.5 PDF set, for both values of the jet radius parameter. Even stronger disagreement is observed between data and the NLOJet++ predictions using the ABM11 PDF set, indicating the sensitivity of the measurements to the choice of PDF set. The sensitivity of the frequentist method to assumptions about the correlations between the jet energy calibration uncertainties is tested and found to be small. However, tests of the impact of assumptions about the correlations between the theoretical uncertainties, dominant in the comparison between data and the SM, would be desirable.

The CL_s method is employed using measured cross-sections to explore possible contributions to dijet production from physics beyond the Standard Model. An example using a model of contact interactions is shown, computed using full NLO QCD. An exclusion of compositeness scales $\Lambda < 6.9\text{--}7.7\text{ TeV}$ is achieved, depending on the PDF set used for the calculation. This analysis gives results similar to those from a previous ATLAS analysis using the same data set, that relied on detailed detector simulations of the contact interaction contribution, and does not improve the lower limit on Λ . The method presented here can be used to confront other new models using measurements of dijet production in pp collisions.

Acknowledgments

We thank CERN for the very successful operation of the LHC, as well as the support staff from our institutions without whom ATLAS could not be operated efficiently.

We acknowledge the support of ANPCyT, Argentina; YerPhI, Armenia; ARC, Australia; BMWF and FWF, Austria; ANAS, Azerbaijan; SSTC, Belarus; CNPq and FAPESP, Brazil; NSERC, NRC and CFI, Canada; CERN; CONICYT, Chile; CAS, MOST and NSFC, China; COLCIENCIAS, Colombia; MSMT CR, MPO CR and VSC CR, Czech Republic; DNRF, DNSRC and Lundbeck Foundation, Denmark; EPLANET, ERC and NSRF, European Union; IN2P3-CNRS, CEA-DSM/IRFU, France; GNSF, Georgia; BMBF, DFG, HGF, MPG and AvH Foundation, Germany; GSRT and NSRF, Greece; ISF, MINERVA, GIF, DIP and Benoziyo Center, Israel; INFN, Italy; MEXT and JSPS, Japan; CNRST, Morocco; FOM and NWO, Netherlands; BRF and RCN, Norway; MNiSW and NCN, Poland; GRICES and FCT, Portugal; MNE/IFA, Romania; MES of Russia and ROSATOM, Russian Federation; JINR; MSTD, Serbia; MSSR, Slovakia; ARRS and MIZŠ, Slovenia; DST/NRF, South Africa; MINECO, Spain; SRC and Wallenberg Foundation, Sweden; SER, SNSF and Cantons of Bern and Geneva, Switzerland; NSC, Taiwan; TAEK, Turkey; STFC, the Royal Society and Leverhulme Trust, United Kingdom; DOE and NSF, United States of America.

The crucial computing support from all WLCG partners is acknowledged gratefully, in particular from CERN and the ATLAS Tier-1 facilities at TRIUMF (Canada), NDGF (Denmark, Norway, Sweden), CC-IN2P3 (France), KIT/GridKA (Germany), INFN-CNAF (Italy), NL-T1 (Netherlands), PIC (Spain), ASGC (Taiwan), RAL (UK) and BNL (USA) and in the Tier-2 facilities worldwide.

A Tables of results

$m_{12}-y^*$	m_{12} range	σ	$\delta_{\text{stat}}^{\text{data}}$	$\delta_{\text{stat}}^{\text{MC}}$	$\gamma_{\text{in situ}}$	γ_{pileup}	$\gamma_{\text{close-by}}$	γ_{flavour}	u_{JER}	u_{JAR}	u_{unfold}	u_{qual}	u_{lumi}
bin #	[TeV]	[pb/TeV]	%	%	%	%	%	%	%	%	%	%	%
0	0.26-0.31	7.77e+05	0.47	0.56	+5.6 -5.3	+1.1 -1.0	+1.9 -1.8	+5.0 -4.9	0.9	0.2	0.2		
1	0.31-0.37	2.98e+05	0.45	0.52	+5.5 -5.1	+1.0 -0.9	+1.7 -1.7	+4.7 -4.5	0.8	0.2	0.1		
2	0.37-0.44	1.14e+05	0.41	0.55	+5.4 -5.2	+1.2 -0.9	+1.8 -1.8	+4.3 -4.2	0.8	0.1	0.0		
3	0.44-0.51	4.57e+04	0.43	0.57	+5.3 -5.3	+1.2 -0.9	+1.9 -2.0	+3.9 -3.9	0.8	0.1	0.0		
4	0.51-0.59	1.96e+04	0.30	0.48	+5.2 -5.1	+1.0 -0.9	+2.0 -2.1	+3.5 -3.4	0.8	0.1	0.0		
5	0.59-0.67	8.74e+03	0.30	0.43	+5.0 -4.8	+0.8 -0.7	+2.0 -2.1	+3.1 -3.0	0.7	0.1	0.0		
6	0.67-0.76	4.08e+03	0.23	0.44	+4.9 -4.6	+0.5 -0.5	+1.9 -2.0	+2.8 -2.7	0.6	0.1	0.0		
7	0.76-0.85	1.97e+03	0.27	0.48	+4.8 -4.5	+0.3 -0.3	+1.7 -1.7	+2.5 -2.4	0.5	0.1	0.0		
8	0.85-0.95	9.72e+02	0.25	0.47	+4.7 -4.5	+0.1 -0.1	+1.4 -1.3	+2.3 -2.2	0.5	0.1	0.0		
9	0.95-1.06	4.71e+02	0.31	0.46	+4.9 -4.7	+0.1 -0.0	+0.9 -0.9	+2.0 -2.0	0.4	0.1	0.0		
10	1.06-1.18	2.30e+02	0.42	0.42	+5.2 -5.0	+0.1 -0.1	+0.6 -0.5	+1.9 -1.8	0.4	0.1	0.0	0.5	1.8
11	1.18-1.31	1.12e+02	0.60	0.39	+5.8 -5.6	+0.1 -0.1	+0.3 -0.3	+1.8 -1.7	0.4	0.1	0.0		
12	1.31-1.45	5.22e+01	0.85	0.45	+6.4 -6.2	+0.1 -0.1	+0.1 -0.1	+1.7 -1.6	0.4	0.1	0.0		
13	1.45-1.60	2.53e+01	1.2	0.47	+7.2 -7.0	+0.1 -0.1	+0.1 -0.1	+1.6 -1.6	0.4	0.0	0.0		
14	1.60-1.76	1.22e+01	1.6	0.46	+8.0 -7.9	+0.1 -0.1	+0.0 -0.0	+1.4 -1.5	0.4	0.0	0.0		
15	1.76-1.94	5.93e+00	2.2	0.46	+8.8 -8.7	+0.1 -0.1	+0.0 -0.0	+1.3 -1.4	0.4	0.0	0.0		
16	1.94-2.12	2.58e+00	3.3	0.50	+9.7 -9.6	+0.1 -0.0	+0.0 -0.0	+1.2 -1.2	0.4	0.0	0.0		
17	2.12-2.33	1.22e+00	4.4	0.45	+11 -10	+0.0 -0.0	+0.0 -0.0	+1.1 -1.1	0.4	0.0	0.0		
18	2.33-2.55	5.59e-01	6.5	0.39	+11 -11	+0.0 -0.0	+0.0 -0.0	+1.0 -1.0	0.5	0.0	0.0		
19	2.55-2.78	2.16e-01	10	0.44	+13 -13	+0.0 -0.0	+0.0 -0.0	+1.0 -1.0	0.5	0.0	0.2		
20	2.78-4.27	2.07e-02	14	0.30	+26 -25	+0.0 -0.0	+0.0 -0.0	+0.9 -0.8	1.3	0.0	0.2		

Table 4. Measured double-differential dijet cross-sections for the range $y^* < 0.5$ and jet radius parameter $R = 0.4$. Here, σ is the measured cross-section. All uncertainties are given in %. The variable $\delta_{\text{stat}}^{\text{data}}$ ($\delta_{\text{stat}}^{\text{MC}}$) is the statistical uncertainty from the data (MC simulation). The γ components show the uncertainties due to those on the jet energy calibration from the in situ, pileup, close-by jet, and flavour components. The u components show the uncertainty for the jet energy and angular resolution, the unfolding, the quality selection, and the integrated luminosity. While all columns are uncorrelated with each other, the in situ, pileup, and flavour uncertainties shown here are the sum in quadrature of multiple uncorrelated components. The full set of cross-section values and uncertainty components, each of which is fully correlated in dijet mass and y^* but uncorrelated with the other components, can be found in HepData [16].

$m_{12}-y^*$	m_{12} range	σ	$\delta_{\text{stat}}^{\text{data}}$	$\delta_{\text{stat}}^{\text{MC}}$	$\gamma_{\text{in situ}}$	γ_{pileup}	$\gamma_{\text{close-by}}$	γ_{flavour}	u_{JER}	u_{JAR}	u_{unfold}	u_{qual}	u_{lumi}
bin #	[TeV]	[pb/TeV]	%	%	%	%	%	%	%	%	%	%	%
21	0.31–0.37	6.92e+05	0.52	0.79	+6.4 −5.8	+1.2 −0.9	+2.0 −1.6	+5.4 −5.0	1.4	0.3	0.2		
22	0.37–0.44	2.64e+05	0.54	0.70	+6.3 −6.0	+1.2 −1.1	+2.0 −1.7	+5.0 −4.7	1.0	0.3	0.1		
23	0.44–0.51	1.09e+05	0.55	0.72	+6.2 −6.3	+1.2 −1.1	+1.8 −1.8	+4.5 −4.4	0.7	0.2	0.0		
24	0.51–0.59	4.59e+04	0.53	0.73	+6.0 −6.4	+1.2 −1.1	+1.8 −1.9	+4.0 −4.1	0.6	0.2	0.0		
25	0.59–0.67	2.02e+04	0.54	0.77	+6.0 −6.2	+1.3 −1.2	+1.9 −2.0	+3.6 −3.8	0.7	0.2	0.0		
26	0.67–0.76	9.49e+03	0.41	0.69	+6.1 −6.0	+1.2 −1.2	+2.1 −2.0	+3.4 −3.4	0.7	0.3	0.0		
27	0.76–0.85	4.54e+03	0.40	0.65	+6.1 −5.9	+1.0 −1.1	+2.1 −2.1	+3.2 −3.1	0.6	0.2	0.0		
28	0.85–0.95	2.24e+03	0.35	0.56	+6.0 −5.8	+0.7 −0.7	+1.9 −1.9	+2.9 −2.8	0.5	0.2	0.0		
29	0.95–1.06	1.11e+03	0.33	0.56	+5.8 −5.6	+0.5 −0.4	+1.7 −1.7	+2.6 −2.5	0.5	0.1	0.0		
30	1.06–1.18	5.38e+02	0.36	0.57	+5.7 −5.6	+0.2 −0.1	+1.4 −1.4	+2.4 −2.3	0.6	0.1	0.0		
31	1.18–1.31	2.61e+02	0.40	0.57	+5.8 −5.6	+0.1 −0.1	+1.1 −1.0	+2.2 −2.1	0.6	0.1	0.0	0.5	1.8
32	1.31–1.45	1.26e+02	0.54	0.57	+6.0 −5.8	+0.1 −0.0	+0.7 −0.7	+2.0 −1.9	0.6	0.1	0.0		
33	1.45–1.60	6.01e+01	0.76	0.56	+6.4 −6.1	+0.1 −0.1	+0.4 −0.4	+1.8 −1.7	0.6	0.1	0.0		
34	1.60–1.76	2.86e+01	1.1	0.53	+7.0 −6.7	+0.1 −0.1	+0.2 −0.2	+1.7 −1.6	0.6	0.1	0.0		
35	1.76–1.94	1.33e+01	1.5	0.52	+7.7 −7.4	+0.1 −0.1	+0.1 −0.1	+1.6 −1.5	0.6	0.1	0.0		
36	1.94–2.12	6.05e+00	2.1	0.55	+8.6 −8.2	+0.1 −0.1	+0.1 −0.1	+1.4 −1.4	0.6	0.1	0.0		
37	2.12–2.33	2.68e+00	3.1	0.54	+9.5 −9.1	+0.1 −0.1	+0.0 −0.0	+1.3 −1.3	0.7	0.1	0.0		
38	2.33–2.55	1.03e+00	4.7	0.54	+11 −10	+0.1 −0.1	+0.0 −0.0	+1.2 −1.2	0.8	0.1	0.0		
39	2.55–2.78	4.52e-01	7.0	0.49	+11 −11	+0.1 −0.1	+0.0 −0.0	+1.1 −1.1	0.8	0.1	0.1		
40	2.78–3.04	1.67e-01	11	0.47	+12 −12	+0.0 −0.1	+0.0 −0.0	+1.0 −1.0	0.9	0.1	1.0		
41	3.04–4.27	1.72e-02	16	0.28	+19 −19	+0.0 −0.0	+0.0 −0.0	+0.8 −0.9	1.7	0.0	1.8		

Table 5. Measured double-differential dijet cross-sections for the range $0.5 \leq y^* < 1.0$ and jet radius parameter $R = 0.4$. Here, σ is the measured cross-section. All uncertainties are given in %. The variable $\delta_{\text{stat}}^{\text{data}}$ ($\delta_{\text{stat}}^{\text{MC}}$) is the statistical uncertainty from the data (MC simulation). The γ components show the uncertainties due to those on the jet energy calibration from the in situ, pileup, close-by jet, and flavour components. The u components show the uncertainty for the jet energy and angular resolution, the unfolding, the quality selection, and the integrated luminosity. While all columns are uncorrelated with each other, the in situ, pileup, and flavour uncertainties shown here are the sum in quadrature of multiple uncorrelated components. The full set of cross-section values and uncertainty components, each of which is fully correlated in dijet mass and y^* but uncorrelated with the other components, can be found in HepData [16].

$m_{12}-y^*$	m_{12} range	σ	$\delta_{\text{stat}}^{\text{data}}$	$\delta_{\text{stat}}^{\text{MC}}$	$\gamma_{\text{in situ}}$	γ_{pileup}	$\gamma_{\text{close-by}}$	γ_{flavour}	u_{JER}	u_{JAR}	u_{unfold}	u_{qual}	u_{lumi}
bin #	[TeV]	[pb/TeV]	%	%	%	%	%	%	%	%	%	%	%
42	0.51–0.59	1.31e+05	0.82	0.79	+8.3 –8.5	+1.2 –1.1	+1.6 –1.8	+4.8 –5.0	1.3	0.1	0.3		
43	0.59–0.67	5.92e+04	0.86	0.80	+8.6 –8.6	+1.0 –1.1	+1.6 –1.9	+4.6 –4.6	1.2	0.1	0.1		
44	0.67–0.76	2.73e+04	0.90	0.73	+8.8 –8.7	+1.0 –1.2	+1.7 –1.9	+4.4 –4.3	1.0	0.1	0.0		
45	0.76–0.85	1.28e+04	0.93	0.80	+8.9 –8.7	+0.9 –1.2	+1.9 –2.0	+4.1 –4.0	0.9	0.1	0.0		
46	0.85–0.95	6.60e+03	0.89	0.75	+9.0 –8.7	+0.9 –1.1	+2.0 –2.0	+3.8 –3.6	0.9	0.2	0.0		
47	0.95–1.06	3.18e+03	0.83	0.77	+9.1 –8.6	+0.8 –1.1	+2.0 –1.9	+3.6 –3.3	0.9	0.2	0.0		
48	1.06–1.18	1.53e+03	0.69	0.67	+8.9 –8.5	+0.8 –1.0	+2.1 –2.0	+3.3 –3.0	0.9	0.3	0.0		
49	1.18–1.31	7.43e+02	0.74	0.59	+8.7 –8.5	+0.6 –0.9	+2.1 –2.0	+2.9 –2.8	0.8	0.3	0.0		
50	1.31–1.45	3.54e+02	0.66	0.54	+8.5 –8.4	+0.4 –0.7	+2.0 –1.9	+2.7 –2.6	0.8	0.2	0.0		
51	1.45–1.60	1.72e+02	0.68	0.53	+8.4 –8.3	+0.2 –0.4	+1.8 –1.7	+2.4 –2.4	0.7	0.2	0.0	0.5	1.8
52	1.60–1.76	8.30e+01	0.78	0.53	+8.5 –8.3	+0.1 –0.2	+1.5 –1.4	+2.2 –2.2	0.7	0.1	0.0		
53	1.76–1.94	3.80e+01	0.91	0.51	+8.7 –8.3	+0.0 –0.1	+1.1 –1.1	+2.1 –2.1	0.7	0.1	0.0		
54	1.94–2.12	1.67e+01	1.3	0.55	+9.0 –8.6	+0.0 –0.1	+0.8 –0.8	+2.0 –1.9	0.8	0.1	0.0		
55	2.12–2.33	7.74e+00	1.8	0.52	+9.4 –9.0	+0.1 –0.1	+0.5 –0.5	+1.8 –1.8	0.9	0.1	0.0		
56	2.33–2.55	3.35e+00	2.6	0.44	+10 –9.6	+0.1 –0.1	+0.3 –0.3	+1.7 –1.6	0.9	0.1	0.0		
57	2.55–2.78	1.29e+00	4.0	0.46	+11 –10	+0.1 –0.1	+0.2 –0.2	+1.5 –1.5	1.0	0.1	0.0		
58	2.78–3.04	4.39e-01	6.4	0.45	+12 –11	+0.1 –0.1	+0.1 –0.1	+1.4 –1.4	1.1	0.1	0.1		
59	3.04–3.31	1.72e-01	11	0.42	+13 –12	+0.1 –0.1	+0.1 –0.1	+1.3 –1.3	1.2	0.1	0.9		
60	3.31–4.64	2.11e-02	14	0.28	+19 –18	+0.0 –0.0	+0.0 –0.0	+1.0 –0.9	1.7	0.0	1.5		

Table 6. Measured double-differential dijet cross-sections for the range $1.0 \leq y^* < 1.5$ and jet radius parameter $R = 0.4$. Here, σ is the measured cross-section. All uncertainties are given in %. The variable $\delta_{\text{stat}}^{\text{data}}$ ($\delta_{\text{stat}}^{\text{MC}}$) is the statistical uncertainty from the data (MC simulation). The γ components show the uncertainties due to those on the jet energy calibration from the in situ, pileup, close-by jet, and flavour components. The u components show the uncertainty for the jet energy and angular resolution, the unfolding, the quality selection, and the integrated luminosity. While all columns are uncorrelated with each other, the in situ, pileup, and flavour uncertainties shown here are the sum in quadrature of multiple uncorrelated components. The full set of cross-section values and uncertainty components, each of which is fully correlated in dijet mass and y^* but uncorrelated with the other components, can be found in HepData [16].

$m_{12}-y^*$	m_{12} range	σ	$\delta_{\text{stat}}^{\text{data}}$	$\delta_{\text{stat}}^{\text{MC}}$	$\gamma_{\text{in situ}}$	γ_{pileup}	$\gamma_{\text{close-by}}$	γ_{flavour}	u_{JER}	u_{JAR}	u_{unfold}	u_{qual}	u_{lumi}
bin #	[TeV]	[pb/TeV]	%	%	%	%	%	%	%	%	%	%	%
61	0.76–0.85	3.60e+04	1.4	0.97	+13 -12	+1.4 -1.7	+1.8 -2.1	+4.9 -4.8	1.5	0.3	0.2		
62	0.85–0.95	1.82e+04	1.7	0.99	+13 -12	+1.5 -1.5	+1.8 -2.0	+4.6 -4.6	1.4	0.3	0.1		
63	0.95–1.06	9.01e+03	1.8	0.87	+13 -13	+1.5 -1.3	+1.8 -1.9	+4.4 -4.3	1.4	0.3	0.0		
64	1.06–1.18	4.32e+03	1.9	0.87	+14 -13	+1.4 -1.3	+1.8 -1.8	+4.2 -4.0	1.3	0.3	0.0		
65	1.18–1.31	2.17e+03	2.0	0.78	+14 -13	+1.3 -1.3	+1.9 -1.9	+3.9 -3.7	1.3	0.3	0.0		
66	1.31–1.45	9.98e+02	1.9	0.72	+15 -13	+1.3 -1.4	+2.0 -2.0	+3.7 -3.4	1.3	0.2	0.0		
67	1.45–1.60	4.94e+02	2.2	0.69	+15 -14	+1.3 -1.4	+2.1 -2.1	+3.4 -3.2	1.3	0.2	0.0		
68	1.60–1.76	2.42e+02	1.9	0.65	+15 -14	+1.3 -1.3	+2.2 -2.1	+3.1 -3.0	1.3	0.2	0.0		
69	1.76–1.94	1.11e+02	1.9	0.62	+15 -14	+1.1 -1.1	+2.3 -2.1	+2.9 -2.8	1.3	0.1	0.0	0.5	1.8
70	1.94–2.12	4.99e+01	2.2	0.66	+15 -14	+0.9 -0.9	+2.2 -2.0	+2.8 -2.7	1.4	0.1	0.0		
71	2.12–2.33	2.28e+01	2.0	0.60	+15 -14	+0.7 -0.6	+2.1 -1.9	+2.6 -2.6	1.5	0.1	0.0		
72	2.33–2.55	8.88e+00	2.4	0.65	+16 -14	+0.5 -0.4	+1.9 -1.7	+2.6 -2.5	1.5	0.2	0.0		
73	2.55–2.78	3.64e+00	3.1	0.64	+16 -15	+0.3 -0.2	+1.6 -1.4	+2.5 -2.4	1.6	0.2	0.0		
74	2.78–3.04	1.45e+00	4.1	0.56	+17 -15	+0.1 -0.1	+1.3 -1.1	+2.4 -2.3	1.7	0.2	0.0		
75	3.04–3.31	5.47e-01	6.0	0.51	+18 -16	+0.1 -0.1	+1.0 -0.9	+2.3 -2.2	1.9	0.2	0.1		
76	3.31–3.61	1.64e-01	10	0.59	+19 -16	+0.1 -0.1	+0.8 -0.7	+2.2 -2.2	2.1	0.2	0.5		
77	3.61–4.64	1.42e-02	20	0.51	+24 -21	+0.1 -0.1	+0.0 -0.0	+1.7 -1.9	3.1	0.1	1.4		

Table 7. Measured double-differential dijet cross-sections for the range $1.5 \leq y^* < 2.0$ and jet radius parameter $R = 0.4$. Here, σ is the measured cross-section. All uncertainties are given in %. The variable $\delta_{\text{stat}}^{\text{data}}$ ($\delta_{\text{stat}}^{\text{MC}}$) is the statistical uncertainty from the data (MC simulation). The γ components show the uncertainties due to those on the jet energy calibration from the in situ, pileup, close-by jet, and flavour components. The u components show the uncertainty for the jet energy and angular resolution, the unfolding, the quality selection, and the integrated luminosity. While all columns are uncorrelated with each other, the in situ, pileup, and flavour uncertainties shown here are the sum in quadrature of multiple uncorrelated components. The full set of cross-section values and uncertainty components, each of which is fully correlated in dijet mass and y^* but uncorrelated with the other components, can be found in HepData [16].

$m_{12}-y^*$	m_{12} range	σ	$\delta_{\text{stat}}^{\text{data}}$	$\delta_{\text{stat}}^{\text{MC}}$	$\gamma_{\text{in situ}}$	γ_{pileup}	$\gamma_{\text{close-by}}$	γ_{flavour}	u_{JER}	u_{JAR}	u_{unfold}	u_{qual}	u_{lumi}
bin #	[TeV]	[pb/TeV]	%	%	%	%	%	%	%	%	%	%	%
78	1.31–1.45	2.48e+03	3.9	1.1	+21 –18	+1.8 –1.9	+1.9 –1.8	+4.2 –3.8	2.2	0.5	0.1	0.5	1.8
79	1.45–1.60	1.29e+03	4.6	1.2	+21 –19	+1.7 –1.9	+1.8 –1.8	+3.9 –3.6	2.0	0.6	0.1		
80	1.60–1.76	6.61e+02	4.8	1.0	+21 –19	+1.7 –1.8	+1.8 –1.8	+3.6 –3.3	1.9	0.5	0.1		
81	1.76–2.12	2.05e+02	4.5	0.69	+22 –20	+1.8 –1.7	+1.9 –1.9	+3.2 –3.0	1.8	0.4	0.0		
82	2.12–2.55	4.03e+01	5.8	0.65	+25 –22	+2.1 –1.9	+2.2 –2.0	+2.9 –2.6	1.9	0.2	0.1		
83	2.55–3.04	6.83e+00	6.8	0.53	+28 –24	+2.2 –2.1	+2.4 –2.3	+2.7 –2.5	2.4	0.4	0.1		
84	3.04–3.61	8.77e-01	10	0.65	+31 –25	+2.1 –1.8	+2.5 –2.3	+2.6 –2.5	3.2	0.7	0.0		
85	3.61–5.04	3.31e-02	18	1.2	+42 –31	+0.9 –0.9	+2.1 –1.1	+2.5 –2.9	6.2	0.9	2.3		

Table 8. Measured double-differential dijet cross-sections for the range $2.0 \leq y^* < 2.5$ and jet radius parameter $R = 0.4$. Here, σ is the measured cross-section. All uncertainties are given in %. The variable $\delta_{\text{stat}}^{\text{data}}$ ($\delta_{\text{stat}}^{\text{MC}}$) is the statistical uncertainty from the data (MC simulation). The γ components show the uncertainties due to those on the jet energy calibration from the in situ, pileup, close-by jet, and flavour components. The u components show the uncertainty for the jet energy and angular resolution, the unfolding, the quality selection, and the integrated luminosity. While all columns are uncorrelated with each other, the in situ, pileup, and flavour uncertainties shown here are the sum in quadrature of multiple uncorrelated components. The full set of cross-section values and uncertainty components, each of which is fully correlated in dijet mass and y^* but uncorrelated with the other components, can be found in HepData [16].

$m_{12}-y^*$	m_{12} range	σ	$\delta_{\text{stat}}^{\text{data}}$	$\delta_{\text{stat}}^{\text{MC}}$	$\gamma_{\text{in situ}}$	γ_{pileup}	$\gamma_{\text{close-by}}$	γ_{flavour}	u_{JER}	u_{JAR}	u_{unfold}	u_{qual}	u_{lumi}
bin #	[TeV]	[pb/TeV]	%	%	%	%	%	%	%	%	%	%	%
86	2.12–2.55	5.73e+01	16	1.2	+32 –26	+2.1 –1.8	+1.8 –1.3	+3.0 –2.5	2.8	0.3	0.2	0.5	1.8
87	2.55–3.04	1.28e+01	20	1.3	+37 –29	+2.9 –2.2	+2.1 –1.8	+2.8 –2.0	3.5	0.3	0.1		
88	3.04–3.93	1.06e+00	28	1.4	+46 –34	+4.5 –3.0	+2.8 –2.5	+2.4 –1.9	5.0	0.2	0.4		
89	3.93–5.04	1.90e-02	70	2.1	+73 –48	+7.0 –5.1	+4.2 –3.1	+2.3 –2.4	10	0.5	1.7		

Table 9. Measured double-differential dijet cross-sections for the range $2.5 \leq y^* < 3.0$ and jet radius parameter $R = 0.4$. Here, σ is the measured cross-section. All uncertainties are given in %. The variable $\delta_{\text{stat}}^{\text{data}}$ ($\delta_{\text{stat}}^{\text{MC}}$) is the statistical uncertainty from the data (MC simulation). The γ components show the uncertainties due to those on the jet energy calibration from the in situ, pileup, close-by jet, and flavour components. The u components show the uncertainty for the jet energy and angular resolution, the unfolding, the quality selection, and the integrated luminosity. While all columns are uncorrelated with each other, the in situ, pileup, and flavour uncertainties shown here are the sum in quadrature of multiple uncorrelated components. The full set of cross-section values and uncertainty components, each of which is fully correlated in dijet mass and y^* but uncorrelated with the other components, can be found in HepData [16].

$m_{12}-y^*$	m_{12} range	σ	$\delta_{\text{stat}}^{\text{data}}$	$\delta_{\text{stat}}^{\text{MC}}$	$\gamma_{\text{in situ}}$	γ_{pileup}	$\gamma_{\text{close-by}}$	γ_{flavour}	u_{JER}	u_{JAR}	u_{unfold}	u_{qual}	u_{lumi}
bin #	[TeV]	[pb/TeV]	%	%	%	%	%	%	%	%	%	%	%
0	0.26–0.31	1.07e+06	0.55	0.61	+5.6 –5.3	+1.6 –1.3	+2.9 –2.3	+5.5 –5.1	2.0	0.2	0.3		
1	0.31–0.37	4.06e+05	0.60	0.52	+5.4 –5.1	+1.3 –1.1	+2.4 –2.0	+5.1 –4.8	1.5	0.2	0.1		
2	0.37–0.44	1.52e+05	0.57	0.55	+5.2 –4.9	+1.1 –1.1	+2.0 –1.9	+4.5 –4.3	1.0	0.2	0.1		
3	0.44–0.51	6.06e+04	0.57	0.58	+5.1 –4.8	+1.1 –1.1	+1.8 –1.9	+4.0 –3.8	0.8	0.2	0.0		
4	0.51–0.59	2.57e+04	0.58	0.51	+4.9 –4.8	+1.1 –1.1	+1.8 –1.9	+3.5 –3.4	0.7	0.2	0.0		
5	0.59–0.67	1.13e+04	0.42	0.44	+4.8 –4.7	+1.0 –1.2	+1.8 –1.8	+3.1 –3.0	0.7	0.2	0.0		
6	0.67–0.76	5.21e+03	0.46	0.43	+4.8 –4.7	+0.9 –1.2	+1.6 –1.6	+2.8 –2.7	0.7	0.2	0.0		
7	0.76–0.85	2.51e+03	0.36	0.47	+4.8 –4.6	+0.7 –1.0	+1.3 –1.3	+2.5 –2.4	0.5	0.2	0.0		
8	0.85–0.95	1.24e+03	0.36	0.45	+4.8 –4.6	+0.5 –0.7	+0.9 –1.0	+2.2 –2.1	0.4	0.1	0.0		
9	0.95–1.06	5.99e+02	0.37	0.45	+5.0 –4.8	+0.3 –0.4	+0.6 –0.7	+1.9 –1.8	0.3	0.1	0.0		
10	1.06–1.18	2.90e+02	0.38	0.43	+5.2 –5.1	+0.1 –0.2	+0.4 –0.4	+1.7 –1.6	0.3	0.1	0.0	0.5	1.8
11	1.18–1.31	1.40e+02	0.52	0.38	+5.7 –5.6	+0.1 –0.1	+0.2 –0.2	+1.4 –1.4	0.3	0.1	0.0		
12	1.31–1.45	6.56e+01	0.74	0.41	+6.4 –6.3	+0.1 –0.1	+0.1 –0.1	+1.3 –1.3	0.3	0.1	0.0		
13	1.45–1.60	3.19e+01	1.0	0.43	+7.2 –7.2	+0.1 –0.1	+0.0 –0.0	+1.2 –1.2	0.4	0.1	0.0		
14	1.60–1.76	1.49e+01	1.4	0.45	+8.1 –8.1	+0.1 –0.1	+0.0 –0.0	+1.1 –1.1	0.3	0.1	0.0		
15	1.76–1.94	7.05e+00	2.0	0.46	+9.1 –9.0	+0.1 –0.1	+0.0 –0.0	+1.0 –1.0	0.3	0.1	0.0		
16	1.94–2.12	3.23e+00	3.0	0.52	+10 –9.9	+0.1 –0.1	+0.0 –0.0	+1.0 –1.0	0.4	0.1	0.0		
17	2.12–2.33	1.44e+00	4.1	0.47	+11 –11	+0.1 –0.1	+0.0 –0.0	+0.9 –0.9	0.4	0.1	0.0		
18	2.33–2.55	6.81e-01	5.8	0.39	+12 –11	+0.1 –0.1	+0.0 –0.0	+0.9 –0.9	0.4	0.0	0.0		
19	2.55–2.78	2.79e-01	9.0	0.40	+13 –13	+0.1 –0.1	+0.0 –0.0	+0.9 –0.8	0.5	0.0	0.0		
20	2.78–4.27	2.52e-02	12	0.29	+26 –25	+0.0 –0.0	+0.0 –0.0	+0.7 –0.7	0.8	0.0	0.0		

Table 10. Measured double-differential dijet cross-sections for the range $y^* < 0.5$ and jet radius parameter $R = 0.6$. Here, σ is the measured cross-section. All uncertainties are given in %. The variable $\delta_{\text{stat}}^{\text{data}}$ ($\delta_{\text{stat}}^{\text{MC}}$) is the statistical uncertainty from the data (MC simulation). The γ components show the uncertainties due to those on the jet energy calibration from the in situ, pileup, close-by jet, and flavour components. The u components show the uncertainty for the jet energy and angular resolution, the unfolding, the quality selection, and the integrated luminosity. While all columns are uncorrelated with each other, the in situ, pileup, and flavour uncertainties shown here are the sum in quadrature of multiple uncorrelated components. The full set of cross-section values and uncertainty components, each of which is fully correlated in dijet mass and y^* but uncorrelated with the other components, can be found in HepData [16].

$m_{12}-y^*$	m_{12} range	σ	$\delta_{\text{stat}}^{\text{data}}$	$\delta_{\text{stat}}^{\text{MC}}$	$\gamma_{\text{in situ}}$	γ_{pileup}	$\gamma_{\text{close-by}}$	γ_{flavour}	u_{JER}	u_{JAR}	u_{unfold}	u_{qual}	u_{lumi}
bin #	[TeV]	[pb/TeV]	%	%	%	%	%	%	%	%	%	%	%
21	0.31–0.37	9.61e+05	0.66	0.86	+6.4 –5.9	+1.4 –1.3	+2.6 –2.4	+5.8 –5.2	2.5	0.3	0.4		
22	0.37–0.44	3.68e+05	0.66	0.76	+6.4 –6.0	+1.2 –1.4	+2.5 –2.1	+5.5 –4.9	1.8	0.4	0.2		
23	0.44–0.51	1.46e+05	0.71	0.70	+6.2 –6.1	+1.1 –1.4	+2.3 –2.0	+5.0 –4.6	1.2	0.3	0.0		
24	0.51–0.59	6.03e+04	0.74	0.76	+6.1 –6.1	+1.1 –1.4	+2.2 –2.0	+4.5 –4.3	1.0	0.2	0.0		
25	0.59–0.67	2.73e+04	0.74	0.77	+6.2 –5.9	+1.3 –1.4	+2.2 –2.0	+4.1 –3.8	0.9	0.2	0.0		
26	0.67–0.76	1.24e+04	0.74	0.72	+6.1 –5.6	+1.4 –1.2	+2.2 –2.0	+3.7 –3.3	0.9	0.2	0.0		
27	0.76–0.85	5.96e+03	0.67	0.67	+5.8 –5.4	+1.4 –1.1	+2.1 –1.9	+3.3 –3.0	0.9	0.2	0.0		
28	0.85–0.95	2.94e+03	0.57	0.57	+5.6 –5.3	+1.2 –0.9	+1.9 –1.7	+2.9 –2.7	0.9	0.2	0.0		
29	0.95–1.06	1.41e+03	0.58	0.56	+5.5 –5.3	+0.9 –0.7	+1.5 –1.4	+2.5 –2.5	0.8	0.1	0.0		
30	1.06–1.18	6.83e+02	0.49	0.55	+5.4 –5.4	+0.5 –0.5	+1.1 –1.1	+2.2 –2.2	0.7	0.1	0.0		
31	1.18–1.31	3.36e+02	0.51	0.56	+5.5 –5.5	+0.3 –0.3	+0.8 –0.8	+1.9 –2.0	0.7	0.1	0.0	0.5	1.8
32	1.31–1.45	1.59e+02	0.56	0.57	+5.8 –5.7	+0.1 –0.2	+0.5 –0.5	+1.7 –1.7	0.7	0.1	0.0		
33	1.45–1.60	7.64e+01	0.67	0.54	+6.2 –6.0	+0.0 –0.1	+0.3 –0.3	+1.5 –1.5	0.7	0.1	0.0		
34	1.60–1.76	3.64e+01	0.92	0.51	+6.9 –6.6	+0.1 –0.1	+0.2 –0.2	+1.4 –1.3	0.7	0.1	0.0		
35	1.76–1.94	1.67e+01	1.3	0.51	+7.7 –7.3	+0.1 –0.1	+0.1 –0.1	+1.2 –1.1	0.8	0.1	0.0		
36	1.94–2.12	7.57e+00	1.9	0.54	+8.8 –8.2	+0.1 –0.1	+0.0 –0.0	+1.1 –1.0	0.8	0.1	0.0		
37	2.12–2.33	3.36e+00	2.7	0.51	+9.8 –9.3	+0.1 –0.1	+0.0 –0.0	+1.0 –1.0	0.8	0.1	0.0		
38	2.33–2.55	1.29e+00	4.1	0.53	+11 –10	+0.1 –0.1	+0.0 –0.0	+1.0 –0.9	0.8	0.0	0.0		
39	2.55–2.78	5.44e-01	6.4	0.49	+12 –11	+0.1 –0.1	+0.0 –0.0	+1.0 –0.9	0.9	0.0	0.1		
40	2.78–3.04	1.80e-01	10	0.44	+13 –12	+0.1 –0.1	+0.0 –0.0	+1.0 –1.0	0.9	0.0	0.6		
41	3.04–4.27	2.11e-02	15	0.27	+20 –19	+0.1 –0.1	+0.0 –0.0	+1.3 –1.1	1.9	0.0	1.1		

Table 11. Measured double-differential dijet cross-sections for the range $0.5 \leq y^* < 1.0$ and jet radius parameter $R = 0.6$. Here, σ is the measured cross-section. All uncertainties are given in %. The variable $\delta_{\text{stat}}^{\text{data}}$ ($\delta_{\text{stat}}^{\text{MC}}$) is the statistical uncertainty from the data (MC simulation). The γ components show the uncertainties due to those on the jet energy calibration from the in situ, pileup, close-by jet, and flavour components. The u components show the uncertainty for the jet energy and angular resolution, the unfolding, the quality selection, and the integrated luminosity. While all columns are uncorrelated with each other, the in situ, pileup, and flavour uncertainties shown here are the sum in quadrature of multiple uncorrelated components. The full set of cross-section values and uncertainty components, each of which is fully correlated in dijet mass and y^* but uncorrelated with the other components, can be found in HepData [16].

$m_{12}-y^*$	m_{12} range	σ	$\delta_{\text{stat}}^{\text{data}}$	$\delta_{\text{stat}}^{\text{MC}}$	$\gamma_{\text{in situ}}$	γ_{pileup}	$\gamma_{\text{close-by}}$	γ_{flavour}	u_{JER}	u_{JAR}	u_{unfold}	u_{qual}	u_{lumi}
bin #	[TeV]	[pb/TeV]	%	%	%	%	%	%	%	%	%	%	%
42	0.51–0.59	1.80e+05	1.0	0.84	+8.0 –8.1	+1.5 –1.8	+2.6 –2.6	+5.3 –5.2	2.3	0.2	0.4		
43	0.59–0.67	8.07e+04	1.1	0.86	+8.3 –8.2	+1.5 –1.6	+2.4 –2.3	+5.0 –5.0	2.0	0.2	0.2		
44	0.67–0.76	3.74e+04	1.2	0.76	+8.5 –8.2	+1.5 –1.4	+2.3 –2.1	+4.7 –4.6	1.8	0.2	0.0		
45	0.76–0.85	1.75e+04	1.2	0.81	+8.5 –8.1	+1.4 –1.3	+2.2 –2.0	+4.4 –4.1	1.6	0.3	0.0		
46	0.85–0.95	8.84e+03	1.3	0.76	+8.4 –8.0	+1.3 –1.3	+2.0 –2.0	+4.0 –3.8	1.4	0.2	0.0		
47	0.95–1.06	4.21e+03	1.2	0.77	+8.4 –7.9	+1.3 –1.3	+2.0 –2.0	+3.7 –3.5	1.4	0.2	0.0		
48	1.06–1.18	2.08e+03	1.3	0.72	+8.3 –7.8	+1.3 –1.3	+2.0 –1.9	+3.4 –3.2	1.5	0.2	0.0		
49	1.18–1.31	9.64e+02	1.2	0.62	+8.1 –7.6	+1.4 –1.3	+1.9 –1.9	+3.1 –2.9	1.5	0.1	0.0		
50	1.31–1.45	4.66e+02	1.1	0.53	+7.9 –7.5	+1.3 –1.3	+1.8 –1.7	+2.7 –2.7	1.5	0.1	0.0		
51	1.45–1.60	2.26e+02	1.2	0.51	+7.7 –7.5	+1.1 –1.0	+1.6 –1.4	+2.4 –2.4	1.5	0.1	0.0	0.5	1.8
52	1.60–1.76	1.07e+02	1.0	0.52	+7.7 –7.5	+0.8 –0.7	+1.2 –1.1	+2.2 –2.2	1.4	0.1	0.0		
53	1.76–1.94	4.91e+01	1.1	0.50	+7.7 –7.6	+0.5 –0.4	+0.9 –0.8	+1.9 –1.9	1.3	0.1	0.0		
54	1.94–2.12	2.21e+01	1.5	0.56	+8.0 –7.8	+0.3 –0.2	+0.6 –0.6	+1.7 –1.7	1.3	0.1	0.0		
55	2.12–2.33	9.86e+00	1.6	0.49	+8.6 –8.3	+0.1 –0.0	+0.4 –0.4	+1.6 –1.6	1.4	0.1	0.0		
56	2.33–2.55	4.30e+00	2.3	0.45	+9.4 –8.9	+0.1 –0.0	+0.2 –0.2	+1.5 –1.4	1.5	0.1	0.0		
57	2.55–2.78	1.73e+00	3.6	0.47	+10 –9.7	+0.1 –0.1	+0.1 –0.1	+1.4 –1.4	1.7	0.1	0.0		
58	2.78–3.04	6.16e-01	5.7	0.45	+11 –11	+0.1 –0.1	+0.1 –0.1	+1.3 –1.3	1.8	0.1	0.1		
59	3.04–3.31	1.88e-01	9.7	0.42	+12 –12	+0.2 –0.1	+0.0 –0.0	+1.3 –1.3	1.9	0.1	0.9		
60	3.31–4.64	2.61e-02	13	0.25	+19 –18	+0.2 –0.1	+0.0 –0.0	+1.4 –1.3	3.4	0.0	1.7		

Table 12. Measured double-differential dijet cross-sections for the range $1.0 \leq y^* < 1.5$ and jet radius parameter $R = 0.6$. Here, σ is the measured cross-section. All uncertainties are given in %. The variable $\delta_{\text{stat}}^{\text{data}}$ ($\delta_{\text{stat}}^{\text{MC}}$) is the statistical uncertainty from the data (MC simulation). The γ components show the uncertainties due to those on the jet energy calibration from the in situ, pileup, close-by jet, and flavour components. The u components show the uncertainty for the jet energy and angular resolution, the unfolding, the quality selection, and the integrated luminosity. While all columns are uncorrelated with each other, the in situ, pileup, and flavour uncertainties shown here are the sum in quadrature of multiple uncorrelated components. The full set of cross-section values and uncertainty components, each of which is fully correlated in dijet mass and y^* but uncorrelated with the other components, can be found in HepData [16].

$m_{12}-y^*$	m_{12} range	σ	$\delta_{\text{stat}}^{\text{data}}$	$\delta_{\text{stat}}^{\text{MC}}$	$\gamma_{\text{in situ}}$	γ_{pileup}	$\gamma_{\text{close-by}}$	γ_{flavour}	u_{JER}	u_{JAR}	u_{unfold}	u_{qual}	u_{lumi}
bin #	[TeV]	[pb/TeV]	%	%	%	%	%	%	%	%	%	%	%
61	0.76–0.85	4.96e+04	1.8	0.93	+12 -11	+1.4 -1.4	+2.9 -2.6	+5.1 -4.9	3.8	0.4	0.2		
62	0.85–0.95	2.55e+04	2.1	0.99	+12 -11	+1.4 -1.4	+2.6 -2.5	+5.0 -4.7	3.4	0.4	0.1		
63	0.95–1.06	1.22e+04	2.1	0.93	+12 -12	+1.6 -1.5	+2.4 -2.4	+4.7 -4.5	3.0	0.3	0.0		
64	1.06–1.18	6.14e+03	2.4	0.87	+13 -12	+1.7 -1.5	+2.3 -2.2	+4.4 -4.3	2.7	0.3	0.0		
65	1.18–1.31	2.82e+03	2.5	0.85	+13 -12	+1.8 -1.5	+2.4 -2.1	+4.1 -4.0	2.5	0.2	0.0		
66	1.31–1.45	1.44e+03	2.8	0.74	+13 -12	+1.9 -1.5	+2.4 -2.1	+3.9 -3.7	2.4	0.2	0.0		
67	1.45–1.60	6.87e+02	3.0	0.66	+13 -12	+1.9 -1.5	+2.4 -2.1	+3.7 -3.5	2.3	0.2	0.0		
68	1.60–1.76	3.41e+02	3.1	0.66	+13 -12	+1.8 -1.7	+2.2 -2.2	+3.4 -3.3	2.2	0.2	0.0		
69	1.76–1.94	1.50e+02	3.6	0.68	+13 -12	+1.7 -1.7	+2.0 -2.2	+3.2 -3.1	2.2	0.2	0.0	0.5	1.8
70	1.94–2.12	6.33e+01	2.9	0.64	+13 -12	+1.5 -1.7	+1.8 -2.0	+2.9 -2.9	2.4	0.2	0.0		
71	2.12–2.33	3.04e+01	3.4	0.56	+13 -12	+1.4 -1.6	+1.5 -1.8	+2.7 -2.7	2.6	0.2	0.0		
72	2.33–2.55	1.21e+01	4.3	0.64	+14 -12	+1.2 -1.3	+1.3 -1.6	+2.6 -2.6	2.8	0.2	0.0		
73	2.55–2.78	4.90e+00	4.0	0.64	+14 -13	+1.0 -1.1	+1.1 -1.3	+2.4 -2.5	3.0	0.2	0.0		
74	2.78–3.04	1.82e+00	4.8	0.48	+14 -13	+0.8 -0.8	+0.9 -1.0	+2.3 -2.4	3.4	0.2	0.0		
75	3.04–3.31	7.06e-01	7.1	0.50	+15 -14	+0.5 -0.5	+0.7 -0.8	+2.3 -2.3	3.8	0.2	0.1		
76	3.31–3.61	2.44e-01	9.7	0.53	+16 -14	+0.3 -0.3	+0.6 -0.6	+2.2 -2.2	4.2	0.2	0.4		
77	3.61–4.64	2.15e-02	16	0.49	+21 -19	+0.2 -0.3	+0.0 -0.0	+2.0 -2.0	6.1	0.1	1.2		

Table 13. Measured double-differential dijet cross-sections for the range $1.5 \leq y^* < 2.0$ and jet radius parameter $R = 0.6$. Here, σ is the measured cross-section. All uncertainties are given in %. The variable $\delta_{\text{stat}}^{\text{data}}$ ($\delta_{\text{stat}}^{\text{MC}}$) is the statistical uncertainty from the data (MC simulation). The γ components show the uncertainties due to those on the jet energy calibration from the in situ, pileup, close-by jet, and flavour components. The u components show the uncertainty for the jet energy and angular resolution, the unfolding, the quality selection, and the integrated luminosity. While all columns are uncorrelated with each other, the in situ, pileup, and flavour uncertainties shown here are the sum in quadrature of multiple uncorrelated components. The full set of cross-section values and uncertainty components, each of which is fully correlated in dijet mass and y^* but uncorrelated with the other components, can be found in HepData [16].

$m_{12}-y^*$	m_{12} range	σ	$\delta_{\text{stat}}^{\text{data}}$	$\delta_{\text{stat}}^{\text{MC}}$	$\gamma_{\text{in situ}}$	γ_{pileup}	$\gamma_{\text{close-by}}$	γ_{flavour}	u_{JER}	u_{JAR}	u_{unfold}	u_{qual}	u_{lumi}
bin #	[TeV]	[pb/TeV]	%	%	%	%	%	%	%	%	%	%	%
78	1.31–1.45	3.39e+03	4.4	1.1	+18 −17	+2.6 −2.2	+2.8 −2.8	+4.1 −4.1	5.1	0.6	0.1	0.5	1.8
79	1.45–1.60	1.78e+03	5.1	1.1	+19 −17	+2.5 −2.0	+2.6 −2.7	+3.9 −3.9	4.8	0.6	0.1		
80	1.60–1.76	8.32e+02	6.2	1.3	+19 −17	+2.4 −1.9	+2.5 −2.6	+3.8 −3.7	4.4	0.6	0.1		
81	1.76–2.12	2.93e+02	6.4	0.81	+20 −17	+2.3 −1.8	+2.5 −2.4	+3.7 −3.4	4.0	0.5	0.0		
82	2.12–2.55	5.75e+01	8.8	0.72	+22 −19	+2.5 −2.1	+2.5 −2.4	+3.5 −3.2	4.0	0.3	0.0		
83	2.55–3.04	9.59e+00	12	0.48	+24 −20	+2.8 −2.3	+2.5 −2.3	+3.3 −3.1	4.9	0.3	0.0		
84	3.04–3.61	1.34e+00	12	0.62	+26 −22	+3.0 −2.5	+2.2 −2.3	+3.2 −3.1	6.1	0.4	0.1		
85	3.61–5.04	4.50e-02	29	1.2	+34 −28	+4.3 −3.3	+0.6 −0.6	+3.2 −3.2	9.5	0.4	1.6		

Table 14. Measured double-differential dijet cross-sections for the range $2.0 \leq y^* < 2.5$ and jet radius parameter $R = 0.6$. Here, σ is the measured cross-section. All uncertainties are given in %. The variable $\delta_{\text{stat}}^{\text{data}}$ ($\delta_{\text{stat}}^{\text{MC}}$) is the statistical uncertainty from the data (MC simulation). The γ components show the uncertainties due to those on the jet energy calibration from the in situ, pileup, close-by jet, and flavour components. The u components show the uncertainty for the jet energy and angular resolution, the unfolding, the quality selection, and the integrated luminosity. While all columns are uncorrelated with each other, the in situ, pileup, and flavour uncertainties shown here are the sum in quadrature of multiple uncorrelated components. The full set of cross-section values and uncertainty components, each of which is fully correlated in dijet mass and y^* but uncorrelated with the other components, can be found in HepData [16].

$m_{12}-y^*$	m_{12} range	σ	$\delta_{\text{stat}}^{\text{data}}$	$\delta_{\text{stat}}^{\text{MC}}$	$\gamma_{\text{in situ}}$	γ_{pileup}	$\gamma_{\text{close-by}}$	γ_{flavour}	u_{JER}	u_{JAR}	u_{unfold}	u_{qual}	u_{lumi}
bin #	[TeV]	[pb/TeV]	%	%	%	%	%	%	%	%	%	%	%
86	2.12–2.55	1.09e+02	18	1.1	+27 −22	+3.1 −2.5	+2.5 −2.1	+2.9 −2.9	5.2	1.2	0.3	0.5	1.8
87	2.55–3.04	9.75e+00	26	1.8	+30 −24	+3.1 −2.2	+2.5 −2.0	+2.9 −2.7	4.8	1.0	0.1		
88	3.04–3.93	2.42e+00	36	1.1	+38 −29	+3.3 −2.3	+2.6 −2.6	+2.8 −2.6	5.9	1.0	0.1		
89	3.93–5.04	2.10e-02	76	2.4	+61 −43	+5.3 −4.5	+2.9 −3.1	+3.1 −3.2	4.2	2.4	0.4		

Table 15. Measured double-differential dijet cross-sections for the range $2.5 \leq y^* < 3.0$ and jet radius parameter $R = 0.6$. Here, σ is the measured cross-section. All uncertainties are given in %. The variable $\delta_{\text{stat}}^{\text{data}}$ ($\delta_{\text{stat}}^{\text{MC}}$) is the statistical uncertainty from the data (MC simulation). The γ components show the uncertainties due to those on the jet energy calibration from the in situ, pileup, close-by jet, and flavour components. The u components show the uncertainty for the jet energy and angular resolution, the unfolding, the quality selection, and the integrated luminosity. While all columns are uncorrelated with each other, the in situ, pileup, and flavour uncertainties shown here are the sum in quadrature of multiple uncorrelated components. The full set of cross-section values and uncertainty components, each of which is fully correlated in dijet mass and y^* but uncorrelated with the other components, can be found in HepData [16].

References

- [1] L. Evans and P. Bryant, *LHC Machine*, *JINST* **3** (2008) S08001.
- [2] CDF Collaboration, T. Aaltonen et al., *Search for new particles decaying into dijets in proton-antiproton collisions at $\sqrt{s} = 1.96$ TeV*, *Phys. Rev. D* **79** (2009) 112002, [arXiv:0812.4036 \[hep-ex\]](#).
- [3] D0 Collaboration, V. Abazov et al., *Measurement of the dijet invariant mass cross section in $p\bar{p}$ collisions at $\sqrt{s} = 1.96$ TeV*, *Phys. Lett. B* **693** (2010) 531–538, [arXiv:1002.4594 \[hep-ex\]](#).
- [4] CMS Collaboration, *Measurement of the differential dijet production cross section in proton-proton collisions at $\sqrt{s} = 7$ TeV*, *Phys. Lett. B* **700** (2011) 187–206, [arXiv:1104.1693 \[hep-ex\]](#).
- [5] ATLAS Collaboration, *Measurement of inclusive jet and dijet production in pp collisions at $\sqrt{s} = 7$ TeV using the ATLAS detector*, *Phys. Rev. D* **86** (2012) 014022, [arXiv:1112.6297 \[hep-ex\]](#).
- [6] CMS Collaboration, *Measurements of differential jet cross sections in proton-proton collisions at $\sqrt{s} = 7$ TeV with the CMS detector*, *Phys. Rev. D* **87** (2013) 112002, [arXiv:1212.6660 \[hep-ex\]](#).
- [7] H.-L. Lai et al., *New parton distributions for collider physics*, *Phys. Rev. D* **82** (2010) 074024, [arXiv:1007.2241 \[hep-ph\]](#).
- [8] B. Malaescu, *An Iterative, Dynamically Stabilized (IDS) Method of Data Unfolding*, [arXiv:1106.3107 \[physics.data-an\]](#).
- [9] ATLAS Collaboration, *Jet energy scale and its systematic uncertainty in proton-proton collisions at $\sqrt{s} = 7$ TeV with ATLAS 2011 data*, ATLAS-CONF-2013-004. <http://cds.cern.ch/record/1509552>.
- [10] Z. Nagy, *Next-to-leading order calculation of three jet observables in hadron hadron collision*, *Phys. Rev. D* **68** (2003) 094002, [arXiv:hep-ph/0307268](#).
- [11] P. Nason, *A new method for combining NLO QCD with shower Monte Carlo algorithms*, *JHEP* **11** (2004) 040, [arXiv:hep-ph/0409146](#).
- [12] U. Baur, I. Hinchliffe, and D. Zeppenfeld, *Excited Quark Production at Hadron Colliders*, *Int. J. Mod. Phys. A* **2** (1987) 1285.
- [13] E. Eichten, K. Lane, and M. Peskin, *New Tests for Quark and Lepton Substructure*, *Phys. Rev. Lett.* **50** (1983) 811–814.
- [14] ATLAS Collaboration, *ATLAS search for new phenomena in dijet mass and angular distributions using pp collisions at $\sqrt{s} = 7$ TeV*, *JHEP* **01** (2013) 029, [arXiv:1210.1718 \[hep-ex\]](#).
- [15] CMS Collaboration, *Search for quark compositeness in dijet angular distributions from pp collisions at $\sqrt{s} = 7$ TeV*, *JHEP* **05** (2012) 055, [arXiv:1202.5535 \[hep-ex\]](#).
- [16] *The Durham HepData Project*, <http://hepdata.cedar.ac.uk/view/ins1268975>. Accessed: 2014-02-04.
- [17] ATLAS Collaboration, *The ATLAS Experiment at the CERN Large Hadron Collider*, *JINST* **3** (2008) S08003.

- [18] M. Cacciari, G. Salam, and G. Soyez, *The Anti- $k(t)$ jet clustering algorithm*, *JHEP* **04** (2008) 063, [arXiv:0802.1189 \[hep-ph\]](#).
- [19] M. Cacciari, G. Salam, and G. Soyez, *FastJet User Manual*, *Eur. Phys. J. C* **72** (2012) 1896, [arXiv:1111.6097 \[hep-ph\]](#).
- [20] C. Buttar et al., *Standard Model Handles and Candles Working Group: Tools and Jets Summary Report*, [arXiv:0803.0678 \[hep-ph\]](#).
- [21] S. Frixione and G. Ridolfi, *Jet photoproduction at HERA*, *Nucl. Phys. B* **507** (1997) 315–333, [arXiv:hep-ph/9707345 \[hep-ph\]](#).
- [22] T. Sjöstrand, S. Mrenna, and P. Skands, *PYTHIA 6.4 Physics and Manual*, *JHEP* **05** (2006) 026, [arXiv:hep-ph/0603175 \[hep-ph\]](#).
- [23] ATLAS Collaboration, *ATLAS tunes of PYTHIA 6 and Pythia 8 for MC11*, ATL-PHYS-PUB-2011-009. <http://cds.cern.ch/record/1363300>.
- [24] B. Andersson and G. Gustafson, *Semiclassical Models for Gluon Jets and Leptoproduction Based on the Massless Relativistic String*, *Z. Phys. C* **3** (1980) 223.
- [25] T. Sjöstrand, S. Mrenna, and P. Skands, *A Brief Introduction to PYTHIA 8.1*, *Comput. Phys. Commun.* **178** (2008) 852–867, [arXiv:0710.3820 \[hep-ph\]](#).
- [26] R. Corke and T. Sjöstrand, *Interleaved Parton Showers and Tuning Prospects*, *JHEP* **03** (2011) 032, [arXiv:1011.1759 \[hep-ph\]](#).
- [27] A. Sherstnev and R. Thorne, *Different PDF approximations useful for LO Monte Carlo generators*, [arXiv:0807.2132 \[hep-ph\]](#).
- [28] M. Bahr et al., *Herwig++ Physics and Manual*, *Eur. Phys. J. C* **58** (2008) 639–707, [arXiv:0803.0883 \[hep-ph\]](#).
- [29] S. Gieseke et al., *Herwig++ 2.5 Release Note*, [arXiv:1102.1672 \[hep-ph\]](#).
- [30] G. Corcella et al., *HERWIG 6: An Event generator for hadron emission reactions with interfering gluons (including supersymmetric processes)*, *JHEP* **01** (2001) 010, [arXiv:hep-ph/0011363 \[hep-ph\]](#).
- [31] S. Gieseke, C. Rohr, and A. Siodmok, *Colour reconnections in Herwig++*, *Eur. Phys. J. C* **72** (2012) 2225, [arXiv:1206.0041 \[hep-ph\]](#).
- [32] B. Webber, *A QCD Model for Jet Fragmentation Including Soft Gluon Interference*, *Nucl. Phys. B* **238** (1984) 492.
- [33] M. Bahr, S. Gieseke, and M. Seymour, *Simulation of multiple partonic interactions in Herwig++*, *JHEP* **07** (2008) 076, [arXiv:0803.3633 \[hep-ph\]](#).
- [34] J. Pumplin et al., *New generation of parton distributions with uncertainties from global QCD analysis*, *JHEP* **07** (2002) 012, [arXiv:hep-ph/0201195 \[hep-ph\]](#).
- [35] ATLAS Collaboration, *The ATLAS Simulation Infrastructure*, *Eur. Phys. J. C* **70** (2010) 823–874, [arXiv:1005.4568 \[physics.ins-det\]](#).
- [36] GEANT4 Collaboration, S. Agostinelli et al., *GEANT4: A simulation toolkit*, *Nucl. Instrum. Meth. A* **506** (2003) 250–303.
- [37] T. Carli et al., *A posteriori inclusion of parton density functions in NLO QCD final-state calculations at hadron colliders: The APPLGRID Project*, *Eur. Phys. J. C* **66** (2010) 503–524, [arXiv:0911.2985 \[hep-ph\]](#).

- [38] H1 and ZEUS Collaborations, *HERAPDF 1.5*, H1prelim-10-142, ZEUS-prel-10-018.
http://www.desy.de/h1zeus/combined_results/index.php?do=proton_structure.
- [39] ATLAS Collaboration, *Measurement of the inclusive jet cross section in pp collisions at $\sqrt{s} = 2.76$ TeV and comparison to the inclusive jet cross section at $\sqrt{s} = 7$ TeV using the ATLAS detector*, *Eur. Phys. J. C* **73** (2013) 2509, [arXiv:1304.4739 \[hep-ex\]](#).
- [40] A. Martin, W. Stirling, R. Thorne, and G. Watt, *Parton distributions for the LHC*, *Eur. Phys. J. C* **63** (2009) 189–285, [arXiv:0901.0002 \[hep-ph\]](#).
- [41] R. Ball et al., *A first unbiased global NLO determination of parton distributions and their uncertainties*, *Nucl. Phys. B* **838** (2010) 136–206, [arXiv:1002.4407 \[hep-ph\]](#).
- [42] S. Forte, E. Laenen, P. Nason, and J. Rojo, *Heavy quarks in deep-inelastic scattering*, *Nucl. Phys. B* **834** (2010) 116–162, [arXiv:1001.2312 \[hep-ph\]](#).
- [43] R. Ball et al., *Parton distributions with LHC data*, *Nucl. Phys. B* **867** (2013) 244–289, [arXiv:1207.1303 \[hep-ph\]](#).
- [44] S. Alekhin, J. Bluemlein, and S.-O. Moch, *ABM11 PDFs and the cross section benchmarks in NNLO*, *PoS LL* **2012** (2012) 016, [arXiv:1302.1516 \[hep-ph\]](#).
- [45] S. Ellis, Z. Kunszt, and D. Soper, *Two jet production in hadron collisions at order α_s^3 in QCD*, *Phys. Rev. Lett.* **69** (1992) 1496–1499.
- [46] S. Frixione, P. Nason, and C. Oleari, *Matching NLO QCD computations with Parton Shower simulations: the POWHEG method*, *JHEP* **11** (2007) 070, [arXiv:0709.2092 \[hep-ph\]](#).
- [47] S. Alioli, P. Nason, C. Oleari, and E. Re, *A general framework for implementing NLO calculations in shower Monte Carlo programs: the POWHEG BOX*, *JHEP* **06** (2010) 043, [arXiv:1002.2581 \[hep-ph\]](#).
- [48] P. Nason, *MINT: A Computer program for adaptive Monte Carlo integration and generation of unweighted distributions*, [arXiv:0709.2085 \[hep-ph\]](#).
- [49] P. Skands, *Tuning Monte Carlo Generators: The Perugia Tunes*, *Phys. Rev. D* **82** (2010) 074018, [arXiv:1005.3457 \[hep-ph\]](#).
- [50] P. Nason and C. Oleari, *Generation cuts and Born suppression in POWHEG*, [arXiv:1303.3922 \[hep-ph\]](#).
- [51] S. Dittmaier, A. Huss, and C. Speckner, *Weak radiative corrections to dijet production at hadron colliders*, *JHEP* **11** (2012) 095, [arXiv:1210.0438 \[hep-ph\]](#). We thank Stefan Dittmaier, Alexander Huss, and Christian Speckner for providing calculations specific to this measurement.
- [52] H.-L. Lai et al., *Uncertainty induced by QCD coupling in the CTEQ global analysis of parton distributions*, *Phys. Rev. D* **82** (2010) 054021, [arXiv:1004.4624 \[hep-ph\]](#).
- [53] J. Pumplin et al., *Uncertainties of predictions from parton distribution functions. 2. The Hessian method*, *Phys. Rev. D* **65** (2001) 014013, [arXiv:hep-ph/0101032 \[hep-ph\]](#).
- [54] ATLAS Collaboration, *Improved luminosity determination in pp collisions at $\sqrt{s} = 7$ TeV using the ATLAS detector at the LHC*, *Eur. Phys. J. C* **73** (2013) 2518, [arXiv:1302.4393 \[hep-ex\]](#).
- [55] V. Lendermann et al., *Combining Triggers in HEP Data Analysis*, *Nucl. Instrum. Meth. A* **604** (2009) 707–718, [arXiv:0901.4118 \[hep-ex\]](#).

- [56] W. Lampl et al., *Calorimeter clustering algorithms: Description and performance*, ATL-LARG-PUB-2008-002. <http://cds.cern.ch/record/1099735>.
- [57] ATLAS Collaboration, *Local hadronic calibration*, ATL-LARG-PUB-2009-001-2. <http://cds.cern.ch/record/1112035>.
- [58] ATLAS Collaboration, *Pile-up corrections for jets from proton-proton collisions at $\sqrt{s} = 7$ TeV in ATLAS in 2011*, ATLAS-CONF-2012-064. <https://cds.cern.ch/record/1459529>.
- [59] ATLAS Collaboration, *Selection of jets produced in proton-proton collisions with the ATLAS detector using 2011 data*, ATLAS-CONF-2012-020. <http://cds.cern.ch/record/1430034>.
- [60] ATLAS Collaboration, *Measurement of inclusive jet and dijet cross sections in proton-proton collisions at 7 TeV centre-of-mass energy with the ATLAS detector*, *Eur. Phys. J. C* **71** (2011) 1512, [arXiv:1009.5908](https://arxiv.org/abs/1009.5908) [hep-ex].
- [61] A. Hocker and V. Kartvelishvili, *SVD approach to data unfolding*, *Nucl. Instrum. Meth. A* **372** (1996) 469–481, [arXiv:hep-ph/9509307](https://arxiv.org/abs/hep-ph/9509307) [hep-ph].
- [62] ATLAS Collaboration, *Jet energy measurement with the ATLAS detector in proton-proton collisions at $\sqrt{s} = 7$ TeV*, *Eur. Phys. J. C* **73** (2013) 2304, [arXiv:1112.6426](https://arxiv.org/abs/1112.6426) [hep-ex].
- [63] ATLAS Collaboration, *Jet energy resolution in proton-proton collisions at $\sqrt{s} = 7$ TeV recorded in 2010 with the ATLAS detector*, *Eur. Phys. J. C* **73** (2013) 2306, [arXiv:1210.6210](https://arxiv.org/abs/1210.6210) [hep-ex].
- [64] G. Bohm, *Introduction to statistics and data analysis for physicists*. Verl. Dt. Elektronen-Synchrotron, Hamburg, 2010.
- [65] A. Read, *Presentation of search results: the CLs technique*, *J. Phys. G* **28** (2002) 2693.
- [66] G. D’Agostini, *On the use of the covariance matrix to fit correlated data*, *Nucl. Instrum. Meth. A* **346** (1994) 306.
- [67] V. Blobel, *Some Comments on χ^2 Minimization Applications*, *eConf C* **030908** (2003) MOET002. <http://www.slac.stanford.edu/econf/C030908/proceedings.html>.
- [68] M. Botje, *Error estimates on parton density distributions*, *J. Phys. G* **28** (2002) 779–790, [arXiv:hep-ph/0110123](https://arxiv.org/abs/hep-ph/0110123) [hep-ph].
- [69] J. Gao et al., *Next-to-leading QCD effect to the quark compositeness search at the LHC*, *Phys. Rev. Lett.* **106** (2011) 142001, [arXiv:1101.4611](https://arxiv.org/abs/1101.4611) [hep-ph].
- [70] J. Gao, *CIJET: A program for computation of jet cross sections induced by quark contact interactions at hadron colliders*, *Comput. Phys. Commun.* **184** (2013) 2362–2366, [arXiv:1301.7263](https://arxiv.org/abs/1301.7263) [hep-ph].
- [71] CDF Collaboration, F. Abe et al., *Measurement of dijet angular distributions at CDF*, *Phys. Rev. Lett.* **77** (1996) 5336–5341, [arXiv:hep-ex/9609011](https://arxiv.org/abs/hep-ex/9609011) [hep-ex].
- [72] D0 Collaboration, V. Abazov et al., *Measurement of dijet angular distributions at $\sqrt{s} = 1.96$ TeV and searches for quark compositeness and extra spatial dimensions*, *Phys. Rev. Lett.* **103** (2009) 191803, [arXiv:0906.4819](https://arxiv.org/abs/0906.4819) [hep-ex].

The ATLAS Collaboration

G. Aad⁴⁸, T. Abajyan²¹, B. Abbott¹¹², J. Abdallah¹², S. Abdel Khalek¹¹⁶, O. Abdinov¹¹, R. Aben¹⁰⁶, B. Abi¹¹³, M. Abolins⁸⁹, O.S. AbouZeid¹⁵⁹, H. Abramowicz¹⁵⁴, H. Abreu¹³⁷, Y. Abulaiti^{147a,147b}, B.S. Acharya^{165a,165b,a}, L. Adamczyk^{38a}, D.L. Adams²⁵, T.N. Addy⁵⁶, J. Adelman¹⁷⁷, S. Adomeit⁹⁹, T. Adye¹³⁰, S. Aefsky²³, T. Agatonovic-Jovin^{13b}, J.A. Aguilar-Saavedra^{125b,b}, M. Agustoni¹⁷, S.P. Ahlen²², A. Ahmad¹⁴⁹, F. Ahmadov^{64,c}, M. Ahsan⁴¹, G. Aielli^{134a,134b}, T.P.A. Åkesson⁸⁰, G. Akimoto¹⁵⁶, A.V. Akimov⁹⁵, M.A. Alam⁷⁶, J. Albert¹⁷⁰, S. Albrand⁵⁵, M.J. Alconada Verzini⁷⁰, M. Aleksa³⁰, I.N. Aleksandrov⁶⁴, F. Alessandria^{90a}, C. Alexa^{26a}, G. Alexander¹⁵⁴, G. Alexandre⁴⁹, T. Alexopoulos¹⁰, M. Alhroob^{165a,165c}, M. Aliev¹⁶, G. Alimonti^{90a}, L. Alio⁸⁴, J. Alison³¹, B.M.M. Allbrooke¹⁸, L.J. Allison⁷¹, P.P. Allport⁷³, S.E. Allwood-Spiers⁵³, J. Almond⁸³, A. Aloisio^{103a,103b}, R. Alon¹⁷³, A. Alonso³⁶, F. Alonso⁷⁰, A. Altheimer³⁵, B. Alvarez Gonzalez⁸⁹, M.G. Alviggi^{103a,103b}, K. Amako⁶⁵, Y. Amaral Coutinho^{24a}, C. Amelung²³, V.V. Ammosov^{129,*}, S.P. Amor Dos Santos^{125a}, A. Amorim^{125a,d}, S. Amoroso⁴⁸, N. Amram¹⁵⁴, G. Amundsen²³, C. Anastopoulos³⁰, L.S. Ancu¹⁷, N. Andari³⁰, T. Andeen³⁵, C.F. Anders^{58b}, G. Anders^{58a}, K.J. Anderson³¹, A. Andreazza^{90a,90b}, V. Andrei^{58a}, X.S. Anduaga⁷⁰, S. Angelidakis⁹, P. Anger⁴⁴, A. Angerami³⁵, F. Anghinolfi³⁰, A.V. Anisenkov¹⁰⁸, N. Anjos^{125a}, A. Annovi⁴⁷, A. Antonaki⁹, M. Antonelli⁴⁷, A. Antonov⁹⁷, J. Antos^{145b}, F. Anulli^{133a}, M. Aoki¹⁰², L. Aperio Bella¹⁸, R. Apolle^{119,e}, G. Arabidze⁸⁹, I. Aracena¹⁴⁴, Y. Arai⁶⁵, A.T.H. Arce⁴⁵, S. Arfaoui¹⁴⁹, J-F. Arguin⁹⁴, S. Argyropoulos⁴², E. Arik^{19a,*}, M. Arik^{19a}, A.J. Armbruster⁸⁸, O. Arnaez⁸², V. Arnal⁸¹, O. Arslan²¹, A. Artamonov⁹⁶, G. Artoni²³, S. Asai¹⁵⁶, N. Asbah⁹⁴, S. Ask²⁸, B. Åsman^{147a,147b}, L. Asquith⁶, K. Assamagan²⁵, R. Astalos^{145a}, A. Astbury¹⁷⁰, M. Atkinson¹⁶⁶, N.B. Atlay¹⁴², B. Auerbach⁶, E. Auge¹¹⁶, K. Augsten¹²⁷, M. Auresseau^{146b}, G. Avolio³⁰, G. Azuelos^{94,f}, Y. Azuma¹⁵⁶, M.A. Baak³⁰, C. Bacci^{135a,135b}, A.M. Bach¹⁵, H. Bachacou¹³⁷, K. Bachas¹⁵⁵, M. Backes³⁰, M. Backhaus²¹, J. Backus Mayes¹⁴⁴, E. Badescu^{26a}, P. Bagiacchi^{133a,133b}, P. Bagnaia^{133a,133b}, Y. Bai^{33a}, D.C. Bailey¹⁵⁹, T. Bain³⁵, J.T. Baines¹³⁰, O.K. Baker¹⁷⁷, S. Baker⁷⁷, P. Balek¹²⁸, F. Balli¹³⁷, E. Banas³⁹, Sw. Banerjee¹⁷⁴, D. Banfi³⁰, A. Bangert¹⁵¹, V. Bansal¹⁷⁰, H.S. Bansil¹⁸, L. Barak¹⁷³, S.P. Baranov⁹⁵, T. Barber⁴⁸, E.L. Barberio⁸⁷, D. Barberis^{50a,50b}, M. Barbero⁸⁴, T. Barillari¹⁰⁰, M. Barisonzi¹⁷⁶, T. Barklow¹⁴⁴, N. Barlow²⁸, B.M. Barnett¹³⁰, R.M. Barnett¹⁵, A. Baroncelli^{135a}, G. Barone⁴⁹, A.J. Barr¹¹⁹, F. Barreiro⁸¹, J. Barreiro Guimarães da Costa⁵⁷, R. Bartoldus¹⁴⁴, A.E. Barton⁷¹, P. Bartos^{145a}, V. Bartsch¹⁵⁰, A. Bassalat¹¹⁶, A. Basye¹⁶⁶, R.L. Bates⁵³, L. Batkova^{145a}, J.R. Batley²⁸, M. Battistin³⁰, F. Bauer¹³⁷, H.S. Bawa^{144,g}, T. Beau⁷⁹, P.H. Beauchemin¹⁶², R. Beccherle^{50a}, P. Bechtel²¹, H.P. Beck¹⁷, K. Becker¹⁷⁶, S. Becker⁹⁹, M. Beckingham¹³⁹, A.J. Beddall^{19c}, A. Beddall^{19c}, S. Bedikian¹⁷⁷, V.A. Bednyakov⁶⁴, C.P. Bee⁸⁴, L.J. Beemster¹⁰⁶, T.A. Beermann¹⁷⁶, M. Begel²⁵, K. Behr¹¹⁹, C. Belanger-Champagne⁸⁶, P.J. Bell⁴⁹, W.H. Bell⁴⁹, G. Bella¹⁵⁴, L. Bellagamba^{20a}, A. Bellerive²⁹, M. Bellomo³⁰, A. Belloni⁵⁷, O.L. Beloborodova^{108,h}, K. Belotskiy⁹⁷, O. Beltramello³⁰, O. Benary¹⁵⁴, D. Benchekroun^{136a}, K. Bendtz^{147a,147b}, N. Benekos¹⁶⁶, Y. Benhammou¹⁵⁴, E. Benhar Noccioli⁴⁹, J.A. Benitez Garcia^{160b},

D.P. Benjamin⁴⁵, J.R. Bensinger²³, K. Benslama¹³¹, S. Bentvelsen¹⁰⁶, D. Berge³⁰,
 E. Bergeaas Kuutmann¹⁶, N. Berger⁵, F. Berghaus¹⁷⁰, E. Berglund¹⁰⁶, J. Beringer¹⁵,
 C. Bernard²², P. Bernat⁷⁷, R. Bernhard⁴⁸, C. Bernius⁷⁸, F.U. Bernlochner¹⁷⁰, T. Berry⁷⁶,
 P. Berta¹²⁸, C. Bertella⁸⁴, F. Bertolucci^{123a,123b}, M.I. Besana^{90a}, G.J. Besjes¹⁰⁵,
 O. Bessidskaia^{147a,147b}, N. Besson¹³⁷, S. Bethke¹⁰⁰, W. Bhimji⁴⁶, R.M. Bianchi¹²⁴,
 L. Bianchini²³, M. Bianco³⁰, O. Biebel⁹⁹, S.P. Bieniek⁷⁷, K. Bierwagen⁵⁴, J. Biesiada¹⁵,
 M. Biglietti^{135a}, J. Bilbao De Mendizabal⁴⁹, H. Bilokon⁴⁷, M. Bindi^{20a,20b}, S. Binet¹¹⁶,
 A. Bingul^{19c}, C. Bini^{133a,133b}, B. Bittner¹⁰⁰, C.W. Black¹⁵¹, J.E. Black¹⁴⁴, K.M. Black²²,
 D. Blackburn¹³⁹, R.E. Blair⁶, J.-B. Blanchard¹³⁷, T. Blazek^{145a}, I. Bloch⁴², C. Blocker²³,
 J. Blocki³⁹, W. Blum^{82,*}, U. Blumenschein⁵⁴, G.J. Bobbink¹⁰⁶, V.S. Bobrovnikov¹⁰⁸,
 S.S. Bocchetta⁸⁰, A. Bocci⁴⁵, C.R. Boddy¹¹⁹, M. Boehler⁴⁸, J. Boek¹⁷⁶, T.T. Boek¹⁷⁶,
 N. Boelaert³⁶, J.A. Bogaerts³⁰, A.G. Bogdanchikov¹⁰⁸, A. Bogouch^{91,*}, C. Boehm^{147a},
 J. Boehm¹²⁶, V. Boisvert⁷⁶, T. Bold^{38a}, V. Boldea^{26a}, A.S. Boldyrev⁹⁸, N.M. Bolnet¹³⁷,
 M. Bomben⁷⁹, M. Bona⁷⁵, M. Boonekamp¹³⁷, S. Bordini⁷⁹, C. Borer¹⁷, A. Borisov¹²⁹,
 G. Borissov⁷¹, M. Borri⁸³, S. Borroni⁴², J. Bortfeldt⁹⁹, V. Bortolotto^{135a,135b}, K. Bos¹⁰⁶,
 D. Boscherini^{20a}, M. Bosman¹², H. Boterenbrood¹⁰⁶, J. Bouchami⁹⁴, J. Boudreau¹²⁴,
 E.V. Bouhova-Thacker⁷¹, D. Boumediene³⁴, C. Bourdarios¹¹⁶, N. Bousson⁸⁴,
 S. Boutouil^{136d}, A. Boveia³¹, J. Boyd³⁰, I.R. Boyko⁶⁴, I. Bozovic-Jelisavcic^{13b},
 J. Bracinik¹⁸, P. Branchini^{135a}, A. Brandt⁸, G. Brandt¹⁵, O. Brandt⁵⁴, U. Bratzler¹⁵⁷,
 B. Brau⁸⁵, J.E. Brau¹¹⁵, H.M. Braun^{176,*}, S.F. Brazzale^{165a,165c}, B. Brelier¹⁵⁹,
 K. Brendlinger¹²¹, R. Brenner¹⁶⁷, S. Bressler¹⁷³, T.M. Bristow⁴⁶, D. Britton⁵³,
 F.M. Brochu²⁸, I. Brock²¹, R. Brock⁸⁹, F. Broggi^{90a}, C. Bromberg⁸⁹, J. Bronner¹⁰⁰,
 G. Brooijmans³⁵, T. Brooks⁷⁶, W.K. Brooks^{32b}, J. Brosamer¹⁵, E. Brost¹¹⁵, G. Brown⁸³,
 J. Brown⁵⁵, P.A. Bruckman de Renstrom³⁹, D. Bruncko^{145b}, R. Bruneliere⁴⁸, S. Brunet⁶⁰,
 A. Bruni^{20a}, G. Bruni^{20a}, M. Bruschi^{20a}, L. Bryngemark⁸⁰, T. Buanes¹⁴, Q. Buat⁵⁵,
 F. Bucci⁴⁹, P. Buchholz¹⁴², R.M. Buckingham¹¹⁹, A.G. Buckley⁴⁶, S.I. Buda^{26a},
 I.A. Budagov⁶⁴, B. Budick¹⁰⁹, F. Buehrer⁴⁸, L. Bugge¹¹⁸, M.K. Bugge¹¹⁸, O. Bulekov⁹⁷,
 A.C. Bundock⁷³, M. Bunse⁴³, H. Burkhardt³⁰, S. Burdin⁷³, T. Burgess¹⁴,
 B. Burghgrave¹⁰⁷, S. Burke¹³⁰, I. Burmeister⁴³, E. Busato³⁴, V. Buischer⁸², P. Bussey⁵³,
 C.P. Buszello¹⁶⁷, B. Butler⁵⁷, J.M. Butler²², A.I. Butt³, C.M. Buttar⁵³,
 J.M. Butterworth⁷⁷, W. Buttinger²⁸, A. Buzatu⁵³, M. Byszewski¹⁰, S. Cabrera Urbán¹⁶⁸,
 D. Caforio^{20a,20b}, O. Cakir^{4a}, P. Calafiura¹⁵, G. Calderini⁷⁹, P. Calfayan⁹⁹, R. Calkins¹⁰⁷,
 L.P. Caloba^{24a}, R. Caloi^{133a,133b}, D. Calvet³⁴, S. Calvet³⁴, R. Camacho Toro⁴⁹,
 P. Camarri^{134a,134b}, D. Cameron¹¹⁸, L.M. Caminada¹⁵, R. Caminal Armadans¹²,
 S. Campana³⁰, M. Campanelli⁷⁷, V. Canale^{103a,103b}, F. Canelli³¹, A. Canepa^{160a},
 J. Cantero⁸¹, R. Cantrill⁷⁶, T. Cao⁴⁰, M.D.M. Capeans Garrido³⁰, I. Caprini^{26a},
 M. Caprini^{26a}, M. Capua^{37a,37b}, R. Caputo⁸², R. Cardarelli^{134a}, T. Carli³⁰, G. Carlino^{103a},
 L. Carminati^{90a,90b}, S. Caron¹⁰⁵, E. Carquin^{32a}, G.D. Carrillo-Montoya^{146c}, A.A. Carter⁷⁵,
 J.R. Carter²⁸, J. Carvalho^{125a,i}, D. Casadei⁷⁷, M.P. Casado¹², C. Caso^{50a,50b,*},
 E. Castaneda-Miranda^{146b}, A. Castelli¹⁰⁶, V. Castillo Gimenez¹⁶⁸, N.F. Castro^{125a},
 P. Catastini⁵⁷, A. Catinaccio³⁰, J.R. Catmore⁷¹, A. Cattai³⁰, G. Cattani^{134a,134b},
 S. Caughron⁸⁹, V. Cavaliere¹⁶⁶, D. Cavalli^{90a}, M. Cavalli-Sforza¹², V. Cavasinni^{123a,123b},
 F. Ceradini^{135a,135b}, B. Cerio⁴⁵, K. Cerny¹²⁸, A.S. Cerqueira^{24b}, A. Cerri¹⁵⁰, L. Cerrito⁷⁵,

F. Cerutti¹⁵, A. Cervelli¹⁷, S.A. Cetin^{19b}, A. Chafaq^{136a}, D. Chakraborty¹⁰⁷,
 I. Chalupkova¹²⁸, K. Chan³, P. Chang¹⁶⁶, B. Chapleau⁸⁶, J.D. Chapman²⁸,
 D. Charfeddine¹¹⁶, D.G. Charlton¹⁸, V. Chavda⁸³, C.A. Chavez Barajas³⁰,
 S. Cheatham⁸⁶, S. Chekanov⁶, S.V. Chekulaev^{160a}, G.A. Chelkov⁶⁴, M.A. Chelstowska⁸⁸,
 C. Chen⁶³, H. Chen²⁵, K. Chen¹⁴⁹, L. Chen^{33d}, S. Chen^{33c}, X. Chen¹⁷⁴, Y. Chen³⁵,
 Y. Cheng³¹, A. Cheplakov⁶⁴, R. Cherkaoui El Moursli^{136e}, V. Chernyatin^{25,*}, E. Cheu⁷,
 L. Chevalier¹³⁷, V. Chiarella⁴⁷, G. Chiefari^{103a,103b}, J.T. Childers³⁰, A. Chilingarov⁷¹,
 G. Chiodini^{72a}, A.S. Chisholm¹⁸, R.T. Chislett⁷⁷, A. Chitan^{26a}, M.V. Chizhov⁶⁴,
 S. Chouridou⁹, B.K.B. Chow⁹⁹, I.A. Christidi⁷⁷, D. Chromek-Burckhart³⁰, M.L. Chu¹⁵²,
 J. Chudoba¹²⁶, G. Ciapetti^{133a,133b}, A.K. Ciftci^{4a}, R. Ciftci^{4a}, D. Cinca⁶², V. Cindro⁷⁴,
 A. Ciocio¹⁵, M. Cirilli⁸⁸, P. Cirkovic^{13b}, Z.H. Citron¹⁷³, M. Citterio^{90a}, M. Ciubancan^{26a},
 A. Clark⁴⁹, P.J. Clark⁴⁶, R.N. Clarke¹⁵, J.C. Clemens⁸⁴, B. Clement⁵⁵,
 C. Clement^{147a,147b}, Y. Coadou⁸⁴, M. Cobal^{165a,165c}, A. Coccaro¹³⁹, J. Cochran⁶³,
 S. Coelli^{90a}, L. Coffey²³, J.G. Cogan¹⁴⁴, J. Coggeshall¹⁶⁶, J. Colas⁵, B. Cole³⁵, S. Cole¹⁰⁷,
 A.P. Colijn¹⁰⁶, C. Collins-Tooth⁵³, J. Collot⁵⁵, T. Colombo^{58c}, G. Colon⁸⁵,
 G. Compostella¹⁰⁰, P. Conde Muiño^{125a}, E. Coniavitis¹⁶⁷, M.C. Conidi¹², I.A. Connelly⁷⁶,
 S.M. Consonni^{90a,90b}, V. Consorti⁴⁸, S. Constantinescu^{26a}, C. Conta^{120a,120b}, G. Conti⁵⁷,
 F. Conventi^{103a,j}, M. Cooke¹⁵, B.D. Cooper⁷⁷, A.M. Cooper-Sarkar¹¹⁹,
 N.J. Cooper-Smith⁷⁶, K. Copic¹⁵, T. Cornelissen¹⁷⁶, M. Corradi^{20a}, F. Corriveau^{86,k},
 A. Corso-Radu¹⁶⁴, A. Cortes-Gonzalez¹², G. Cortiana¹⁰⁰, G. Costa^{90a}, M.J. Costa¹⁶⁸,
 R. Costa Batalha Pedro^{125a}, D. Costanzo¹⁴⁰, D. Côte⁸, G. Cottin^{32a}, L. Courneyea¹⁷⁰,
 G. Cowan⁷⁶, B.E. Cox⁸³, K. Cranmer¹⁰⁹, G. Cree²⁹, S. Crépe-Renaudin⁵⁵, F. Crescioli⁷⁹,
 M. Crispin Ortuzar¹¹⁹, M. Cristinziani²¹, G. Crosetti^{37a,37b}, C.-M. Cuciuc^{26a},
 C. Cuenca Almenar¹⁷⁷, T. Cuhadar Donszelmann¹⁴⁰, J. Cummings¹⁷⁷, M. Curatolo⁴⁷,
 C. Cuthbert¹⁵¹, H. Cziri¹⁴², P. Czodrowski⁴⁴, Z. Czyczula¹⁷⁷, S. D'Auria⁵³,
 M. D'Onofrio⁷³, A. D'Orazio^{133a,133b}, M.J. Da Cunha Sargedas De Sousa^{125a},
 C. Da Via⁸³, W. Dabrowski^{38a}, A. Dafinca¹¹⁹, T. Dai⁸⁸, F. Dallaire⁹⁴, C. Dallapiccola⁸⁵,
 M. Dam³⁶, A.C. Daniells¹⁸, M. Dano Hoffmann³⁶, V. Dao¹⁰⁵, G. Darbo^{50a},
 G.L. Darlea^{26c}, S. Darmora⁸, J.A. Dassoulas⁴², W. Davey²¹, C. David¹⁷⁰, T. Davidek¹²⁸,
 E. Davies^{119,e}, M. Davies⁹⁴, O. Davignon⁷⁹, A.R. Davison⁷⁷, Y. Davygora^{58a}, E. Dawe¹⁴³,
 I. Dawson¹⁴⁰, R.K. Daya-Ishmukhametova²³, K. De⁸, R. de Asmundis^{103a},
 S. De Castro^{20a,20b}, S. De Cecco⁷⁹, J. de Graat⁹⁹, N. De Groot¹⁰⁵, P. de Jong¹⁰⁶,
 C. De La Taille¹¹⁶, H. De la Torre⁸¹, F. De Lorenzi⁶³, L. De Nooij¹⁰⁶, D. De Pedis^{133a},
 A. De Salvo^{133a}, U. De Sanctis^{165a,165c}, A. De Santo¹⁵⁰, J.B. De Vivie De Regie¹¹⁶,
 G. De Zorzi^{133a,133b}, W.J. Dearnaley⁷¹, R. Debbe²⁵, C. Debenedetti⁴⁶, B. Dechenaux⁵⁵,
 D.V. Dedovich⁶⁴, J. Degenhardt¹²¹, J. Del Peso⁸¹, T. Del Prete^{123a,123b}, T. Delemontex⁵⁵,
 F. Deliot¹³⁷, M. Deliyergiyev⁷⁴, A. Dell'Acqua³⁰, L. Dell'Asta²², M. Della Pietra^{103a,j},
 D. della Volpe^{103a,103b}, M. Delmastro⁵, P.A. Delsart⁵⁵, C. Deluca¹⁰⁶, S. Demers¹⁷⁷,
 M. Demichev⁶⁴, A. Demilly⁷⁹, B. Demirköz^{12,l}, S.P. Denisov¹²⁹, D. Derendarz³⁹,
 J.E. Derkaoui^{136d}, F. Derue⁷⁹, P. Dervan⁷³, K. Desch²¹, P.O. Deviveiros¹⁰⁶,
 A. Dewhurst¹³⁰, B. DeWilde¹⁴⁹, S. Dhaliwal¹⁰⁶, R. Dhullipudi^{78,m}, A. Di Ciaccio^{134a,134b},
 L. Di Ciaccio⁵, C. Di Donato^{103a,103b}, A. Di Girolamo³⁰, B. Di Girolamo³⁰,
 A. Di Mattia¹⁵³, B. Di Micco^{135a,135b}, R. Di Nardo⁴⁷, A. Di Simone⁴⁸, R. Di Sipio^{20a,20b},

D. Di Valentino²⁹, M.A. Diaz^{32a}, E.B. Diehl⁸⁸, J. Dietrich⁴², T.A. Dietzsch^{58a}, S. Diglio⁸⁷,
 K. Dindar Yagci⁴⁰, J. Dingfelder²¹, C. Dionisi^{133a,133b}, P. Dita^{26a}, S. Dita^{26a}, F. Dittus³⁰,
 F. Djama⁸⁴, T. Djobava^{51b}, M.A.B. do Vale^{24c}, A. Do Valle Wemans^{125a,n}, T.K.O. Doan⁵,
 D. Dobos³⁰, E. Dobson⁷⁷, J. Dodd³⁵, C. Doglioni⁴⁹, T. Doherty⁵³, T. Dohmae¹⁵⁶,
 J. Dolejsi¹²⁸, Z. Dolezal¹²⁸, B.A. Dolgoshein^{97,*}, M. Donadelli^{24d}, S. Donati^{123a,123b},
 P. Dondero^{120a,120b}, J. Donini³⁴, J. Dopke³⁰, A. Doria^{103a}, A. Dos Anjos¹⁷⁴,
 A. Dotti^{123a,123b}, M.T. Dova⁷⁰, A.T. Doyle⁵³, M. Dris¹⁰, J. Dubbert⁸⁸, S. Dube¹⁵,
 E. Dubreuil³⁴, E. Duchovni¹⁷³, G. Duckeck⁹⁹, O.A. Ducu^{26a}, D. Duda¹⁷⁶, A. Dudarev³⁰,
 F. Dudziak⁶³, L. DufLOT¹¹⁶, L. Duguid⁷⁶, M. Dührssen³⁰, M. Dunford^{58a},
 H. Duran Yildiz^{4a}, M. Düren⁵², M. Dwuznik^{38a}, J. Ebke⁹⁹, W. Edson², C.A. Edwards⁷⁶,
 N.C. Edwards⁴⁶, W. Ehrenfeld²¹, T. Eifert¹⁴⁴, G. Eigen¹⁴, K. Einsweiler¹⁵,
 E. Eisenhandler⁷⁵, T. Ekelof¹⁶⁷, M. El Kacimi^{136c}, M. Ellert¹⁶⁷, S. Elles⁵, F. Ellinghaus⁸²,
 K. Ellis⁷⁵, N. Ellis³⁰, J. Elmsheuser⁹⁹, M. Elsing³⁰, D. Emeliyanov¹³⁰, Y. Enari¹⁵⁶,
 O.C. Endner⁸², M. Endo¹¹⁷, R. Engelmann¹⁴⁹, J. Erdmann¹⁷⁷, A. Ereditato¹⁷,
 D. Eriksson^{147a}, G. Ernis¹⁷⁶, J. Ernst², M. Ernst²⁵, J. Ernwein¹³⁷, D. Errede¹⁶⁶,
 S. Errede¹⁶⁶, E. Ertel⁸², M. Escalier¹¹⁶, H. Esch⁴³, C. Escobar¹²⁴, X. Espinal Curull¹²,
 B. Esposito⁴⁷, F. Etienne⁸⁴, A.I. Etienvre¹³⁷, E. Etzion¹⁵⁴, D. Evangelakou⁵⁴, H. Evans⁶⁰,
 L. Fabbri^{20a,20b}, G. Facini³⁰, R.M. Fakhruddinov¹²⁹, S. Falciano^{133a}, Y. Fang^{33a},
 M. Fanti^{90a,90b}, A. Farbin⁸, A. Farilla^{135a}, T. Farooque¹⁵⁹, S. Farrell¹⁶⁴,
 S.M. Farrington¹⁷¹, P. Farthouat³⁰, F. Fassi¹⁶⁸, P. Fassnacht³⁰, D. Fassouliotis⁹,
 B. Fatholahzadeh¹⁵⁹, A. Favareto^{50a,50b}, L. Fayard¹¹⁶, P. Federic^{145a}, O.L. Fedin¹²²,
 W. Fedorko¹⁶⁹, M. Fehling-Kaschek⁴⁸, L. Felgioni⁸⁴, C. Feng^{33d}, E.J. Feng⁶, H. Feng⁸⁸,
 A.B. Fenyuk¹²⁹, W. Fernando⁶, S. Ferrag⁵³, J. Ferrando⁵³, V. Ferrara⁴², A. Ferrari¹⁶⁷,
 P. Ferrari¹⁰⁶, R. Ferrari^{120a}, D.E. Ferreira de Lima⁵³, A. Ferrer¹⁶⁸, D. Ferrere⁴⁹,
 C. Ferretti⁸⁸, A. Ferretto Parodi^{50a,50b}, M. Fiascaris³¹, F. Fiedler⁸², A. Filipčič⁷⁴,
 M. Filipuzzi⁴², F. Filthaut¹⁰⁵, M. Fincke-Keeler¹⁷⁰, K.D. Finelli⁴⁵, M.C.N. Fiolhais^{125a,i},
 L. Fiorini¹⁶⁸, A. Firan⁴⁰, J. Fischer¹⁷⁶, M.J. Fisher¹¹⁰, E.A. Fitzgerald²³, M. Flechl⁴⁸,
 I. Fleck¹⁴², P. Fleischmann¹⁷⁵, S. Fleischmann¹⁷⁶, G.T. Fletcher¹⁴⁰, G. Fletcher⁷⁵,
 T. Flick¹⁷⁶, A. Floderus⁸⁰, L.R. Flores Castillo¹⁷⁴, A.C. Florez Bustos^{160b},
 M.J. Flowerdew¹⁰⁰, T. Fonseca Martin¹⁷, A. Formica¹³⁷, A. Forti⁸³, D. Fortin^{160a},
 D. Fournier¹¹⁶, H. Fox⁷¹, P. Francavilla¹², M. Franchini^{20a,20b}, S. Franchino³⁰,
 D. Francis³⁰, M. Franklin⁵⁷, S. Franz⁶¹, M. Fraternali^{120a,120b}, S. Fratina¹²¹, S.T. French²⁸,
 C. Friedrich⁴², F. Friedrich⁴⁴, D. Froidevaux³⁰, J.A. Frost²⁸, C. Fukunaga¹⁵⁷,
 E. Fullana Torregrosa¹²⁸, B.G. Fulson¹⁴⁴, J. Fuster¹⁶⁸, C. Gabaldon⁵⁵, O. Gabizon¹⁷³,
 A. Gabrielli^{20a,20b}, A. Gabrielli^{133a,133b}, S. Gadatsch¹⁰⁶, T. Gadfort²⁵, S. Gadomski⁴⁹,
 G. Gagliardi^{50a,50b}, P. Gagnon⁶⁰, C. Galea⁹⁹, B. Galhardo^{125a}, E.J. Gallas¹¹⁹, V. Gallo¹⁷,
 B.J. Gallop¹³⁰, P. Gallus¹²⁷, G. Galster³⁶, K.K. Gan¹¹⁰, R.P. Gandrajula⁶², J. Gao^{33b,o},
 Y.S. Gao^{144,g}, F.M. Garay Walls⁴⁶, F. Garbersson¹⁷⁷, C. García¹⁶⁸, J.E. García Navarro¹⁶⁸,
 M. Garcia-Sciveres¹⁵, R.W. Gardner³¹, N. Garelli¹⁴⁴, V. Garonne³⁰, C. Gatti⁴⁷,
 G. Gaudio^{120a}, B. Gaur¹⁴², L. Gauthier⁹⁴, P. Gauzzi^{133a,133b}, I.L. Gavrilenko⁹⁵, C. Gay¹⁶⁹,
 G. Gaycken²¹, E.N. Gazis¹⁰, P. Ge^{33d,p}, Z. Gece¹⁶⁹, C.N.P. Gee¹³⁰, D.A.A. Geerts¹⁰⁶,
 Ch. Geich-Gimbel²¹, K. Gellerstedt^{147a,147b}, C. Gemme^{50a}, A. Gemmel⁵³, M.H. Genest⁵⁵,
 S. Gentile^{133a,133b}, M. George⁵⁴, S. George⁷⁶, D. Gerbaudo¹⁶⁴, A. Gershon¹⁵⁴,

H. Ghazlane^{136b}, N. Ghodbane³⁴, B. Giacobbe^{20a}, S. Giagu^{133a,133b}, V. Giangiobbe¹²,
 P. Giannetti^{123a,123b}, F. Gianotti³⁰, B. Gibbard²⁵, S.M. Gibson⁷⁶, M. Gilchriese¹⁵,
 T.P.S. Gillam²⁸, D. Gillberg³⁰, A.R. Gillman¹³⁰, D.M. Gingrich^{3,f}, N. Giokaris⁹,
 M.P. Giordani^{165a,165c}, R. Giordano^{103a,103b}, F.M. Giorgi¹⁶, P. Giovannini¹⁰⁰,
 P.F. Giraud¹³⁷, D. Giugni^{90a}, C. Giuliani⁴⁸, M. Giunta⁹⁴, B.K. Gjelsten¹¹⁸, I. Gkialas^{155,q},
 L.K. Gladilin⁹⁸, C. Glasman⁸¹, J. Glatzer²¹, A. Glazov⁴², G.L. Glonti⁶⁴,
 M. Goblirsch-Kolb¹⁰⁰, J.R. Goddard⁷⁵, J. Godfrey¹⁴³, J. Godlewski³⁰, C. Goeringer⁸²,
 S. Goldfarb⁸⁸, T. Golling¹⁷⁷, D. Golubkov¹²⁹, A. Gomes^{125a,d}, L.S. Gomez Fajardo⁴²,
 R. Gonalo⁷⁶, J. Goncalves Pinto Firmino Da Costa⁴², L. Gonella²¹,
 S. Gonzalez de la Hoz¹⁶⁸, G. Gonzalez Parra¹², M.L. Gonzalez Silva²⁷,
 S. Gonzalez-Sevilla⁴⁹, J.J. Goodson¹⁴⁹, L. Goossens³⁰, P.A. Gorbounov⁹⁶, H.A. Gordon²⁵,
 I. Gorelov¹⁰⁴, G. Gorfine¹⁷⁶, B. Gorini³⁰, E. Gorini^{72a,72b}, A. Gorišek⁷⁴, E. Gornicki³⁹,
 A.T. Goshaw⁶, C. Gossling⁴³, M.I. Gostkin⁶⁴, M. Gouighri^{136a}, D. Goujdami^{136c},
 M.P. Goulette⁴⁹, A.G. Goussiou¹³⁹, C. Goy⁵, S. Gozpinar²³, H.M.X. Grabas¹³⁷,
 L. Graber⁵⁴, I. Grabowska-Bold^{38a}, P. Grafstrom^{20a,20b}, K-J. Grahm⁴², J. Gramling⁴⁹,
 E. Gramstad¹¹⁸, F. Grancagnolo^{72a}, S. Grancagnolo¹⁶, V. Grassi¹⁴⁹, V. Gratchev¹²²,
 H.M. Gray³⁰, J.A. Gray¹⁴⁹, E. Graziani^{135a}, O.G. Grebenyuk¹²², Z.D. Greenwood^{78,m},
 K. Gregersen³⁶, I.M. Gregor⁴², P. Grenier¹⁴⁴, J. Griffiths⁸, N. Grigalashvili⁶⁴,
 A.A. Grillo¹³⁸, K. Grimm⁷¹, S. Grinstein^{12,r}, Ph. Gris³⁴, Y.V. Grishkevich⁹⁸,
 J.-F. Grivaz¹¹⁶, J.P. Grohs⁴⁴, A. Grohsjean⁴², E. Gross¹⁷³, J. Grosse-Knetter⁵⁴,
 G.C. Grossi^{134a,134b}, J. Groth-Jensen¹⁷³, Z.J. Grout¹⁵⁰, K. Grybel¹⁴², F. Guescini⁴⁹,
 D. Guest¹⁷⁷, O. Gueta¹⁵⁴, C. Guicheney³⁴, E. Guido^{50a,50b}, T. Guillemin¹¹⁶, S. Guindon²,
 U. Gul⁵³, C. Gumpert⁴⁴, J. Gunther¹²⁷, J. Guo³⁵, S. Gupta¹¹⁹, P. Gutierrez¹¹²,
 N.G. Gutierrez Ortiz⁵³, C. Gutsche⁷⁷, N. Guttman¹⁵⁴, C. Guyot¹³⁷, C. Gwenlan¹¹⁹,
 C.B. Gwilliam⁷³, A. Haas¹⁰⁹, C. Haber¹⁵, H.K. Hadavand⁸, P. Haefner²¹, S. Hageboeck²¹,
 Z. Hajduk³⁹, H. Hakobyan¹⁷⁸, D. Hall¹¹⁹, G. Halladjian⁸⁹, K. Hamacher¹⁷⁶, P. Hamal¹¹⁴,
 K. Hamano⁸⁷, M. Hamer⁵⁴, A. Hamilton^{146a,s}, S. Hamilton¹⁶², L. Han^{33b}, K. Hanagaki¹¹⁷,
 K. Hanawa¹⁵⁶, M. Hance¹⁵, P. Hanke^{58a}, J.R. Hansen³⁶, J.B. Hansen³⁶, J.D. Hansen³⁶,
 P.H. Hansen³⁶, P. Hansson¹⁴⁴, K. Hara¹⁶¹, A.S. Hard¹⁷⁴, T. Harenberg¹⁷⁶, S. Harkusha⁹¹,
 D. Harper⁸⁸, R.D. Harrington⁴⁶, O.M. Harris¹³⁹, P.F. Harrison¹⁷¹, F. Hartjes¹⁰⁶,
 A. Harvey⁵⁶, S. Hasegawa¹⁰², Y. Hasegawa¹⁴¹, S. Hassani¹³⁷, S. Haug¹⁷, M. Hauschild³⁰,
 R. Hauser⁸⁹, M. Havranek²¹, C.M. Hawkes¹⁸, R.J. Hawkings³⁰, A.D. Hawkins⁸⁰,
 T. Hayashi¹⁶¹, D. Hayden⁸⁹, C.P. Hays¹¹⁹, H.S. Hayward⁷³, S.J. Haywood¹³⁰, S.J. Head¹⁸,
 T. Heck⁸², V. Hedberg⁸⁰, L. Heelan⁸, S. Heim¹²¹, B. Heinemann¹⁵, S. Heisterkamp³⁶,
 J. Hejbal¹²⁶, L. Helary²², C. Heller⁹⁹, M. Heller³⁰, S. Hellman^{147a,147b}, D. Hellmich²¹,
 C. Helsen³⁰, J. Henderson¹¹⁹, R.C.W. Henderson⁷¹, A. Henrichs¹⁷⁷,
 A.M. Henriques Correia³⁰, S. Henrot-Versille¹¹⁶, C. Hensel⁵⁴, G.H. Herbert¹⁶,
 C.M. Hernandez⁸, Y. Hernandez Jimenez¹⁶⁸, R. Herrberg-Schubert¹⁶, G. Herten⁴⁸,
 R. Hertenberger⁹⁹, L. Hervas³⁰, G.G. Hesketh⁷⁷, N.P. Hesse¹⁰⁶, R. Hickling⁷⁵,
 E. Higon-Rodriguez¹⁶⁸, J.C. Hill²⁸, K.H. Hiller⁴², S. Hillert²¹, S.J. Hillier¹⁸, I. Hinchliffe¹⁵,
 E. Hines¹²¹, M. Hirose¹¹⁷, D. Hirschbuehl¹⁷⁶, J. Hobbs¹⁴⁹, N. Hod¹⁰⁶,
 M.C. Hodgkinson¹⁴⁰, P. Hodgson¹⁴⁰, A. Hoecker³⁰, M.R. Hoferkamp¹⁰⁴, J. Hoffman⁴⁰,
 D. Hoffmann⁸⁴, J.I. Hofmann^{58a}, M. Hohlfeld⁸², T.R. Holmes¹⁵, T.M. Hong¹²¹,

L. Hooft van Huysduynen¹⁰⁹, J.-Y. Hostachy⁵⁵, S. Hou¹⁵², A. Hoummada^{136a},
 J. Howard¹¹⁹, J. Howarth⁸³, M. Hrabovsky¹¹⁴, I. Hristova¹⁶, J. Hrivnac¹¹⁶, T. Hryn'ova⁵,
 P.J. Hsu⁸², S.-C. Hsu¹³⁹, D. Hu³⁵, X. Hu²⁵, Y. Huang^{146c}, Z. Hubacek³⁰, F. Hubaut⁸⁴,
 F. Huegging²¹, A. Huettmann⁴², T.B. Huffman¹¹⁹, E.W. Hughes³⁵, G. Hughes⁷¹,
 M. Huhtinen³⁰, T.A. Hülsing⁸², M. Hurwitz¹⁵, N. Huseynov^{64,c}, J. Huston⁸⁹, J. Huth⁵⁷,
 G. Iacobucci⁴⁹, G. Iakovidis¹⁰, I. Ibragimov¹⁴², L. Iconomidou-Fayard¹¹⁶, J. Idarraga¹¹⁶,
 E. Ideal¹⁷⁷, P. Iengo^{103a}, O. Igonkina¹⁰⁶, T. Iizawa¹⁷², Y. Ikegami⁶⁵, K. Ikematsu¹⁴²,
 M. Ikeno⁶⁵, D. Iliadis¹⁵⁵, N. Ilic¹⁵⁹, Y. Inamaru⁶⁶, T. Ince¹⁰⁰, P. Ioannou⁹, M. Iodice^{135a},
 K. Iordanidou⁹, V. Ippolito^{133a,133b}, A. Irls Quiles¹⁶⁸, C. Isaksson¹⁶⁷, M. Ishino⁶⁷,
 M. Ishitsuka¹⁵⁸, R. Ishmukhametov¹¹⁰, C. Issever¹¹⁹, S. Istin^{19a}, A.V. Ivashin¹²⁹,
 W. Iwanski³⁹, H. Iwasaki⁶⁵, J.M. Izen⁴¹, V. Izzo^{103a}, B. Jackson¹²¹, J.N. Jackson⁷³,
 M. Jackson⁷³, P. Jackson¹, M.R. Jaekel³⁰, V. Jain², K. Jakobs⁴⁸, S. Jakobsen³⁶,
 T. Jakoubek¹²⁶, J. Jakubek¹²⁷, D.O. Jamin¹⁵², D.K. Jana¹¹², E. Jansen⁷⁷, H. Jansen³⁰,
 J. Janssen²¹, M. Janus¹⁷¹, R.C. Jared¹⁷⁴, G. Jarlskog⁸⁰, L. Jeanty⁵⁷, G.-Y. Jeng¹⁵¹,
 I. Jen-La Plante³¹, D. Jennens⁸⁷, P. Jenni^{48,t}, J. Jentzsch⁴³, C. Jeske¹⁷¹, S. Jézéquel⁵,
 M.K. Jha^{20a}, H. Ji¹⁷⁴, W. Ji⁸², J. Jia¹⁴⁹, Y. Jiang^{33b}, M. Jimenez Belenguer⁴², S. Jin^{33a},
 A. Jinaru^{26a}, O. Jinnouchi¹⁵⁸, M.D. Joergensen³⁶, D. Joffe⁴⁰, K.E. Johansson^{147a},
 P. Johansson¹⁴⁰, K.A. Johns⁷, K. Jon-And^{147a,147b}, G. Jones¹⁷¹, R.W.L. Jones⁷¹,
 T.J. Jones⁷³, P.M. Jorge^{125a}, K.D. Joshi⁸³, J. Jovicevic¹⁴⁸, X. Ju¹⁷⁴, C.A. Jung⁴³,
 R.M. Jungst³⁰, P. Jussel⁶¹, A. Juste Rozas^{12,r}, M. Kaci¹⁶⁸, A. Kaczmarska³⁹,
 P. Kadlecik³⁶, M. Kado¹¹⁶, H. Kagan¹¹⁰, M. Kagan¹⁴⁴, E. Kajomovitz⁴⁵, S. Kalinin¹⁷⁶,
 S. Kama⁴⁰, N. Kanaya¹⁵⁶, M. Kaneda³⁰, S. Kaneti²⁸, T. Kanno¹⁵⁸, V.A. Kantserov⁹⁷,
 J. Kanzaki⁶⁵, B. Kaplan¹⁰⁹, A. Kapliy³¹, D. Kar⁵³, K. Karakostas¹⁰, N. Karastathis¹⁰,
 M. Karnevskiy⁸², S.N. Karpov⁶⁴, K. Karthik¹⁰⁹, V. Kartvelishvili⁷¹, A.N. Karyukhin¹²⁹,
 L. Kashif¹⁷⁴, G. Kasieczka^{58b}, R.D. Kass¹¹⁰, A. Kastanas¹⁴, Y. Kataoka¹⁵⁶, A. Katre⁴⁹,
 J. Katzy⁴², V. Kaushik⁷, K. Kawagoe⁶⁹, T. Kawamoto¹⁵⁶, G. Kawamura⁵⁴, S. Kazama¹⁵⁶,
 V.F. Kazanin¹⁰⁸, M.Y. Kazarinov⁶⁴, R. Keeler¹⁷⁰, P.T. Keener¹²¹, R. Kehoe⁴⁰, M. Keil⁵⁴,
 J.S. Keller¹³⁹, H. Keoshkerian⁵, O. Kepka¹²⁶, B.P. Kerševan⁷⁴, S. Kersten¹⁷⁶,
 K. Kessoku¹⁵⁶, J. Keung¹⁵⁹, F. Khalil-zada¹¹, H. Khandanyan^{147a,147b}, A. Khanov¹¹³,
 D. Kharchenko⁶⁴, A. Khodinov⁹⁷, A. Khomich^{58a}, T.J. Khoo²⁸, G. Khoriauli²¹,
 A. Khoroshilov¹⁷⁶, V. Khovanskiy⁹⁶, E. Khramov⁶⁴, J. Khubua^{51b}, H. Kim^{147a,147b},
 S.H. Kim¹⁶¹, N. Kimura¹⁷², O. Kind¹⁶, B.T. King⁷³, M. King⁶⁶, R.S.B. King¹¹⁹,
 S.B. King¹⁶⁹, J. Kirk¹³⁰, A.E. Kiryunin¹⁰⁰, T. Kishimoto⁶⁶, D. Kisielewska^{38a},
 T. Kitamura⁶⁶, T. Kittelmann¹²⁴, K. Kiuchi¹⁶¹, E. Kladiva^{145b}, M. Klein⁷³, U. Klein⁷³,
 K. Kleinknecht⁸², P. Klimek^{147a,147b}, A. Klimentov²⁵, R. Klingenberg⁴³, J.A. Klinger⁸³,
 E.B. Klinkby³⁶, T. Klioutchnikova³⁰, P.F. Klok¹⁰⁵, E.-E. Kluge^{58a}, P. Kluit¹⁰⁶,
 S. Kluth¹⁰⁰, E. Kneringer⁶¹, E.B.F.G. Knoops⁸⁴, A. Knue⁵⁴, T. Kobayashi¹⁵⁶, M. Kobel⁴⁴,
 M. Kocian¹⁴⁴, P. Kodys¹²⁸, S. Koenig⁸², P. Koevesarki²¹, T. Koffas²⁹, E. Koffeman¹⁰⁶,
 L.A. Kogan¹¹⁹, S. Kohlmann¹⁷⁶, Z. Kohout¹²⁷, T. Kohriki⁶⁵, T. Koi¹⁴⁴, H. Kolanoski¹⁶,
 I. Koletsou⁵, J. Koll⁸⁹, A.A. Komar^{95,*}, Y. Komori¹⁵⁶, T. Kondo⁶⁵, K. Köneke⁴⁸,
 A.C. König¹⁰⁵, T. Kono^{65,u}, R. Konoplich^{109,v}, N. Konstantinidis⁷⁷, R. Kopeliansky¹⁵³,
 S. Koperny^{38a}, L. Köpke⁸², A.K. Kopp⁴⁸, K. Korcyl³⁹, K. Kordas¹⁵⁵, A. Korn⁴⁶,
 A.A. Korol¹⁰⁸, I. Korolkov¹², E.V. Korolkova¹⁴⁰, V.A. Korotkov¹²⁹, O. Kortner¹⁰⁰,

S. Kortner¹⁰⁰, V.V. Kostyukhin²¹, S. Kotov¹⁰⁰, V.M. Kotov⁶⁴, A. Kotwal⁴⁵,
 C. Kourkoumelis⁹, V. Kouskoura¹⁵⁵, A. Koutsman^{160a}, R. Kowalewski¹⁷⁰,
 T.Z. Kowalski^{38a}, W. Kozanecki¹³⁷, A.S. Kozhin¹²⁹, V. Kral¹²⁷, V.A. Kramarenko⁹⁸,
 G. Kramberger⁷⁴, M.W. Krasny⁷⁹, A. Krasznahorkay¹⁰⁹, J.K. Kraus²¹, A. Kravchenko²⁵,
 S. Kreiss¹⁰⁹, J. Kretzschmar⁷³, K. Kreutzfeldt⁵², N. Krieger⁵⁴, P. Krieger¹⁵⁹,
 K. Kroeninger⁵⁴, H. Kroha¹⁰⁰, J. Kroll¹²¹, J. Kroseberg²¹, J. Krstic^{13a}, U. Kruchonak⁶⁴,
 H. Krüger²¹, T. Kruker¹⁷, N. Krumnack⁶³, Z.V. Krumshteyn⁶⁴, A. Kruse¹⁷⁴,
 M.C. Kruse⁴⁵, M. Kruskal²², T. Kubota⁸⁷, S. Kудay^{4a}, S. Kuehn⁴⁸, A. Kugel^{58c},
 T. Kuhl⁴², V. Kukhtin⁶⁴, Y. Kulchitsky⁹¹, S. Kuleshov^{32b}, M. Kuna^{133a,133b}, J. Kunkle¹²¹,
 A. Kupco¹²⁶, H. Kurashige⁶⁶, M. Kurata¹⁶¹, Y.A. Kurochkin⁹¹, R. Kurumida⁶⁶,
 V. Kus¹²⁶, E.S. Kuwertz¹⁴⁸, M. Kuze¹⁵⁸, J. Kvita¹⁴³, R. Kwee¹⁶, A. La Rosa⁴⁹,
 L. La Rotonda^{37a,37b}, L. Labarga⁸¹, S. Lablak^{136a}, C. Lacasta¹⁶⁸, F. Lacava^{133a,133b},
 J. Lacey²⁹, H. Lacker¹⁶, D. Lacour⁷⁹, V.R. Lacuesta¹⁶⁸, E. Ladygin⁶⁴, R. Lafaye⁵,
 B. Laforge⁷⁹, T. Lagouri¹⁷⁷, S. Lai⁴⁸, H. Laier^{58a}, E. Laisne⁵⁵, L. Lambourne⁷⁷,
 C.L. Lampen⁷, W. Lampl⁷, E. Lançon¹³⁷, U. Landgraf⁴⁸, M.P.J. Landon⁷⁵, V.S. Lang^{58a},
 C. Lange⁴², A.J. Lankford¹⁶⁴, F. Lanni²⁵, K. Lantzsch³⁰, A. Lanza^{120a}, S. Laplace⁷⁹,
 C. Lapoire²¹, J.F. Laporte¹³⁷, T. Lari^{90a}, A. Larner¹¹⁹, M. Lassnig³⁰, P. Laurelli⁴⁷,
 V. Lavorini^{37a,37b}, W. Lavrijsen¹⁵, P. Laycock⁷³, B.T. Le⁵⁵, O. Le Dortz⁷⁹,
 E. Le Guirriec⁸⁴, E. Le Menedeu¹², T. LeCompte⁶, F. Ledroit-Guillon⁵⁵, C.A. Lee¹⁵²,
 H. Lee¹⁰⁶, J.S.H. Lee¹¹⁷, S.C. Lee¹⁵², L. Lee¹⁷⁷, G. Lefebvre⁷⁹, M. Lefebvre¹⁷⁰,
 F. Legger⁹⁹, C. Leggett¹⁵, A. Lehan⁷³, M. Lehmacher²¹, G. Lehmann Miotto³⁰, X. Lei⁷,
 A.G. Leister¹⁷⁷, M.A.L. Leite^{24d}, R. Leitner¹²⁸, D. Lellouch¹⁷³, B. Lemmer⁵⁴,
 V. Lendermann^{58a}, K.J.C. Leney^{146c}, T. Lenz¹⁰⁶, G. Lenzen¹⁷⁶, B. Lenzi³⁰, R. Leone⁷,
 K. Leonhardt⁴⁴, S. Leontsinis¹⁰, C. Leroy⁹⁴, J-R. Lessard¹⁷⁰, C.G. Lester²⁸,
 C.M. Lester¹²¹, J. Levêque⁵, D. Levin⁸⁸, L.J. Levinson¹⁷³, A. Lewis¹¹⁹, G.H. Lewis¹⁰⁹,
 A.M. Leyko²¹, M. Leyton¹⁶, B. Li^{33b,w}, B. Li⁸⁴, H. Li¹⁴⁹, H.L. Li³¹, S. Li⁴⁵, X. Li⁸⁸,
 Z. Liang^{119,x}, H. Liao³⁴, B. Liberti^{134a}, P. Lichard³⁰, K. Lie¹⁶⁶, J. Liebal²¹, W. Liebig¹⁴,
 C. Limbach²¹, A. Limosani⁸⁷, M. Limper⁶², S.C. Lin^{152,y}, F. Linde¹⁰⁶, B.E. Lindquist¹⁴⁹,
 J.T. Linnemann⁸⁹, E. Lipeles¹²¹, A. Lipniacka¹⁴, M. Lisovyi⁴², T.M. Liss¹⁶⁶, D. Lissauer²⁵,
 A. Lister¹⁶⁹, A.M. Litke¹³⁸, B. Liu¹⁵², D. Liu¹⁵², J.B. Liu^{33b}, K. Liu^{33b,z}, L. Liu⁸⁸,
 M. Liu⁴⁵, M. Liu^{33b}, Y. Liu^{33b}, M. Livan^{120a,120b}, S.S.A. Livermore¹¹⁹, A. Lleres⁵⁵,
 J. Llorente Merino⁸¹, S.L. Lloyd⁷⁵, F. Lo Sterzo¹⁵², E. Lobodzinska⁴², P. Loch⁷,
 W.S. Lockman¹³⁸, T. Loddenkoetter²¹, F.K. Loebinger⁸³, A.E. Loevschall-Jensen³⁶,
 A. Loginov¹⁷⁷, C.W. Loh¹⁶⁹, T. Lohse¹⁶, K. Lohwasser⁴⁸, M. Lokajicek¹²⁶,
 V.P. Lombardo⁵, J.D. Long⁸⁸, R.E. Long⁷¹, L. Lopes^{125a}, D. Lopez Mateos⁵⁷,
 B. Lopez Paredes¹⁴⁰, J. Lorenz⁹⁹, N. Lorenzo Martinez¹¹⁶, M. Losada¹⁶³, P. Loscutoff¹⁵,
 M.J. Losty^{160a,*}, X. Lou⁴¹, A. Lounis¹¹⁶, J. Love⁶, P.A. Love⁷¹, A.J. Lowe^{144,g}, F. Lu^{33a},
 H.J. Lubatti¹³⁹, C. Luci^{133a,133b}, A. Lucotte⁵⁵, D. Ludwig⁴², I. Ludwig⁴⁸, F. Luehring⁶⁰,
 W. Lukas⁶¹, L. Luminari^{133a}, E. Lund¹¹⁸, J. Lundberg^{147a,147b}, O. Lundberg^{147a,147b},
 B. Lund-Jensen¹⁴⁸, M. Lungwitz⁸², D. Lynn²⁵, R. Lysak¹²⁶, E. Lytken⁸⁰, H. Ma²⁵,
 L.L. Ma^{33d}, G. Maccarrone⁴⁷, A. Macchiolo¹⁰⁰, B. Maček⁷⁴, J. Machado Miguens^{125a},
 D. Macina³⁰, R. Mackeprang³⁶, R. Madar⁴⁸, R.J. Madaras¹⁵, H.J. Maddocks⁷¹,
 W.F. Mader⁴⁴, A. Madsen¹⁶⁷, M. Maeno⁸, T. Maeno²⁵, L. Magnoni¹⁶⁴, E. Magradze⁵⁴,

K. Mahboubi⁴⁸, J. Mahlstedt¹⁰⁶, S. Mahmoud⁷³, G. Mahout¹⁸, C. Maiani¹³⁷,
 C. Maidantchik^{24a}, A. Maio^{125a,d}, S. Majewski¹¹⁵, Y. Makida⁶⁵, N. Makovec¹¹⁶,
 P. Mal^{137,aa}, B. Malaescu⁷⁹, Pa. Malecki³⁹, V.P. Maleev¹²², F. Malek⁵⁵, U. Mallik⁶²,
 D. Malon⁶, C. Malone¹⁴⁴, S. Maltezos¹⁰, V.M. Malyshev¹⁰⁸, S. Malyukov³⁰,
 J. Mamuzic^{13b}, L. Mandelli^{90a}, I. Mandić⁷⁴, R. Mandrysch⁶², J. Maneira^{125a},
 A. Manfredini¹⁰⁰, L. Manhaes de Andrade Filho^{24b}, J.A. Manjarres Ramos¹³⁷, A. Mann⁹⁹,
 P.M. Manning¹³⁸, A. Manousakis-Katsikakis⁹, B. Mansoulie¹³⁷, R. Mantifel⁸⁶,
 L. Mapelli³⁰, L. March¹⁶⁸, J.F. Marchand²⁹, F. Marchese^{134a,134b}, G. Marchiori⁷⁹,
 M. Marcisovsky¹²⁶, C.P. Marino¹⁷⁰, C.N. Marques^{125a}, F. Marroquin^{24a}, Z. Marshall¹⁵,
 L.F. Marti¹⁷, S. Marti-Garcia¹⁶⁸, B. Martin³⁰, B. Martin⁸⁹, J.P. Martin⁹⁴, T.A. Martin¹⁷¹,
 V.J. Martin⁴⁶, B. Martin dit Latour⁴⁹, H. Martinez¹³⁷, M. Martinez^{12,r},
 S. Martin-Haugh¹³⁰, A.C. Martyniuk¹⁷⁰, M. Marx¹³⁹, F. Marzano^{133a}, A. Marzin¹¹²,
 L. Masetti⁸², T. Mashimo¹⁵⁶, R. Mashinistov⁹⁵, J. Masik⁸³, A.L. Maslennikov¹⁰⁸,
 I. Massa^{20a,20b}, N. Massol⁵, P. Mastrandrea¹⁴⁹, A. Mastroberardino^{37a,37b},
 T. Masubuchi¹⁵⁶, H. Matsunaga¹⁵⁶, T. Matsushita⁶⁶, P. Mättig¹⁷⁶, S. Mättig⁴²,
 J. Mattmann⁸², C. Mattravers^{119,e}, J. Maurer⁸⁴, S.J. Maxfield⁷³, D.A. Maximov^{108,h},
 R. Mazini¹⁵², L. Mazzaferro^{134a,134b}, M. Mazzanti^{90a}, G. Mc Goldrick¹⁵⁹, S.P. Mc Kee⁸⁸,
 A. McCarn⁸⁸, R.L. McCarthy¹⁴⁹, T.G. McCarthy²⁹, N.A. McCubbin¹³⁰,
 K.W. McFarlane^{56,*}, J.A. Mcfayden¹⁴⁰, G. Mchedlidze^{51b}, T. Mclaughlan¹⁸,
 S.J. McMahon¹³⁰, R.A. McPherson^{170,k}, A. Meade⁸⁵, J. Mechnich¹⁰⁶, M. Mechtel¹⁷⁶,
 M. Medinnis⁴², S. Meehan³¹, R. Meera-Lebbai¹¹², S. Mehlhase³⁶, A. Mehta⁷³,
 K. Meier^{58a}, C. Meineck⁹⁹, B. Meirose⁸⁰, C. Melachrinou³¹, B.R. Mellado Garcia^{146c},
 F. Meloni^{90a,90b}, L. Mendoza Navas¹⁶³, A. Mengarelli^{20a,20b}, S. Menke¹⁰⁰, E. Meoni¹⁶²,
 K.M. Mercurio⁵⁷, S. Mergelmeyer²¹, N. Meric¹³⁷, P. Mermod⁴⁹, L. Merola^{103a,103b},
 C. Meroni^{90a}, F.S. Merritt³¹, H. Merritt¹¹⁰, A. Messina^{30,ab}, J. Metcalfe²⁵, A.S. Mete¹⁶⁴,
 C. Meyer⁸², C. Meyer³¹, J.-P. Meyer¹³⁷, J. Meyer³⁰, J. Meyer⁵⁴, S. Michal³⁰,
 R.P. Middleton¹³⁰, S. Migas⁷³, L. Mijović¹³⁷, G. Mikenberg¹⁷³, M. Mikestikova¹²⁶,
 M. Mikuž⁷⁴, D.W. Miller³¹, C. Mills⁵⁷, A. Milov¹⁷³, D.A. Milstead^{147a,147b}, D. Milstein¹⁷³,
 A.A. Minaenko¹²⁹, M. Miñano Moya¹⁶⁸, I.A. Minashvili⁶⁴, A.I. Mincer¹⁰⁹, B. Mindur^{38a},
 M. Mineev⁶⁴, Y. Ming¹⁷⁴, L.M. Mir¹², G. Mirabelli^{133a}, T. Mitani¹⁷², J. Mitrevski¹³⁸,
 V.A. Mitsou¹⁶⁸, S. Mitsui⁶⁵, P.S. Miyagawa¹⁴⁰, J.U. Mjörnmark⁸⁰, T. Moa^{147a,147b},
 V. Moeller²⁸, S. Mohapatra¹⁴⁹, W. Mohr⁴⁸, S. Molander^{147a,147b}, R. Moles-Valls¹⁶⁸,
 A. Molfetas³⁰, K. Mönig⁴², C. Monini⁵⁵, J. Monk³⁶, E. Monnier⁸⁴, J. Montejo Berlingen¹²,
 F. Monticelli⁷⁰, S. Monzani^{20a,20b}, R.W. Moore³, C. Mora Herrera⁴⁹, A. Moraes⁵³,
 N. Morange⁶², J. Morel⁵⁴, D. Moreno⁸², M. Moreno Llácer¹⁶⁸, P. Morettini^{50a},
 M. Morgenstern⁴⁴, M. Morii⁵⁷, S. Moritz⁸², A.K. Morley¹⁴⁸, G. Mornacchi³⁰,
 J.D. Morris⁷⁵, L. Morvaj¹⁰², H.G. Moser¹⁰⁰, M. Mosidze^{51b}, J. Moss¹¹⁰, R. Mount¹⁴⁴,
 E. Mountricha^{10,ac}, S.V. Mouraviev^{95,*}, E.J.W. Moyse⁸⁵, R.D. Mudd¹⁸, F. Mueller^{58a},
 J. Mueller¹²⁴, K. Mueller²¹, T. Mueller²⁸, T. Mueller⁸², D. Muenstermann⁴⁹,
 Y. Munwes¹⁵⁴, J.A. Murillo Quijada¹⁸, W.J. Murray¹³⁰, I. Mussche¹⁰⁶, E. Musto¹⁵³,
 A.G. Myagkov^{129,ad}, M. Myska¹²⁶, O. Nackenhorst⁵⁴, J. Nadal⁵⁴, K. Nagai⁶¹, R. Nagai¹⁵⁸,
 Y. Nagai⁸⁴, K. Nagano⁶⁵, A. Nagarkar¹¹⁰, Y. Nagasaka⁵⁹, M. Nagel¹⁰⁰, A.M. Nairz³⁰,
 Y. Nakahama³⁰, K. Nakamura⁶⁵, T. Nakamura¹⁵⁶, I. Nakano¹¹¹, H. Namasivayam⁴¹,

G. Nanava²¹, A. Napier¹⁶², R. Narayan^{58b}, M. Nash^{77,e}, T. Nattermann²¹, T. Naumann⁴², G. Navarro¹⁶³, H.A. Neal⁸⁸, P.Yu. Nechaeva⁹⁵, T.J. Neep⁸³, A. Negri^{120a,120b}, G. Negri³⁰, M. Negrini^{20a}, S. Nektarijevic⁴⁹, A. Nelson¹⁶⁴, T.K. Nelson¹⁴⁴, S. Nemecek¹²⁶, P. Nemethy¹⁰⁹, A.A. Nepomuceno^{24a}, M. Nessi^{30,ae}, M.S. Neubauer¹⁶⁶, M. Neumann¹⁷⁶, A. Neusiedl⁸², R.M. Neves¹⁰⁹, P. Nevski²⁵, F.M. Newcomer¹²¹, P.R. Newman¹⁸, D.H. Nguyen⁶, V. Nguyen Thi Hong¹³⁷, R.B. Nickerson¹¹⁹, R. Nicolaidou¹³⁷, B. Nicquevert³⁰, J. Nielsen¹³⁸, N. Nikiforou³⁵, A. Nikiforov¹⁶, V. Nikolaenko^{129,ad}, I. Nikolic-Audit⁷⁹, K. Nikolics⁴⁹, K. Nikolopoulos¹⁸, P. Nilsson⁸, Y. Ninomiya¹⁵⁶, A. Nisati^{133a}, R. Nisius¹⁰⁰, T. Nobe¹⁵⁸, L. Nodulman⁶, M. Nomachi¹¹⁷, I. Nomidis¹⁵⁵, S. Norberg¹¹², M. Nordberg³⁰, J. Novakova¹²⁸, M. Nozaki⁶⁵, L. Nozka¹¹⁴, K. Ntekas¹⁰, A.-E. Nuncio-Quiroz²¹, G. Nunes Hanninger⁸⁷, T. Nunnemann⁹⁹, E. Nurse⁷⁷, B.J. O'Brien⁴⁶, F. O'grady⁷, D.C. O'Neil¹⁴³, V. O'Shea⁵³, L.B. Oakes⁹⁹, F.G. Oakham^{29,f}, H. Oberlack¹⁰⁰, J. Ocariz⁷⁹, A. Ochi⁶⁶, M.I. Ochoa⁷⁷, S. Oda⁶⁹, S. Odaka⁶⁵, H. Ogren⁶⁰, A. Oh⁸³, S.H. Oh⁴⁵, C.C. Ohm³⁰, T. Ohshima¹⁰², W. Okamura¹¹⁷, H. Okawa²⁵, Y. Okumura³¹, T. Okuyama¹⁵⁶, A. Olariu^{26a}, A.G. Olchevski⁶⁴, S.A. Olivares Pino⁴⁶, M. Oliveira^{125a,i}, D. Oliveira Damazio²⁵, E. Oliver Garcia¹⁶⁸, D. Olivito¹²¹, A. Olszewski³⁹, J. Olszowska³⁹, A. Onofre^{125a,af}, P.U.E. Onyisi^{31,ag}, C.J. Oram^{160a}, M.J. Oreglia³¹, Y. Oren¹⁵⁴, D. Orestano^{135a,135b}, N. Orlando^{72a,72b}, C. Oropeza Barrera⁵³, R.S. Orr¹⁵⁹, B. Osculati^{50a,50b}, R. Ospanov¹²¹, G. Otero y Garzon²⁷, H. Otono⁶⁹, M. Ouchrif^{136d}, E.A. Ouellette¹⁷⁰, F. Ould-Saada¹¹⁸, A. Ouraou¹³⁷, K.P. Oussoren¹⁰⁶, Q. Ouyang^{33a}, A. Ovcharova¹⁵, M. Owen⁸³, S. Owen¹⁴⁰, V.E. Ozcan^{19a}, N. Ozturk⁸, K. Pachal¹¹⁹, A. Pacheco Pages¹², C. Padilla Aranda¹², S. Pagan Griso¹⁵, E. Paganis¹⁴⁰, C. Pahl¹⁰⁰, F. Paige²⁵, P. Pais⁸⁵, K. Pajchel¹¹⁸, G. Palacino^{160b}, S. Palestini³⁰, D. Pallin³⁴, A. Palma^{125a}, J.D. Palmer¹⁸, Y.B. Pan¹⁷⁴, E. Panagiotopoulou¹⁰, J.G. Panduro Vazquez⁷⁶, P. Pani¹⁰⁶, N. Panikashvili⁸⁸, S. Panitkin²⁵, D. Pantea^{26a}, Th.D. Papadopoulou¹⁰, K. Papageorgiou^{155,q}, A. Paramonov⁶, D. Paredes Hernandez³⁴, M.A. Parker²⁸, F. Parodi^{50a,50b}, J.A. Parsons³⁵, U. Parzefall⁴⁸, S. Pashapour⁵⁴, E. Pasqualucci^{133a}, S. Passaggio^{50a}, A. Passeri^{135a}, F. Pastore^{135a,135b,*}, Fr. Pastore⁷⁶, G. Pásztor^{49,ah}, S. Pataraiia¹⁷⁶, N.D. Patel¹⁵¹, J.R. Pater⁸³, S. Patricelli^{103a,103b}, T. Pauly³⁰, J. Pearce¹⁷⁰, M. Pedersen¹¹⁸, S. Pedraza Lopez¹⁶⁸, S.V. Peleganchuk¹⁰⁸, D. Pelikan¹⁶⁷, H. Peng^{33b}, B. Penning³¹, J. Penwell⁶⁰, D.V. Perepelitsa³⁵, T. Perez Cavalcanti⁴², E. Perez Codina^{160a}, M.T. Pérez García-Estañ¹⁶⁸, V. Perez Reale³⁵, L. Perini^{90a,90b}, H. Pernegger³⁰, R. Perrino^{72a}, R. Peschke⁴², V.D. Peshekhonov⁶⁴, K. Peters³⁰, R.F.Y. Peters^{54,ai}, B.A. Petersen³⁰, J. Petersen³⁰, T.C. Petersen³⁶, E. Petit⁵, A. Petridis^{147a,147b}, C. Petridou¹⁵⁵, E. Petrolu^{133a}, F. Petrucci^{135a,135b}, M. Petteni¹⁴³, R. Pezoa^{32b}, P.W. Phillips¹³⁰, G. Piacquadio¹⁴⁴, E. Pianori¹⁷¹, A. Picazio⁴⁹, E. Piccaro⁷⁵, M. Piccinini^{20a,20b}, S.M. Piec⁴², R. Piegaiia²⁷, D.T. Pignotti¹¹⁰, J.E. Pilcher³¹, A.D. Pilkington⁷⁷, J. Pina^{125a,d}, M. Pinamonti^{165a,165c,aj}, A. Pinder¹¹⁹, J.L. Pinfold³, A. Pingel³⁶, B. Pinto^{125a}, C. Pizio^{90a,90b}, M.-A. Pleier²⁵, V. Pleskot¹²⁸, E. Plotnikova⁶⁴, P. Plucinski^{147a,147b}, S. Poddar^{58a}, F. Podlyski³⁴, R. Poettgen⁸², L. Poggioli¹¹⁶, D. Pohl²¹, M. Pohl⁴⁹, G. Polesello^{120a}, A. Policicchio^{37a,37b}, R. Polifka¹⁵⁹, A. Polini^{20a}, C.S. Pollard⁴⁵, V. Polychronakos²⁵, D. Pomeroy²³, K. Pommès³⁰, L. Pontecorvo^{133a}, B.G. Pope⁸⁹, G.A. Popeneciu^{26b}, D.S. Popovic^{13a},

A. Poppleton³⁰, X. Portell Bueso¹², G.E. Pospelov¹⁰⁰, S. Pospisil¹²⁷, K. Potamianos¹⁵,
 I.N. Potrap⁶⁴, C.J. Potter¹⁵⁰, C.T. Potter¹¹⁵, G. Poulard³⁰, J. Poveda⁶⁰, V. Pozdnyakov⁶⁴,
 R. Prabhu⁷⁷, P. Pralavorio⁸⁴, A. Pranko¹⁵, S. Prasad³⁰, R. Pravahan⁸, S. Prell⁶³,
 D. Price⁸³, J. Price⁷³, L.E. Price⁶, D. Prieur¹²⁴, M. Primavera^{72a}, M. Proissl⁴⁶,
 K. Prokofiev¹⁰⁹, F. Prokoshin^{32b}, E. Protopapadaki¹³⁷, S. Protopopescu²⁵, J. Proudfoot⁶,
 X. Prudent⁴⁴, M. Przybycien^{38a}, H. Przysiecki⁵, S. Psoroulas²¹, E. Ptacek¹¹⁵,
 E. Pueschel⁸⁵, D. Puldon¹⁴⁹, M. Purohit^{25,ak}, P. Puzo¹¹⁶, Y. Pylypchenko⁶², J. Qian⁸⁸,
 A. Quadt⁵⁴, D.R. Quarrie¹⁵, W.B. Quayle^{146c}, D. Quilty⁵³, V. Radeka²⁵, V. Radescu⁴²,
 S.K. Radhakrishnan¹⁴⁹, P. Radloff¹¹⁵, F. Ragusa^{90a,90b}, G. Rahal¹⁷⁹, S. Rajagopalan²⁵,
 M. Rammensee⁴⁸, M. Rammes¹⁴², A.S. Randle-Conde⁴⁰, C. Rangel-Smith⁷⁹, K. Rao¹⁶⁴,
 F. Rauscher⁹⁹, T.C. Rave⁴⁸, T. Ravenscroft⁵³, M. Raymond³⁰, A.L. Read¹¹⁸,
 D.M. Rebuffi^{120a,120b}, A. Redelbach¹⁷⁵, G. Redlinger²⁵, R. Reece¹³⁸, K. Reeves⁴¹,
 A. Reinsch¹¹⁵, H. Reisin²⁷, I. Reisinger⁴³, M. Relich¹⁶⁴, C. Rembser³⁰, Z.L. Ren¹⁵²,
 A. Renaud¹¹⁶, M. Rescigno^{133a}, S. Resconi^{90a}, B. Resende¹³⁷, P. Reznicek⁹⁹, R. Rezvani⁹⁴,
 R. Richter¹⁰⁰, E. Richter-Was^{38b}, M. Ridel⁷⁹, P. Rieck¹⁶, M. Rijssenbeek¹⁴⁹,
 A. Rimoldi^{120a,120b}, L. Rinaldi^{20a}, E. Ritsch⁶¹, I. Riu¹², G. Rivoltella^{90a,90b},
 F. Rizatdinova¹¹³, E. Rizvi⁷⁵, S.H. Robertson^{86,k}, A. Robichaud-Veronneau¹¹⁹,
 D. Robinson²⁸, J.E.M. Robinson⁸³, A. Robson⁵³, J.G. Rocha de Lima¹⁰⁷,
 C. Roda^{123a,123b}, D. Roda Dos Santos¹²⁶, L. Rodrigues³⁰, S. Roe³⁰, O. Røhne¹¹⁸,
 S. Rolli¹⁶², A. Romaniouk⁹⁷, M. Romano^{20a,20b}, G. Romeo²⁷, E. Romero Adam¹⁶⁸,
 N. Rompotis¹³⁹, L. Roos⁷⁹, E. Ros¹⁶⁸, S. Rosati^{133a}, K. Rosbach⁴⁹, A. Rose¹⁵⁰, M. Rose⁷⁶,
 P.L. Rosendahl¹⁴, O. Rosenthal¹⁴², V. Rossetti^{147a,147b}, E. Rossi^{103a,103b}, L.P. Rossi^{50a},
 R. Rosten¹³⁹, M. Rotaru^{26a}, I. Roth¹⁷³, J. Rothberg¹³⁹, D. Rousseau¹¹⁶, C.R. Royon¹³⁷,
 A. Rozanov⁸⁴, Y. Rozen¹⁵³, X. Ruan^{146c}, F. Rubbo¹², I. Rubinskiy⁴², V.I. Rud⁹⁸,
 C. Rudolph⁴⁴, M.S. Rudolph¹⁵⁹, F. Rühr⁷, A. Ruiz-Martinez⁶³, L. Rumyantsev⁶⁴,
 Z. Rurikova⁴⁸, N.A. Rusakovich⁶⁴, A. Ruschke⁹⁹, J.P. Rutherford⁷, N. Ruthmann⁴⁸,
 P. Ruzicka¹²⁶, Y.F. Ryabov¹²², M. Rybar¹²⁸, G. Rybkin¹¹⁶, N.C. Ryder¹¹⁹,
 A.F. Saavedra¹⁵¹, S. Sacerdoti²⁷, A. Saddique³, I. Sadeh¹⁵⁴, H.F-W. Sadrozinski¹³⁸,
 R. Sadykov⁶⁴, F. Safai Tehrani^{133a}, H. Sakamoto¹⁵⁶, Y. Sakurai¹⁷², G. Salamanna⁷⁵,
 A. Salamon^{134a}, M. Saleem¹¹², D. Salek¹⁰⁶, P.H. Sales De Bruin¹³⁹, D. Salihagic¹⁰⁰,
 A. Salnikov¹⁴⁴, J. Salt¹⁶⁸, B.M. Salvachua Ferrando⁶, D. Salvatore^{37a,37b}, F. Salvatore¹⁵⁰,
 A. Salvucci¹⁰⁵, A. Salzburger³⁰, D. Sampsonidis¹⁵⁵, A. Sanchez^{103a,103b}, J. Sánchez¹⁶⁸,
 V. Sanchez Martinez¹⁶⁸, H. Sandaker¹⁴, H.G. Sander⁸², M.P. Sanders⁹⁹, M. Sandhoff¹⁷⁶,
 T. Sandoval²⁸, C. Sandoval¹⁶³, R. Sandstroem¹⁰⁰, D.P.C. Sankey¹³⁰, A. Sansoni⁴⁷,
 C. Santoni³⁴, R. Santonico^{134a,134b}, H. Santos^{125a}, I. Santoyo Castillo¹⁵⁰, K. Sapp¹²⁴,
 A. Saproinov⁶⁴, J.G. Saraiva^{125a}, E. Sarkisyan-Grinbaum⁸, B. Sarrazin²¹, G. Sartisohn¹⁷⁶,
 O. Sasaki⁶⁵, Y. Sasaki¹⁵⁶, N. Sasao⁶⁷, I. Satsounkevitch⁹¹, G. Sauvage^{5,*}, E. Sauvan⁵,
 J.B. Sauvan¹¹⁶, P. Savard^{159,f}, V. Savinov¹²⁴, D.O. Savu³⁰, C. Sawyer¹¹⁹, L. Sawyer^{78,m},
 D.H. Saxon⁵³, J. Saxon¹²¹, C. Sbarra^{20a}, A. Sbrizzi³, T. Scanlon³⁰, D.A. Scannicchio¹⁶⁴,
 M. Scarcella¹⁵¹, J. Schaarschmidt¹⁷³, P. Schacht¹⁰⁰, D. Schaefer¹²¹, A. Schaelicke⁴⁶,
 S. Schaepe²¹, S. Schaetzel^{58b}, U. Schäfer⁸², A.C. Schaffer¹¹⁶, D. Schaile⁹⁹,
 R.D. Schamberger¹⁴⁹, V. Scharif^{58a}, V.A. Schegelsky¹²², D. Scheirich⁸⁸, M. Schernau¹⁶⁴,
 M.I. Scherzer³⁵, C. Schiavi^{50a,50b}, J. Schieck⁹⁹, C. Schillo⁴⁸, M. Schioppa^{37a,37b},

S. Schlenker³⁰, E. Schmidt⁴⁸, K. Schmieden³⁰, C. Schmitt⁸², C. Schmitt⁹⁹, S. Schmitt^{58b},
 B. Schneider¹⁷, Y.J. Schnellbach⁷³, U. Schnoor⁴⁴, L. Schoeffel¹³⁷, A. Schoening^{58b},
 B.D. Schoenrock⁸⁹, A.L.S. Schorlemmer⁵⁴, M. Schott⁸², D. Schouten^{160a},
 J. Schovancova²⁵, M. Schram⁸⁶, S. Schramm¹⁵⁹, M. Schreyer¹⁷⁵, C. Schroeder⁸²,
 N. Schroer^{58c}, N. Schuh⁸², M.J. Schultens²¹, H.-C. Schultz-Coulon^{58a}, H. Schulz¹⁶,
 M. Schumacher⁴⁸, B.A. Schumm¹³⁸, Ph. Schune¹³⁷, A. Schwartzman¹⁴⁴, Ph. Schwegler¹⁰⁰,
 Ph. Schwemling¹³⁷, R. Schwienhorst⁸⁹, J. Schwindling¹³⁷, T. Schwindt²¹, M. Schwoerer⁵,
 F.G. Sciacca¹⁷, E. Scifo¹¹⁶, G. Sciolla²³, W.G. Scott¹³⁰, F. Scutti²¹, J. Searcy⁸⁸,
 G. Sedov⁴², E. Sedykh¹²², S.C. Seidel¹⁰⁴, A. Seiden¹³⁸, F. Seifert¹²⁷, J.M. Seixas^{24a},
 G. Sekhniaidze^{103a}, S.J. Sekula⁴⁰, K.E. Selbach⁴⁶, D.M. Seliverstov¹²², G. Sellers⁷³,
 M. Seman^{145b}, N. Semprini-Cesari^{20a,20b}, C. Serfon³⁰, L. Serin¹¹⁶, L. Serkin⁵⁴, T. Serre⁸⁴,
 R. Seuster^{160a}, H. Severini¹¹², F. Sforza¹⁰⁰, A. Sfyrla³⁰, E. Shabalina⁵⁴, M. Shamim¹¹⁵,
 L.Y. Shan^{33a}, J.T. Shank²², Q.T. Shao⁸⁷, M. Shapiro¹⁵, P.B. Shatalov⁹⁶, K. Shaw^{165a,165c},
 P. Sherwood⁷⁷, S. Shimizu⁶⁶, M. Shimojima¹⁰¹, T. Shin⁵⁶, M. Shiyakova⁶⁴, A. Shmeleva⁹⁵,
 M.J. Shochet³¹, D. Short¹¹⁹, S. Shrestha⁶³, E. Shulga⁹⁷, M.A. Shupe⁷, S. Shushkevich⁴²,
 P. Sicho¹²⁶, D. Sidorov¹¹³, A. Sidoti^{133a}, F. Siegert⁴⁸, Dj. Sijacki^{13a}, O. Silbert¹⁷³,
 J. Silva^{125a}, Y. Silver¹⁵⁴, D. Silverstein¹⁴⁴, S.B. Silverstein^{147a}, V. Simak¹²⁷, O. Simard⁵,
 Lj. Simic^{13a}, S. Simion¹¹⁶, E. Simioni⁸², B. Simmons⁷⁷, R. Simoniello^{90a,90b},
 M. Simonyan³⁶, P. Sinervo¹⁵⁹, N.B. Sinev¹¹⁵, V. Sipica¹⁴², G. Siragusa¹⁷⁵, A. Sircar⁷⁸,
 A.N. Sisakyan^{64,*}, S.Yu. Sivoklokov⁹⁸, J. Sjölin^{147a,147b}, T.B. Sjursen¹⁴, L.A. Skinnari¹⁵,
 H.P. Skottowe⁵⁷, K.Yu. Skovpen¹⁰⁸, P. Skubic¹¹², M. Slater¹⁸, T. Slavicek¹²⁷, K. Sliwa¹⁶²,
 V. Smakhtin¹⁷³, B.H. Smart⁴⁶, L. Smestad¹¹⁸, S.Yu. Smirnov⁹⁷, Y. Smirnov⁹⁷,
 L.N. Smirnova^{98,al}, O. Smirnova⁸⁰, K.M. Smith⁵³, M. Smizanska⁷¹, K. Smolek¹²⁷,
 A.A. Snesarev⁹⁵, G. Snidero⁷⁵, J. Snow¹¹², S. Snyder²⁵, R. Sobie^{170,k}, F. Socher⁴⁴,
 J. Sodomka¹²⁷, A. Soffer¹⁵⁴, D.A. Soh^{152,x}, C.A. Solans³⁰, M. Solar¹²⁷, J. Solc¹²⁷,
 E.Yu. Soldatov⁹⁷, U. Soldevila¹⁶⁸, E. Solfaroli Camillocci^{133a,133b}, A.A. Solodkov¹²⁹,
 O.V. Solovyanov¹²⁹, V. Solovyev¹²², N. Soni¹, A. Sood¹⁵, V. Sopko¹²⁷, B. Sopko¹²⁷,
 M. Sosebee⁸, R. Soualah^{165a,165c}, P. Soueid⁹⁴, A.M. Soukharev¹⁰⁸, D. South⁴²,
 S. Spagnolo^{72a,72b}, F. Spanò⁷⁶, W.R. Spearman⁵⁷, R. Spighi^{20a}, G. Spigo³⁰,
 M. Spousta^{128,am}, T. Spreitzer¹⁵⁹, B. Spurlock⁸, R.D. St. Denis⁵³, J. Stahlman¹²¹,
 R. Stamen^{58a}, E. Stanecka³⁹, R.W. Stanek⁶, C. Stanescu^{135a}, M. Stanescu-Bellu⁴²,
 M.M. Stanitzki⁴², S. Stapnes¹¹⁸, E.A. Starchenko¹²⁹, J. Stark⁵⁵, P. Staroba¹²⁶,
 P. Starovoitov⁴², R. Staszewski³⁹, P. Stavina^{145a,*}, G. Steele⁵³, P. Steinbach⁴⁴,
 P. Steinberg²⁵, I. Stekl¹²⁷, B. Stelzer¹⁴³, H.J. Stelzer⁸⁹, O. Stelzer-Chilton^{160a},
 H. Stenzel⁵², S. Stern¹⁰⁰, G.A. Stewart³⁰, J.A. Stillings²¹, M.C. Stockton⁸⁶, M. Stoebe⁸⁶,
 K. Stoerig⁴⁸, G. Stoicea^{26a}, S. Stonjek¹⁰⁰, A.R. Stradling⁸, A. Straessner⁴⁴,
 J. Strandberg¹⁴⁸, S. Strandberg^{147a,147b}, A. Strandlie¹¹⁸, E. Strauss¹⁴⁴, M. Strauss¹¹²,
 P. Striznec^{145b}, R. Ströhmer¹⁷⁵, D.M. Strom¹¹⁵, R. Stroynowski⁴⁰, S.A. Stucci¹⁷,
 B. Stugu¹⁴, I. Stumer^{25,*}, J. Stupak¹⁴⁹, P. Sturm¹⁷⁶, N.A. Styles⁴², D. Su¹⁴⁴, J. Su¹²⁴,
 HS. Subramania³, R. Subramaniam⁷⁸, A. Succurro¹², Y. Sugaya¹¹⁷, C. Suhr¹⁰⁷,
 M. Suk¹²⁷, V.V. Sulin⁹⁵, S. Sultansoy^{4c}, T. Sumida⁶⁷, X. Sun⁵⁵, J.E. Sundermann⁴⁸,
 K. Suruliz¹⁴⁰, G. Susinno^{37a,37b}, M.R. Sutton¹⁵⁰, Y. Suzuki⁶⁵, M. Svatos¹²⁶, S. Swedish¹⁶⁹,
 M. Swiatlowski¹⁴⁴, I. Sykora^{145a}, T. Sykora¹²⁸, D. Ta⁸⁹, K. Tackmann⁴², J. Taenzer¹⁵⁹,

A. Taffard¹⁶⁴, R. Tafirout^{160a}, N. Taiblum¹⁵⁴, Y. Takahashi¹⁰², H. Takai²⁵,
 R. Takashima⁶⁸, H. Takeda⁶⁶, T. Takeshita¹⁴¹, Y. Takubo⁶⁵, M. Talby⁸⁴,
 A.A. Talyshev^{108,h}, J.Y.C. Tam¹⁷⁵, M.C. Tamsett^{78,an}, K.G. Tan⁸⁷, J. Tanaka¹⁵⁶,
 R. Tanaka¹¹⁶, S. Tanaka¹³², S. Tanaka⁶⁵, A.J. Tanasijczuk¹⁴³, K. Tani⁶⁶, N. Tannoury⁸⁴,
 S. Tapprogge⁸², S. Tarem¹⁵³, F. Tarrade²⁹, G.F. Tartarelli^{90a}, P. Tas¹²⁸, M. Tasevsky¹²⁶,
 T. Tashiro⁶⁷, E. Tassi^{37a,37b}, A. Tavares Delgado^{125a}, Y. Tayalati^{136d}, C. Taylor⁷⁷,
 F.E. Taylor⁹³, G.N. Taylor⁸⁷, W. Taylor^{160b}, F.A. Teischinger³⁰,
 M. Teixeira Dias Castanheira⁷⁵, P. Teixeira-Dias⁷⁶, K.K. Temming⁴⁸, H. Ten Kate³⁰,
 P.K. Teng¹⁵², S. Terada⁶⁵, K. Terashi¹⁵⁶, J. Terron⁸¹, S. Terzo¹⁰⁰, M. Testa⁴⁷,
 R.J. Teuscher^{159,k}, J. Therhaag²¹, T. Thevenaux-Pelzer³⁴, S. Thoma⁴⁸, J.P. Thomas¹⁸,
 E.N. Thompson³⁵, P.D. Thompson¹⁸, P.D. Thompson¹⁵⁹, A.S. Thompson⁵³,
 L.A. Thomsen³⁶, E. Thomson¹²¹, M. Thomson²⁸, W.M. Thong⁸⁷, R.P. Thun^{88,*},
 F. Tian³⁵, M.J. Tibbetts¹⁵, T. Tic¹²⁶, V.O. Tikhomirov^{95,ao}, Yu.A. Tikhonov^{108,h},
 S. Timoshenko⁹⁷, E. Tiouchichine⁸⁴, P. Tipton¹⁷⁷, S. Tisserant⁸⁴, T. Todorov⁵,
 S. Todorova-Nova¹²⁸, B. Toggerson¹⁶⁴, J. Tojo⁶⁹, S. Tokár^{145a}, K. Tokushuku⁶⁵,
 K. Tollefson⁸⁹, L. Tomlinson⁸³, M. Tomoto¹⁰², L. Tompkins³¹, K. Toms¹⁰⁴,
 N.D. Topilin⁶⁴, E. Torrence¹¹⁵, H. Torres¹⁴³, E. Torró Pastor¹⁶⁸, J. Toth^{84,ah},
 F. Touchard⁸⁴, D.R. Tovey¹⁴⁰, H.L. Tran¹¹⁶, T. Trefzger¹⁷⁵, L. Tremblet³⁰, A. Tricoli³⁰,
 I.M. Trigger^{160a}, S. Trincaz-Duvoid⁷⁹, M.F. Tripiana⁷⁰, N. Triplett²⁵, W. Trischuk¹⁵⁹,
 B. Trocmé⁵⁵, C. Troncon^{90a}, M. Trottier-McDonald¹⁴³, M. Trovatelli^{135a,135b}, P. True⁸⁹,
 M. Trzebinski³⁹, A. Trzupek³⁹, C. Tsarouchas³⁰, J.C-L. Tseng¹¹⁹, P.V. Tsiareshka⁹¹,
 D. Tsionou¹³⁷, G. Tsipolitis¹⁰, N. Tsirintanis⁹, S. Tsiskaridze¹², V. Tsiskaridze⁴⁸,
 E.G. Tskhadadze^{51a}, I.I. Tsukerman⁹⁶, V. Tsulaia¹⁵, J.-W. Tsung²¹, S. Tsuno⁶⁵,
 D. Tsybychev¹⁴⁹, A. Tua¹⁴⁰, A. Tudorache^{26a}, V. Tudorache^{26a}, J.M. Tuggle³¹,
 A.N. Tuna¹²¹, S.A. Tupputi^{20a,20b}, S. Turchikhin^{98,al}, D. Turecek¹²⁷, I. Turk Cakir^{4d},
 R. Turra^{90a,90b}, P.M. Tuts³⁵, A. Tykhonov⁷⁴, M. Tylmad^{147a,147b}, M. Tyndel¹³⁰,
 K. Uchida²¹, I. Ueda¹⁵⁶, R. Ueno²⁹, M. Ughetto⁸⁴, M. Ugland¹⁴, M. Uhlenbrock²¹,
 F. Ukegawa¹⁶¹, G. Unal³⁰, A. Undrus²⁵, G. Unel¹⁶⁴, F.C. Ungaro⁴⁸, Y. Unno⁶⁵,
 D. Urbaniec³⁵, P. Urquijo²¹, G. Usai⁸, A. Usanova⁶¹, L. Vacavant⁸⁴, V. Vacek¹²⁷,
 B. Vachon⁸⁶, N. Valencic¹⁰⁶, S. Valentineti^{20a,20b}, A. Valero¹⁶⁸, L. Valery³⁴, S. Valkar¹²⁸,
 E. Valladolid Gallego¹⁶⁸, S. Vallecorsa⁴⁹, J.A. Valls Ferrer¹⁶⁸, R. Van Berg¹²¹,
 P.C. Van Der Deijl¹⁰⁶, R. van der Geer¹⁰⁶, H. van der Graaf¹⁰⁶, R. Van Der Leeuw¹⁰⁶,
 D. van der Ster³⁰, N. van Eldik³⁰, P. van Gemmeren⁶, J. Van Nieuwkoop¹⁴³,
 I. van Vulpen¹⁰⁶, M.C. van Woerden³⁰, M. Vanadia¹⁰⁰, W. Vandelli³⁰, A. Vaniachine⁶,
 P. Vankov⁴², F. Vannucci⁷⁹, G. Vardanyan¹⁷⁸, R. Vari^{133a}, E.W. Varnes⁷, T. Varol⁸⁵,
 D. Varouchas¹⁵, A. Vartapetian⁸, K.E. Varvell¹⁵¹, V.I. Vassilakopoulos⁵⁶, F. Vazeille³⁴,
 T. Vazquez Schroeder⁵⁴, J. Veatch⁷, F. Veloso^{125a}, S. Veneziano^{133a}, A. Ventura^{72a,72b},
 D. Ventura⁸⁵, M. Venturi⁴⁸, N. Venturi¹⁵⁹, A. Venturini²³, V. Vercesi^{120a}, M. Verducci¹³⁹,
 W. Verkerke¹⁰⁶, J.C. Vermeulen¹⁰⁶, A. Vest⁴⁴, M.C. Vetterli^{143,f}, O. Viazlo⁸⁰,
 I. Vichou¹⁶⁶, T. Vickey^{146c,ap}, O.E. Vickey Boeriu^{146c}, G.H.A. Viehhauser¹¹⁹, S. Viel¹⁶⁹,
 R. Vigne³⁰, M. Villa^{20a,20b}, M. Villaplana Perez¹⁶⁸, E. Vilucchi⁴⁷, M.G. Vincter²⁹,
 V.B. Vinogradov⁶⁴, J. Virzi¹⁵, O. Vitells¹⁷³, M. Viti⁴², I. Vivarelli¹⁵⁰, F. Vives Vaque³,
 S. Vlachos¹⁰, D. Vladioiu⁹⁹, M. Vlasak¹²⁷, A. Vogel²¹, P. Vokac¹²⁷, G. Volpi⁴⁷, M. Volpi⁸⁷,

G. Volpini^{90a}, H. von der Schmitt¹⁰⁰, H. von Radziewski⁴⁸, E. von Toerne²¹,
V. Vorobel¹²⁸, M. Vos¹⁶⁸, R. Voss³⁰, J.H. Vosseveld⁷³, N. Vranjes¹³⁷,
M. Vranjes Milosavljevic¹⁰⁶, V. Vrba¹²⁶, M. Vreeswijk¹⁰⁶, T. Vu Anh⁴⁸, R. Vuillermet³⁰,
I. Vukotic³¹, Z. Vykydal¹²⁷, W. Wagner¹⁷⁶, P. Wagner²¹, S. Wahrmund⁴⁴,
J. Wakabayashi¹⁰², S. Walch⁸⁸, J. Walder⁷¹, R. Walker⁹⁹, W. Walkowiak¹⁴², R. Wall¹⁷⁷,
P. Waller⁷³, B. Walsh¹⁷⁷, C. Wang⁴⁵, H. Wang¹⁵, H. Wang⁴⁰, J. Wang¹⁵², J. Wang^{33a},
K. Wang⁸⁶, R. Wang¹⁰⁴, S.M. Wang¹⁵², T. Wang²¹, X. Wang¹⁷⁷, A. Warburton⁸⁶,
C.P. Ward²⁸, D.R. Wardrope⁷⁷, M. Warsinsky⁴⁸, A. Washbrook⁴⁶, C. Wasicki⁴²,
I. Watanabe⁶⁶, P.M. Watkins¹⁸, A.T. Watson¹⁸, I.J. Watson¹⁵¹, M.F. Watson¹⁸,
G. Watts¹³⁹, S. Watts⁸³, A.T. Waugh¹⁵¹, B.M. Waugh⁷⁷, S. Webb⁸³, M.S. Weber¹⁷,
S.W. Weber¹⁷⁵, J.S. Webster³¹, A.R. Weidberg¹¹⁹, P. Weigell¹⁰⁰, J. Weingarten⁵⁴,
C. Weiser⁴⁸, H. Weits¹⁰⁶, P.S. Wells³⁰, T. Wenaus²⁵, D. Wendland¹⁶, Z. Weng^{152,x},
T. Wengler³⁰, S. Wenig³⁰, N. Wermes²¹, M. Werner⁴⁸, P. Werner³⁰, M. Wessels^{58a},
J. Wetter¹⁶², K. Whalen²⁹, A. White⁸, M.J. White¹, R. White^{32b}, S. White^{123a,123b},
D. Whiteson¹⁶⁴, D. Whittington⁶⁰, D. Wicke¹⁷⁶, F.J. Wickens¹³⁰, W. Wiedenmann¹⁷⁴,
M. Wielers^{80,e}, P. Wienemann²¹, C. Wiglesworth³⁶, L.A.M. Wiik-Fuchs²¹,
P.A. Wijeratne⁷⁷, A. Wildauer¹⁰⁰, M.A. Wildt^{42,aq}, I. Wilhelm¹²⁸, H.G. Wilkens³⁰,
J.Z. Will⁹⁹, H.H. Williams¹²¹, S. Williams²⁸, W. Willis^{35,*}, S. Willocq⁸⁵, J.A. Wilson¹⁸,
A. Wilson⁸⁸, I. Wingerter-Seez⁵, S. Winkelmann⁴⁸, F. Winklmeier¹¹⁵, M. Wittgen¹⁴⁴,
T. Wittig⁴³, J. Wittkowski⁹⁹, S.J. Wollstadt⁸², M.W. Wolter³⁹, H. Wolters^{125a,i},
W.C. Wong⁴¹, B.K. Wosiek³⁹, J. Wotschack³⁰, M.J. Woudstra⁸³, K.W. Wozniak³⁹,
K. Wraight⁵³, M. Wright⁵³, S.L. Wu¹⁷⁴, X. Wu⁴⁹, Y. Wu⁸⁸, E. Wulf³⁵, T.R. Wyatt⁸³,
B.M. Wynne⁴⁶, S. Xella³⁶, M. Xiao¹³⁷, C. Xu^{33b,ac}, D. Xu^{33a}, L. Xu^{33b,ar}, B. Yabsley¹⁵¹,
S. Yacoub^{146b,as}, M. Yamada⁶⁵, H. Yamaguchi¹⁵⁶, Y. Yamaguchi¹⁵⁶, A. Yamamoto⁶⁵,
K. Yamamoto⁶³, S. Yamamoto¹⁵⁶, T. Yamamura¹⁵⁶, T. Yamanaka¹⁵⁶, K. Yamauchi¹⁰²,
Y. Yamazaki⁶⁶, Z. Yan²², H. Yang^{33e}, H. Yang¹⁷⁴, U.K. Yang⁸³, Y. Yang¹¹⁰, S. Yanush⁹²,
L. Yao^{33a}, Y. Yasu⁶⁵, E. Yatsenko⁴², K.H. Yau Wong²¹, J. Ye⁴⁰, S. Ye²⁵, A.L. Yen⁵⁷,
E. Yildirim⁴², M. Yilmaz^{4b}, R. Yoosofmiya¹²⁴, K. Yorita¹⁷², R. Yoshida⁶,
K. Yoshihara¹⁵⁶, C. Young¹⁴⁴, C.J.S. Young¹¹⁹, S. Youssef²², D.R. Yu¹⁵, J. Yu⁸, J. Yu¹¹³,
L. Yuan⁶⁶, A. Yurkewicz¹⁰⁷, B. Zabinski³⁹, R. Zaidan⁶², A.M. Zaitsev^{129,ad}, A. Zaman¹⁴⁹,
S. Zambito²³, L. Zanello^{133a,133b}, D. Zanzi¹⁰⁰, A. Zaytsev²⁵, C. Zeitnitz¹⁷⁶, M. Zeman¹²⁷,
A. Zemla³⁹, K. Zengel²³, O. Zenin¹²⁹, T. Ženiš^{145a}, D. Zerwas¹¹⁶, G. Zevi della Porta⁵⁷,
D. Zhang⁸⁸, H. Zhang⁸⁹, J. Zhang⁶, L. Zhang¹⁵², X. Zhang^{33d}, Z. Zhang¹¹⁶, Z. Zhao^{33b},
A. Zhemchugov⁶⁴, J. Zhong¹¹⁹, B. Zhou⁸⁸, L. Zhou³⁵, N. Zhou¹⁶⁴, C.G. Zhu^{33d}, H. Zhu^{33a},
J. Zhu⁸⁸, Y. Zhu^{33b}, X. Zhuang^{33a}, A. Zibell⁹⁹, D. Zieminska⁶⁰, N.I. Zimin⁶⁴,
C. Zimmermann⁸², R. Zimmermann²¹, S. Zimmermann²¹, S. Zimmermann⁴⁸,
Z. Zinonos⁵⁴, M. Ziolkowski¹⁴², R. Zitoun⁵, L. Živković³⁵, G. Zobernig¹⁷⁴,
A. Zoccoli^{20a,20b}, M. zur Nedden¹⁶, G. Zurzolo^{103a,103b}, V. Zutshi¹⁰⁷, L. Zwalinski³⁰.

¹ School of Chemistry and Physics, University of Adelaide, Adelaide, Australia

² Physics Department, SUNY Albany, Albany NY, United States of America

³ Department of Physics, University of Alberta, Edmonton AB, Canada

⁴ (a) Department of Physics, Ankara University, Ankara; (b) Department of Physics, Gazi

- University, Ankara; ^(c) Division of Physics, TOBB University of Economics and Technology, Ankara; ^(d) Turkish Atomic Energy Authority, Ankara, Turkey
- ⁵ LAPP, CNRS/IN2P3 and Université de Savoie, Annecy-le-Vieux, France
- ⁶ High Energy Physics Division, Argonne National Laboratory, Argonne IL, United States of America
- ⁷ Department of Physics, University of Arizona, Tucson AZ, United States of America
- ⁸ Department of Physics, The University of Texas at Arlington, Arlington TX, United States of America
- ⁹ Physics Department, University of Athens, Athens, Greece
- ¹⁰ Physics Department, National Technical University of Athens, Zografou, Greece
- ¹¹ Institute of Physics, Azerbaijan Academy of Sciences, Baku, Azerbaijan
- ¹² Institut de Física d'Altes Energies and Departament de Física de la Universitat Autònoma de Barcelona, Barcelona, Spain
- ¹³ ^(a) Institute of Physics, University of Belgrade, Belgrade; ^(b) Vinca Institute of Nuclear Sciences, University of Belgrade, Belgrade, Serbia
- ¹⁴ Department for Physics and Technology, University of Bergen, Bergen, Norway
- ¹⁵ Physics Division, Lawrence Berkeley National Laboratory and University of California, Berkeley CA, United States of America
- ¹⁶ Department of Physics, Humboldt University, Berlin, Germany
- ¹⁷ Albert Einstein Center for Fundamental Physics and Laboratory for High Energy Physics, University of Bern, Bern, Switzerland
- ¹⁸ School of Physics and Astronomy, University of Birmingham, Birmingham, United Kingdom
- ¹⁹ ^(a) Department of Physics, Bogazici University, Istanbul; ^(b) Department of Physics, Dogus University, Istanbul; ^(c) Department of Physics Engineering, Gaziantep University, Gaziantep, Turkey
- ²⁰ ^(a) INFN Sezione di Bologna; ^(b) Dipartimento di Fisica e Astronomia, Università di Bologna, Bologna, Italy
- ²¹ Physikalisches Institut, University of Bonn, Bonn, Germany
- ²² Department of Physics, Boston University, Boston MA, United States of America
- ²³ Department of Physics, Brandeis University, Waltham MA, United States of America
- ²⁴ ^(a) Universidade Federal do Rio De Janeiro COPPE/EE/IF, Rio de Janeiro; ^(b) Federal University of Juiz de Fora (UFJF), Juiz de Fora; ^(c) Federal University of Sao Joao del Rei (UFSJ), Sao Joao del Rei; ^(d) Instituto de Fisica, Universidade de Sao Paulo, Sao Paulo, Brazil
- ²⁵ Physics Department, Brookhaven National Laboratory, Upton NY, United States of America
- ²⁶ ^(a) National Institute of Physics and Nuclear Engineering, Bucharest; ^(b) National Institute for Research and Development of Isotopic and Molecular Technologies, Physics Department, Cluj Napoca; ^(c) University Politehnica Bucharest, Bucharest; ^(d) West University in Timisoara, Timisoara, Romania
- ²⁷ Departamento de Física, Universidad de Buenos Aires, Buenos Aires, Argentina
- ²⁸ Cavendish Laboratory, University of Cambridge, Cambridge, United Kingdom

- ²⁹ Department of Physics, Carleton University, Ottawa ON, Canada
- ³⁰ CERN, Geneva, Switzerland
- ³¹ Enrico Fermi Institute, University of Chicago, Chicago IL, United States of America
- ³² ^(a) Departamento de Física, Pontificia Universidad Católica de Chile, Santiago; ^(b) Departamento de Física, Universidad Técnica Federico Santa María, Valparaíso, Chile
- ³³ ^(a) Institute of High Energy Physics, Chinese Academy of Sciences, Beijing; ^(b) Department of Modern Physics, University of Science and Technology of China, Anhui; ^(c) Department of Physics, Nanjing University, Jiangsu; ^(d) School of Physics, Shandong University, Shandong; ^(e) Physics Department, Shanghai Jiao Tong University, Shanghai, China
- ³⁴ Laboratoire de Physique Corpusculaire, Clermont Université and Université Blaise Pascal and CNRS/IN2P3, Clermont-Ferrand, France
- ³⁵ Nevis Laboratory, Columbia University, Irvington NY, United States of America
- ³⁶ Niels Bohr Institute, University of Copenhagen, Kobenhavn, Denmark
- ³⁷ ^(a) INFN Gruppo Collegato di Cosenza; ^(b) Dipartimento di Fisica, Università della Calabria, Rende, Italy
- ³⁸ ^(a) AGH University of Science and Technology, Faculty of Physics and Applied Computer Science, Krakow; ^(b) Marian Smoluchowski Institute of Physics, Jagiellonian University, Krakow, Poland
- ³⁹ The Henryk Niewodniczanski Institute of Nuclear Physics, Polish Academy of Sciences, Krakow, Poland
- ⁴⁰ Physics Department, Southern Methodist University, Dallas TX, United States of America
- ⁴¹ Physics Department, University of Texas at Dallas, Richardson TX, United States of America
- ⁴² DESY, Hamburg and Zeuthen, Germany
- ⁴³ Institut für Experimentelle Physik IV, Technische Universität Dortmund, Dortmund, Germany
- ⁴⁴ Institut für Kern- und Teilchenphysik, Technische Universität Dresden, Dresden, Germany
- ⁴⁵ Department of Physics, Duke University, Durham NC, United States of America
- ⁴⁶ SUPA - School of Physics and Astronomy, University of Edinburgh, Edinburgh, United Kingdom
- ⁴⁷ INFN Laboratori Nazionali di Frascati, Frascati, Italy
- ⁴⁸ Fakultät für Mathematik und Physik, Albert-Ludwigs-Universität, Freiburg, Germany
- ⁴⁹ Section de Physique, Université de Genève, Geneva, Switzerland
- ⁵⁰ ^(a) INFN Sezione di Genova; ^(b) Dipartimento di Fisica, Università di Genova, Genova, Italy
- ⁵¹ ^(a) E. Andronikashvili Institute of Physics, Iv. Javakhishvili Tbilisi State University, Tbilisi; ^(b) High Energy Physics Institute, Tbilisi State University, Tbilisi, Georgia
- ⁵² II Physikalisches Institut, Justus-Liebig-Universität Giessen, Giessen, Germany
- ⁵³ SUPA - School of Physics and Astronomy, University of Glasgow, Glasgow, United Kingdom

- ⁵⁴ II Physikalisches Institut, Georg-August-Universität, Göttingen, Germany
- ⁵⁵ Laboratoire de Physique Subatomique et de Cosmologie, Université Joseph Fourier and CNRS/IN2P3 and Institut National Polytechnique de Grenoble, Grenoble, France
- ⁵⁶ Department of Physics, Hampton University, Hampton VA, United States of America
- ⁵⁷ Laboratory for Particle Physics and Cosmology, Harvard University, Cambridge MA, United States of America
- ⁵⁸ ^(a) Kirchhoff-Institut für Physik, Ruprecht-Karls-Universität Heidelberg, Heidelberg; ^(b) Physikalisches Institut, Ruprecht-Karls-Universität Heidelberg, Heidelberg; ^(c) ZITI Institut für technische Informatik, Ruprecht-Karls-Universität Heidelberg, Mannheim, Germany
- ⁵⁹ Faculty of Applied Information Science, Hiroshima Institute of Technology, Hiroshima, Japan
- ⁶⁰ Department of Physics, Indiana University, Bloomington IN, United States of America
- ⁶¹ Institut für Astro- und Teilchenphysik, Leopold-Franzens-Universität, Innsbruck, Austria
- ⁶² University of Iowa, Iowa City IA, United States of America
- ⁶³ Department of Physics and Astronomy, Iowa State University, Ames IA, United States of America
- ⁶⁴ Joint Institute for Nuclear Research, JINR Dubna, Dubna, Russia
- ⁶⁵ KEK, High Energy Accelerator Research Organization, Tsukuba, Japan
- ⁶⁶ Graduate School of Science, Kobe University, Kobe, Japan
- ⁶⁷ Faculty of Science, Kyoto University, Kyoto, Japan
- ⁶⁸ Kyoto University of Education, Kyoto, Japan
- ⁶⁹ Department of Physics, Kyushu University, Fukuoka, Japan
- ⁷⁰ Instituto de Física La Plata, Universidad Nacional de La Plata and CONICET, La Plata, Argentina
- ⁷¹ Physics Department, Lancaster University, Lancaster, United Kingdom
- ⁷² ^(a) INFN Sezione di Lecce; ^(b) Dipartimento di Matematica e Fisica, Università del Salento, Lecce, Italy
- ⁷³ Oliver Lodge Laboratory, University of Liverpool, Liverpool, United Kingdom
- ⁷⁴ Department of Physics, Jožef Stefan Institute and University of Ljubljana, Ljubljana, Slovenia
- ⁷⁵ School of Physics and Astronomy, Queen Mary University of London, London, United Kingdom
- ⁷⁶ Department of Physics, Royal Holloway University of London, Surrey, United Kingdom
- ⁷⁷ Department of Physics and Astronomy, University College London, London, United Kingdom
- ⁷⁸ Louisiana Tech University, Ruston LA, United States of America
- ⁷⁹ Laboratoire de Physique Nucléaire et de Hautes Energies, UPMC and Université Paris-Diderot and CNRS/IN2P3, Paris, France
- ⁸⁰ Fysiska institutionen, Lunds universitet, Lund, Sweden
- ⁸¹ Departamento de Física Teórica C-15, Universidad Autónoma de Madrid, Madrid, Spain

- ⁸² Institut für Physik, Universität Mainz, Mainz, Germany
- ⁸³ School of Physics and Astronomy, University of Manchester, Manchester, United Kingdom
- ⁸⁴ CPPM, Aix-Marseille Université and CNRS/IN2P3, Marseille, France
- ⁸⁵ Department of Physics, University of Massachusetts, Amherst MA, United States of America
- ⁸⁶ Department of Physics, McGill University, Montreal QC, Canada
- ⁸⁷ School of Physics, University of Melbourne, Victoria, Australia
- ⁸⁸ Department of Physics, The University of Michigan, Ann Arbor MI, United States of America
- ⁸⁹ Department of Physics and Astronomy, Michigan State University, East Lansing MI, United States of America
- ⁹⁰ *(a)* INFN Sezione di Milano; *(b)* Dipartimento di Fisica, Università di Milano, Milano, Italy
- ⁹¹ B.I. Stepanov Institute of Physics, National Academy of Sciences of Belarus, Minsk, Republic of Belarus
- ⁹² National Scientific and Educational Centre for Particle and High Energy Physics, Minsk, Republic of Belarus
- ⁹³ Department of Physics, Massachusetts Institute of Technology, Cambridge MA, United States of America
- ⁹⁴ Group of Particle Physics, University of Montreal, Montreal QC, Canada
- ⁹⁵ P.N. Lebedev Institute of Physics, Academy of Sciences, Moscow, Russia
- ⁹⁶ Institute for Theoretical and Experimental Physics (ITEP), Moscow, Russia
- ⁹⁷ Moscow Engineering and Physics Institute (MEPhI), Moscow, Russia
- ⁹⁸ D.V.Skobel'tsyn Institute of Nuclear Physics, M.V.Lomonosov Moscow State University, Moscow, Russia
- ⁹⁹ Fakultät für Physik, Ludwig-Maximilians-Universität München, München, Germany
- ¹⁰⁰ Max-Planck-Institut für Physik (Werner-Heisenberg-Institut), München, Germany
- ¹⁰¹ Nagasaki Institute of Applied Science, Nagasaki, Japan
- ¹⁰² Graduate School of Science and Kobayashi-Maskawa Institute, Nagoya University, Nagoya, Japan
- ¹⁰³ *(a)* INFN Sezione di Napoli; *(b)* Dipartimento di Scienze Fisiche, Università di Napoli, Napoli, Italy
- ¹⁰⁴ Department of Physics and Astronomy, University of New Mexico, Albuquerque NM, United States of America
- ¹⁰⁵ Institute for Mathematics, Astrophysics and Particle Physics, Radboud University Nijmegen/Nikhef, Nijmegen, Netherlands
- ¹⁰⁶ Nikhef National Institute for Subatomic Physics and University of Amsterdam, Amsterdam, Netherlands
- ¹⁰⁷ Department of Physics, Northern Illinois University, DeKalb IL, United States of America
- ¹⁰⁸ Budker Institute of Nuclear Physics, SB RAS, Novosibirsk, Russia
- ¹⁰⁹ Department of Physics, New York University, New York NY, United States of America

- 110 Ohio State University, Columbus OH, United States of America
- 111 Faculty of Science, Okayama University, Okayama, Japan
- 112 Homer L. Dodge Department of Physics and Astronomy, University of Oklahoma, Norman OK, United States of America
- 113 Department of Physics, Oklahoma State University, Stillwater OK, United States of America
- 114 Palacký University, RCPTM, Olomouc, Czech Republic
- 115 Center for High Energy Physics, University of Oregon, Eugene OR, United States of America
- 116 LAL, Université Paris-Sud and CNRS/IN2P3, Orsay, France
- 117 Graduate School of Science, Osaka University, Osaka, Japan
- 118 Department of Physics, University of Oslo, Oslo, Norway
- 119 Department of Physics, Oxford University, Oxford, United Kingdom
- 120 ^(a) INFN Sezione di Pavia; ^(b) Dipartimento di Fisica, Università di Pavia, Pavia, Italy
- 121 Department of Physics, University of Pennsylvania, Philadelphia PA, United States of America
- 122 Petersburg Nuclear Physics Institute, Gatchina, Russia
- 123 ^(a) INFN Sezione di Pisa; ^(b) Dipartimento di Fisica E. Fermi, Università di Pisa, Pisa, Italy
- 124 Department of Physics and Astronomy, University of Pittsburgh, Pittsburgh PA, United States of America
- 125 ^(a) Laboratório de Instrumentação e Física Experimental de Partículas - LIP, Lisboa, Portugal; ^(b) Departamento de Física Teórica y del Cosmos and CAFPE, Universidad de Granada, Granada, Spain
- 126 Institute of Physics, Academy of Sciences of the Czech Republic, Praha, Czech Republic
- 127 Czech Technical University in Prague, Praha, Czech Republic
- 128 Faculty of Mathematics and Physics, Charles University in Prague, Praha, Czech Republic
- 129 State Research Center Institute for High Energy Physics, Protvino, Russia
- 130 Particle Physics Department, Rutherford Appleton Laboratory, Didcot, United Kingdom
- 131 Physics Department, University of Regina, Regina SK, Canada
- 132 Ritsumeikan University, Kusatsu, Shiga, Japan
- 133 ^(a) INFN Sezione di Roma I; ^(b) Dipartimento di Fisica, Università La Sapienza, Roma, Italy
- 134 ^(a) INFN Sezione di Roma Tor Vergata; ^(b) Dipartimento di Fisica, Università di Roma Tor Vergata, Roma, Italy
- 135 ^(a) INFN Sezione di Roma Tre; ^(b) Dipartimento di Matematica e Fisica, Università Roma Tre, Roma, Italy
- 136 ^(a) Faculté des Sciences Ain Chock, Réseau Universitaire de Physique des Hautes Energies - Université Hassan II, Casablanca; ^(b) Centre National de l'Energie des Sciences Techniques Nucleaires, Rabat; ^(c) Faculté des Sciences Semlalia, Université Cadi Ayyad,

LPHEA-Marrakech; ^(d) Faculté des Sciences, Université Mohamed Premier and LPTPM, Oujda; ^(e) Faculté des sciences, Université Mohammed V-Agdal, Rabat, Morocco

¹³⁷ DSM/IRFU (Institut de Recherches sur les Lois Fondamentales de l'Univers), CEA Saclay (Commissariat à l'Energie Atomique et aux Energies Alternatives), Gif-sur-Yvette, France

¹³⁸ Santa Cruz Institute for Particle Physics, University of California Santa Cruz, Santa Cruz CA, United States of America

¹³⁹ Department of Physics, University of Washington, Seattle WA, United States of America

¹⁴⁰ Department of Physics and Astronomy, University of Sheffield, Sheffield, United Kingdom

¹⁴¹ Department of Physics, Shinshu University, Nagano, Japan

¹⁴² Fachbereich Physik, Universität Siegen, Siegen, Germany

¹⁴³ Department of Physics, Simon Fraser University, Burnaby BC, Canada

¹⁴⁴ SLAC National Accelerator Laboratory, Stanford CA, United States of America

¹⁴⁵ ^(a) Faculty of Mathematics, Physics & Informatics, Comenius University, Bratislava; ^(b) Department of Subnuclear Physics, Institute of Experimental Physics of the Slovak Academy of Sciences, Kosice, Slovak Republic

¹⁴⁶ ^(a) Department of Physics, University of Cape Town, Cape Town; ^(b) Department of Physics, University of Johannesburg, Johannesburg; ^(c) School of Physics, University of the Witwatersrand, Johannesburg, South Africa

¹⁴⁷ ^(a) Department of Physics, Stockholm University; ^(b) The Oskar Klein Centre, Stockholm, Sweden

¹⁴⁸ Physics Department, Royal Institute of Technology, Stockholm, Sweden

¹⁴⁹ Departments of Physics & Astronomy and Chemistry, Stony Brook University, Stony Brook NY, United States of America

¹⁵⁰ Department of Physics and Astronomy, University of Sussex, Brighton, United Kingdom

¹⁵¹ School of Physics, University of Sydney, Sydney, Australia

¹⁵² Institute of Physics, Academia Sinica, Taipei, Taiwan

¹⁵³ Department of Physics, Technion: Israel Institute of Technology, Haifa, Israel

¹⁵⁴ Raymond and Beverly Sackler School of Physics and Astronomy, Tel Aviv University, Tel Aviv, Israel

¹⁵⁵ Department of Physics, Aristotle University of Thessaloniki, Thessaloniki, Greece

¹⁵⁶ International Center for Elementary Particle Physics and Department of Physics, The University of Tokyo, Tokyo, Japan

¹⁵⁷ Graduate School of Science and Technology, Tokyo Metropolitan University, Tokyo, Japan

¹⁵⁸ Department of Physics, Tokyo Institute of Technology, Tokyo, Japan

¹⁵⁹ Department of Physics, University of Toronto, Toronto ON, Canada

¹⁶⁰ ^(a) TRIUMF, Vancouver BC; ^(b) Department of Physics and Astronomy, York University, Toronto ON, Canada

¹⁶¹ Faculty of Pure and Applied Sciences, University of Tsukuba, Tsukuba, Japan

- ¹⁶² Department of Physics and Astronomy, Tufts University, Medford MA, United States of America
- ¹⁶³ Centro de Investigaciones, Universidad Antonio Narino, Bogota, Colombia
- ¹⁶⁴ Department of Physics and Astronomy, University of California Irvine, Irvine CA, United States of America
- ¹⁶⁵ ^(a) INFN Gruppo Collegato di Udine; ^(b) ICTP, Trieste; ^(c) Dipartimento di Chimica, Fisica e Ambiente, Università di Udine, Udine, Italy
- ¹⁶⁶ Department of Physics, University of Illinois, Urbana IL, United States of America
- ¹⁶⁷ Department of Physics and Astronomy, University of Uppsala, Uppsala, Sweden
- ¹⁶⁸ Instituto de Física Corpuscular (IFIC) and Departamento de Física Atómica, Molecular y Nuclear and Departamento de Ingeniería Electrónica and Instituto de Microelectrónica de Barcelona (IMB-CNM), University of Valencia and CSIC, Valencia, Spain
- ¹⁶⁹ Department of Physics, University of British Columbia, Vancouver BC, Canada
- ¹⁷⁰ Department of Physics and Astronomy, University of Victoria, Victoria BC, Canada
- ¹⁷¹ Department of Physics, University of Warwick, Coventry, United Kingdom
- ¹⁷² Waseda University, Tokyo, Japan
- ¹⁷³ Department of Particle Physics, The Weizmann Institute of Science, Rehovot, Israel
- ¹⁷⁴ Department of Physics, University of Wisconsin, Madison WI, United States of America
- ¹⁷⁵ Fakultät für Physik und Astronomie, Julius-Maximilians-Universität, Würzburg, Germany
- ¹⁷⁶ Fachbereich C Physik, Bergische Universität Wuppertal, Wuppertal, Germany
- ¹⁷⁷ Department of Physics, Yale University, New Haven CT, United States of America
- ¹⁷⁸ Yerevan Physics Institute, Yerevan, Armenia
- ¹⁷⁹ Centre de Calcul de l'Institut National de Physique Nucléaire et de Physique des Particules (IN2P3), Villeurbanne, France
- ^a Also at Department of Physics, King's College London, London, United Kingdom
- ^b Also at Laboratório de Instrumentação e Física Experimental de Partículas - LIP, Lisboa, Portugal
- ^c Also at Institute of Physics, Azerbaijan Academy of Sciences, Baku, Azerbaijan
- ^d Also at Faculdade de Ciências and CFNUL, Universidade de Lisboa, Lisboa, Portugal
- ^e Also at Particle Physics Department, Rutherford Appleton Laboratory, Didcot, United Kingdom
- ^f Also at TRIUMF, Vancouver BC, Canada
- ^g Also at Department of Physics, California State University, Fresno CA, United States of America
- ^h Also at Novosibirsk State University, Novosibirsk, Russia
- ⁱ Also at Department of Physics, University of Coimbra, Coimbra, Portugal
- ^j Also at Università di Napoli Parthenope, Napoli, Italy
- ^k Also at Institute of Particle Physics (IPP), Canada
- ^l Also at Department of Physics, Middle East Technical University, Ankara, Turkey
- ^m Also at Louisiana Tech University, Ruston LA, United States of America

- ⁿ Also at Dep Fisica and CEFITEC of Faculdade de Ciencias e Tecnologia, Universidade Nova de Lisboa, Caparica, Portugal
- ^o Also at CPPM, Aix-Marseille Université and CNRS/IN2P3, Marseille, France
- ^p Also at Department of Physics and Astronomy, Michigan State University, East Lansing MI, United States of America
- ^q Also at Department of Financial and Management Engineering, University of the Aegean, Chios, Greece
- ^r Also at Institutio Catalana de Recerca i Estudis Avancats, ICREA, Barcelona, Spain
- ^s Also at Department of Physics, University of Cape Town, Cape Town, South Africa
- ^t Also at CERN, Geneva, Switzerland
- ^u Also at O Chadai Academic Production, Ochanomizu University, Tokyo, Japan
- ^v Also at Manhattan College, New York NY, United States of America
- ^w Also at Institute of Physics, Academia Sinica, Taipei, Taiwan
- ^x Also at School of Physics and Engineering, Sun Yat-sen University, Guanzhou, China
- ^y Also at Academia Sinica Grid Computing, Institute of Physics, Academia Sinica, Taipei, Taiwan
- ^z Also at Laboratoire de Physique Nucléaire et de Hautes Energies, UPMC and Université Paris-Diderot and CNRS/IN2P3, Paris, France
- ^{aa} Also at School of Physical Sciences, National Institute of Science Education and Research, Bhubaneswar, India
- ^{ab} Also at Dipartimento di Fisica, Università La Sapienza, Roma, Italy
- ^{ac} Also at DSM/IRFU (Institut de Recherches sur les Lois Fondamentales de l'Univers), CEA Saclay (Commissariat à l'Energie Atomique et aux Energies Alternatives), Gif-sur-Yvette, France
- ^{ad} Also at Moscow Institute of Physics and Technology State University, Dolgoprudny, Russia
- ^{ae} Also at Section de Physique, Université de Genève, Geneva, Switzerland
- ^{af} Also at Departamento de Fisica, Universidade de Minho, Braga, Portugal
- ^{ag} Also at Department of Physics, The University of Texas at Austin, Austin TX, United States of America
- ^{ah} Also at Institute for Particle and Nuclear Physics, Wigner Research Centre for Physics, Budapest, Hungary
- ^{ai} Also at DESY, Hamburg and Zeuthen, Germany
- ^{aj} Also at International School for Advanced Studies (SISSA), Trieste, Italy
- ^{ak} Also at Department of Physics and Astronomy, University of South Carolina, Columbia SC, United States of America
- ^{al} Also at Faculty of Physics, M.V.Lomonosov Moscow State University, Moscow, Russia
- ^{am} Also at Nevis Laboratory, Columbia University, Irvington NY, United States of America
- ^{an} Also at Physics Department, Brookhaven National Laboratory, Upton NY, United States of America
- ^{ao} Also at Moscow Engineering and Physics Institute (MEPhI), Moscow, Russia
- ^{ap} Also at Department of Physics, Oxford University, Oxford, United Kingdom

^{aq} Also at Institut für Experimentalphysik, Universität Hamburg, Hamburg, Germany

^{ar} Also at Department of Physics, The University of Michigan, Ann Arbor MI, United States of America

^{as} Also at Discipline of Physics, University of KwaZulu-Natal, Durban, South Africa

* Deceased